The Astrophysical Journal, 877:93 (42pp), 2019 June 1 https://doi.org/10.3847/1538-4357/ab1a40
© 2019. The American Astronomical Society.
OPEN ACCESS

Droplets. I. Pressure-dominated Coherent Structures in L1688 and B18

Hope How-Huan Chen[1], Jaime E. Pineda[2], Alyssa A. Goodman[3], Andreas Burkert[4], Stella S. R. Offner[1], Rachel K. Friesen[5], Philip C. Myers[3], Felipe Alves[2], Héctor G. Arce[6], Paola Caselli[2], Ana Chacón-Tanarro[2], Michael Chun-Yuan Chen[7], James Di Francesco[7,8], Adam Ginsburg[9], Jared Keown[7], Helen Kirk[7,8], Peter G. Martin[10], Christopher Matzner[11], Anna Punanova[12], Elena Redaelli[2], Erik Rosolowsky[13], Samantha Scibelli[14], Youngmin Seo[15], Yancy Shirley[14], and Ayushi Singh[11]
(The GAS Collaboration)
[1] Department of Astronomy, The University of Texas, Austin, TX 78712, USA; hopechen@utexas.edu
[2] Max-Planck-Institut für extraterrestrische Physik, Giesenbachstrasse 1, D-85748 Garching, Germany
[3] Harvard-Smithsonian Center for Astrophysics, 60 Garden St., Cambridge, MA 02138, USA
[4] University Observatory Munich (USM), Scheinerstrasse 1, D-81679 Munich, Germany
[5] National Radio Astronomy Observatory, 520 Edgemont Rd., Charlottesville, VA 22903, USA
[6] Department of Astronomy, Yale University, P.O. Box 208101, New Haven, CT 06520-8101, USA
[7] Department of Physics and Astronomy, University of Victoria, 3800 Finnerty Rd., Victoria, BC V8P 5C2, Canada
[8] Herzberg Astronomy and Astrophysics, National Research Council of Canada, 5071 West Saanich Rd., Victoria, BC V9E 2E7, Canada
[9] National Radio Astronomy Observatory, Socorro, NM 87801, USA
[10] Canadian Institute for Theoretical Astrophysics, University of Toronto, 60 St. George St., Toronto, ON M5S 3H8, Canada
[11] Department of Astronomy & Astrophysics, University of Toronto, 50 St. George St., Toronto, ON M5S 3H4, Canada
[12] Ural Federal University, 620002, 19 Mira St., Yekaterinburg, Russia
[13] Department of Physics, 4-181 CCIS, University of Alberta, Edmonton, AB T6G 2E1, Canada
[14] Steward Observatory, 933 North Cherry Ave., Tucson, AZ 85721, USA
[15] Jet Propulsion Laboratory, NASA, 4800 Oak Grove Dr., Pasadena, CA 91109, USA
Received 2018 September 25; revised 2019 April 11; accepted 2019 April 11; published 2019 May 29

Abstract

We present the observation and analysis of newly discovered coherent structures in the L1688 region of Ophiuchus and the B18 region of Taurus. Using data from the Green Bank Ammonia Survey, we identify regions of high density and near-constant, almost-thermal velocity dispersion. We reveal 18 coherent structures are revealed, 12 in L1688 and 6 in B18, each of which shows a sharp "transition to coherence" in velocity dispersion around its periphery. The identification of these structures provides a chance to statistically study the coherent structures in molecular clouds. The identified coherent structures have a typical radius of 0.04 pc and a typical mass of 0.4 $M_{\odot}$, generally smaller than previously known coherent cores identified by Goodman et al., Caselli et al., and Pineda et al. We call these structures "droplets." We find that, unlike previously known coherent cores, these structures are not virially bound by self-gravity and are instead predominantly confined by ambient pressure. The droplets have density profiles shallower than a critical Bonnor–Ebert sphere, and they have a velocity ($V_{\rm LSR}$) distribution consistent with the dense gas motions traced by NH_3 emission. These results point to a potential formation mechanism through pressure compression and turbulent processes in the dense gas. We present a comparison with a magnetohydrodynamic simulation of a star-forming region, and we speculate on the relationship of droplets with larger, gravitationally bound coherent cores, as well as on the role that droplets and other coherent structures play in the star formation process.

Key words: ISM: clouds – ISM: individual objects (L1688, B18) – ISM: kinematics and dynamics – magnetohydrodynamics (MHD) – radio lines: ISM – stars: formation

Supporting material: animation

1. Introduction

In the early 1980s, NH_3 was identified as an excellent tracer of the cold, dense gas associated with highly extinguished compact regions. These regions were named "dense cores" by Myers et al. (1983). Their properties were studied and documented in a series of papers throughout the 1980s and 1990s, the titles of which began with "Dense Cores in Dark Clouds" (Benson & Myers 1983; Myers 1983; Myers et al. 1983; Myers & Benson 1983; Fuller & Myers 1992; Goodman et al. 1993; Benson et al. 1998; Caselli et al. 2002). Since the start of that series, astronomers have used the "dense core" paradigm as a way to think about the small (0.1 pc, with the smallest being ~0.03 pc) (Myers & Benson 1983; Jijina et al. 1999), prolate but roundish (aspect ratio near 2) (Myers et al. 1991), quiescent (velocity dispersion nearly thermal) (Fuller & Myers 1992), blobs of gas that can form stars like the Sun. Whether these cores also exist in clusters where more massive stars form (Evans 1999; Garay & Lizano 1999; Tan et al. 2006; Li et al. 2015), how long-lived and/or transient these cores might be (Bertoldi & McKee 1992; Ballesteros-Paredes et al. 1999; Elmegreen 2000; Enoch et al. 2008), and how they relate to the ubiquitous filamentary structure inside star-forming regions (McKee & Ostriker 2007; Hacar et al. 2013; André et al. 2014; Padoan et al. 2014; Tafalla & Hacar 2015) are still open questions. Nonetheless, a gravitationally collapsing "dense core" remains the central theme in discussions of star-forming material.

Original content from this work may be used under the terms of the Creative Commons Attribution 3.0 licence. Any further distribution of this work must maintain attribution to the author(s) and the title of the work, journal citation and DOI.

Barranco & Goodman (1998) made observations of NH_3 hyperfine line emission of four "dense cores" and found that the line widths in the interior of a dense core are roughly constant at a value slightly higher than a purely thermal line width, and that the line widths start to increase near the edge of the dense core. Using observations of OH and $C^{18}O$ line emission, Goodman et al. (1998) proposed a characteristic radius where the scaling law between the line width and the size changes, marking the "transition to coherence." Goodman et al. (1998) found that the characteristic radius is ∼0.1 pc and that the line width is virtually constant within ∼0.1 pc from the center of a dense core. This gave birth to the idea of the existence of "coherent cores" at the densest part of previously identified "dense cores." The coherence is defined by a transition from supersonic to subsonic turbulent velocity dispersion that is found to accompany a sharp change in the scaling law between the velocity dispersion and the size scale. Goodman et al. (1998) hypothesized that the coherent core provides the needed "calmness," or low-turbulence, environment for further star formation dominated by gravitational collapse.

Using Green Bank Telescope (GBT) observations of NH_3 hyperfine line emission, Pineda et al. (2010) made the first direct observation of a coherent core, resolving the transition to coherence across the boundary from a "Larson's Law"-like (turbulent) regime to a coherent (thermal) one. The observed coherent core sits in the B5 region in Perseus and has an elongated shape with a characteristic radius of ∼0.2 pc. The interior line widths are almost constant and subsonic, but are not purely thermal. Later VLA observations of the interior of B5 by Pineda et al. (2011) show that there are finer structures inside the coherent core, and Pineda et al. (2015) found that these substructures are forming stars in a freefall time of ∼40,000 yr. The gravitationally collapsing substructures inside the coherent core are consistent with the picture of star formation within the "calmness" of a coherent core.

The coherent core in B5 has remained the only known example where the transition to coherence is spatially resolved with a single tracer. In search of other coherent structures in nearby molecular clouds, we follow the same procedure adopted by Pineda et al. (2010) and identify a total of 18 coherent structures, 12 in the L1688 region in Ophiuchus and 6 in the B18 region in Perseus, using data from the Green Bank Ammonia Survey (GAS) (Friesen et al. 2017). Although many of these structures may be associated with previously known cores or density features, this is the first time "transitions to coherence" have been captured using a single tracer. The 18 coherent structures identified within a total projected area on the plane of the sky of $\sim 0.6\,\mathrm{pc}^2$ suggest the ubiquity of coherent structures in nearby molecular clouds. This catalog allows statistical analyses of coherent structures for the first time.

In the analyses presented in this paper, we find that these newly identified coherent structures have small sizes, ∼0.04 pc, and masses, $\sim 0.4\,M_\odot$.[16] Unlike previously known coherent cores, the coherent structures identified in this paper are mostly gravitationally unbound; instead, they are predominantly bound by pressure provided by the ambient gas motions, despite the subsonic velocity dispersions found in these structures.[17] We term this newly discovered population of gravitationally unbound and pressure confined coherent structures "droplets," and examine their relation to the known gravitationally bound and likely star-forming coherent cores and other dense cores.

In this paper, we present a full description of the physical properties of the droplets and discuss their potential formation mechanism. In Section 2, we describe the data used in this paper, including data from the GAS DR1 (Section 2.1; Friesen et al. 2017), maps of column density and dust temperature based on spectral energy distribution (SED) fitting of observations made by the Herschel Gould Belt Survey (HGBS) (Section 2.2; André et al. 2010), and the catalogs of previously known NH_3 cores (Section 2.3; Goodman et al. 1993; Pineda et al. 2010). In Section 3, we present our analysis of the droplets, including their identification (Section 3.1), basic properties (Section 3.2), and a virial analysis including an ambient gas pressure term (Section 3.3). In the discussion, we further examine the nature of their pressure confinement in Section 4.1, by comparing the radial density and pressure profiles to the Bonnor–Ebert model (Section 4.1.1) and the logotropic spheres (Section 4.1.2). We examine the relation between the droplets and the host molecular cloud by looking into the velocity distributions (Section 4.1.3). We then demonstrate that formation of droplets is possible in a magnetohydrodynamics (MHD) simulation, and speculate on the formation mechanism of the droplets in Section 4.2. We discuss their relation to coherent cores and their evolution in Section 4.3. Finally, in Section 5, we summarize this work and outline future projects that might shed more light on how droplets form, their relationship with structures at different size scales, and the role they might play in star formation.

2. Data

2.1. Green Bank Ammonia Survey (GAS)

The GAS (Friesen et al. 2017) is a Large Program at the GBT to map most Gould Belt star-forming regions with $A_V \geqslant 7$ mag visible from the northern hemisphere in emission from NH_3 and other key molecules.[18] The data used in this work are from the first data release (DR1) of GAS that includes four nearby star-forming regions: L1688 in Ophiuchus, B18 in Taurus, NGC 1333 in Perseus, and Orion A.

To achieve better physical resolution, only the two closest regions in the GAS DR1 are used in our present study. L1688 in Ophiuchus sits at a distance of 137.3 ± 6 pc (Ortiz-León et al. 2017), and B18 in Taurus sits at a distance of 126.6 ± 1.7 pc (notice this is updated from the distance adopted by Friesen et al. (2017), which was taken from Schlafly et al. (2014) and Galli et al. (2018)). At these distances, the GBT full width at half maximum (FWHM) beam size of 32″ at 23 GHz corresponds to ∼4350 au (0.02 pc). The GBT beam size at 23 GHz also matches well with the *Herschel* SPIRE 500 μm FWHM beam size of 36″ (see Section 2.2 and discussions in Friesen et al. (2017)). The GBT observations have a spectral resolution of 5.7 kHz, or $\sim 0.07\,\mathrm{km\,s^{-1}}$ at 23 GHz.

[16] Like many of the dense cores observed by Myers (1983), a coherent region has a thermally dominated velocity dispersion. The identification of these coherent structures is "new" in the sense that "transitions to coherence" are captured in a single tracer for the first time for many of these structures and that the identified coherent structures form a previously omitted population of gravitationally unbound and pressure-confined coherent structures, as shown in the analyses below. We acknowledge that many of the coherent structures examined in this paper might be associated with previously known cores or density features. See Appendix C for discussion.

[17] In this paper, the adjectives "supersonic," "transonic," and "subsonic" indicate levels of turbulence. A supersonic/transonic/subsonic velocity dispersion has a turbulent (nonthermal) component larger than/comparable to/smaller than the sonic velocity. See Equation (1) below for a definition of the thermal and nonthermal components of velocity dispersion.

[18] The data from the first data release are public and can be found at https://dataverse.harvard.edu/dataverse/GAS_Project.

2.1.1. Fitting the NH_3 Line Profile

In the GAS DR1, a (single) Gaussian line shape is assumed in fitting spectra of NH_3 (1, 1) and (2, 2) hyperfine line emission (see Section 3.1 in Friesen et al. 2017). The fitting is carried out using the "cold-ammonia" model and a forward-modeling approach in the `PySpecKit` package (Ginsburg & Mirocha 2011), which was developed in Friesen et al. (2017) and built upon the results from Rosolowsky et al. (2008a) and Friesen et al. (2009) in the theoretical framework laid out by Mangum & Shirley (2015). No fitting of multiple velocity components or non-Gaussian profiles was attempted in GAS DR1, but the single-component fitting produced good-quality results in $\gtrsim$95% of detections in all regions included in the GAS DR1. From the fit, we obtain the velocity centroid of emission along each line of sight (Gaussian mean of the best fit) and the velocity dispersion (Gaussian σ), where we have sufficient signal-to-noise in NH_3 (1, 1) emission. For lines of sight where we detect both NH_3 (1, 1) and (2, 2), the model described in Friesen et al. (2017) provides estimates of parameters including the kinetic temperature and the NH_3 column density. Figures 1–4 show the parameters derived from the fitting of the NH_3 hyperfine line profiles.

2.2. Herschel *Column Density Maps*

The *Herschel* column density maps are derived from archival *Herschel* PACS 160 and SPIRE 250/350/500 μm observations of dust emission, observed as part of the Herschel Gould Belt Survey (HGBS) (André et al. 2010). We establish the zero point of emission at each wavelength, using *Planck* observations of the same regions (Planck Collaboration et al. 2014). The emission maps are then convolved to match the SPIRE 500 μm beam FWHM of 36″ and passed to a least-squares fitting routine, where we assume that the emission at these wavelengths follow a modified blackbody emission function, $I_\nu = (1 - \exp^{-\tau_\nu})B_\nu(T)$, where $B_\nu(T)$ is the blackbody radiation and τ is the frequency-dependent opacity. The opacity can be written as a function of the mass column density, $\tau_\nu = \kappa_\nu \Sigma$, where κ_ν is the opacity coefficient. At these wavelengths, κ_ν can be described by a power-law function of frequency, $\kappa_\nu = \kappa_{\nu_0}\left(\frac{\nu}{\nu_0}\right)^\beta$, where β is the emissivity index and κ_{ν_0} is the opacity coefficient at frequency ν_0. Here, we adopt κ_{ν_0} of 0.1 cm^2 g^{-1} at $\nu_0 = 1000$ GHz (Hildebrand 1983) and a fixed β of 1.62 (Planck Collaboration et al. 2014). The resulting I_ν is a function of the temperature and the dust column density, the latter of which can be further converted to the total number column density by assuming a dust-to-gas ratio (100, for the maps we derive) and defining a mean molecular weight[19] (2.8 u; μ_{H_2} in Kauffmann et al. (2008)). The resulting column density map has an angular resolution of 36″ (the SPIRE 500 μm beam FWHM), which matches well with the GBT beam FWHM at 23 GHz (32″). In the following analyses, we do not apply convolution to further match the resolutions of the *Herschel* and GBT observations before regridding the maps onto the same projection and gridding (Nyquist-sampled). Resulting maps column density and dust temperature are shown in Figures 5 and 6 for L1688 in Ophiuchus and B18 in Taurus, respectively.

2.3. Source Catalogs

To understand *droplets* in context, we need compilations of the physical properties of previously identified dense cores. Goodman et al. (1993) (see Section 2.3.1) present a summary of cores from the observational surveys described in Benson & Myers (1989) and Ladd et al. (1994). The cores in Goodman et al. (1993) have low, nearly thermal velocity dispersions, and some of them are known to be "coherent" based on an apparent abrupt spatial transition from supersonic (in OH and $C^{18}O$) to subsonic (in NH_3) velocity dispersion (Goodman et al. 1998; Caselli et al. 2002). We also include the coherent core in the B5 region in Perseus, as observed in NH_3 (Pineda et al. 2010), the only coherent structure known before this work where the spatial change in line width is captured in a single tracer.

2.3.1. Dense Cores Measured in NH_3

Goodman et al. (1993) presented a survey of 43 sources with observations of NH_3 line emission (see Tables 1 and 2 in Goodman et al. (1993); see also the SIMBAD object list[20]), based on observations made by Benson & Myers (1989) and Ladd et al. (1994). The observations were carried out at the 37 m telescope of the Haystack Observatory and the 43 m telescope of the National Radio Astronomy Observatory (NRAO), resulting in a spatial resolution coarser than the modern GBT observations by a factor of ~2.5. The velocity resolution of observations done by Benson & Myers (1989) and Ladd et al. (1994) ranges from 0.07 to 0.20 km s^{-1}. For comparison with the kinematic properties of the droplets measured using the GAS observations of NH_3 emission (Friesen et al. 2017), we adopt values that were also measured using observations of NH_3 hyperfine line emission, presented by Goodman et al. (1993). We correct the physical properties summarized in Goodman et al. (1993) with the modern measurement of the distance to each region. The updated distances are summarized in Appendix A.

The updated distances affect the physical properties listed in Table 1 in Goodman et al. (1998). The size scales with the distance, D, by a linear relation, $R \propto D$. Because the mass was calculated from the number density derived from NH_3 hyperfine line fitting, it scales with the volume of the structure—and thus $M \propto D^3$. The updated distances also affect the velocity gradient and related quantities listed in Tables 1 and 2 in Goodman et al. (1998), which we do not use for the analyses presented in this work.

Apart from the updated distances, we combine the measurements of the kinetic temperature and the NH_3 line width, originally presented by Benson & Myers (1989) and Ladd et al. (1994), to derive the thermal and the nonthermal components of the velocity dispersion. See Equation (1) below for the definitions of the velocity dispersion components.

Among the 43 sources examined by Goodman et al. (1993), eight sources were later confirmed by Goodman et al. (1998) and/or Caselli et al. (2002) to be "coherent cores," using a combination of gas tracers of various critical densities (OH, $C^{18}O$, NH_3, and

[19] In this paper, we use the mean molecular weight per H_2 molecule (2.8 u; μ_{H_2} in Kauffmann et al. (2008)) in the calculation of the mass and other density-related quantities, and we use the mean molecular weight per free particle (2.37 u; μ_p in Kauffmann et al. (2008)) in the calculation of the velocity dispersion and pressure. Both numbers are derived assuming a hydrogen mass ratio of $M_H/M_{total} \approx 0.71$, a helium mass ratio of $M_{He}/M_{total} \approx 0.27$, and a metal mass ratio of $M_Z/M_{total} \approx 0.02$ (Cox & Pilachowski 2000). See Appendix A.1 in Kauffmann et al. (2008).

[20] http://simbad.harvard.edu/simbad/sim-ref?querymethod=bib&simbo=on&submit=submit+bibcode&bibcode=1993ApJ...406..528G

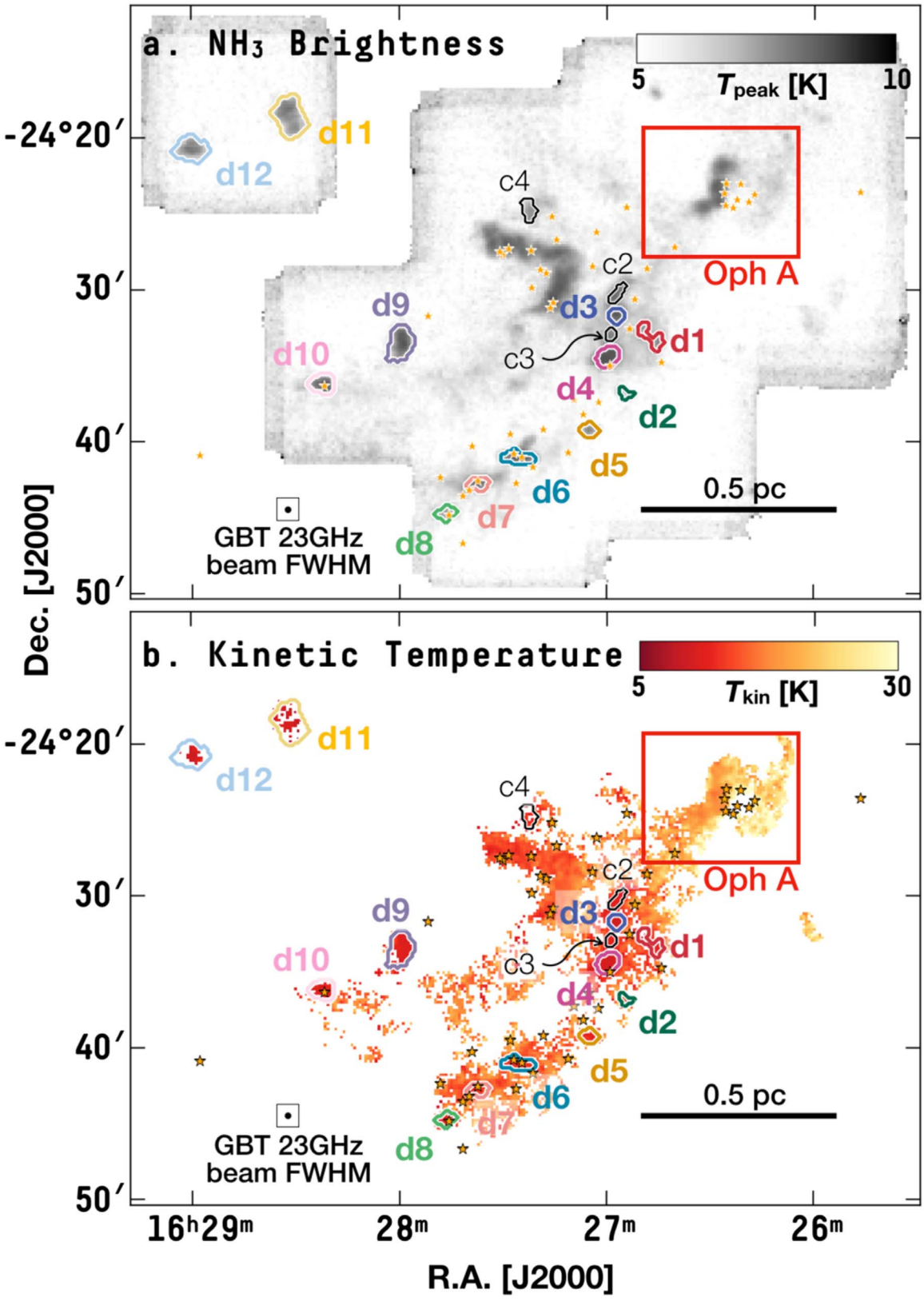

Figure 1. L1688 in Ophiuchus. Shown here are maps of (a) peak NH_3 (1, 1) brightness in the unit of main-beam temperature, T_{peak}, and (b) kinetic temperature, T_{kin}. The colored contours mark the boundaries of droplets, and the black contours mark the boundaries of droplet candidates. Because L1688-c1E and L1688-c1W overlap with L1688-d1, they are not shown in this figure or Figure 2 (see Section 3.1). The stars mark the positions of Class 0/I and flat-spectrum protostars from Dunham et al. (2015). The scale bar at the bottom right corner corresponds to 0.5 pc at the distance of Ophiuchus. The black circle at the bottom-left corner of each panel shows the beam FWHM of the GBT observations at 23 GHz. See Appendix B for a gallery of the close-up views of the droplets.

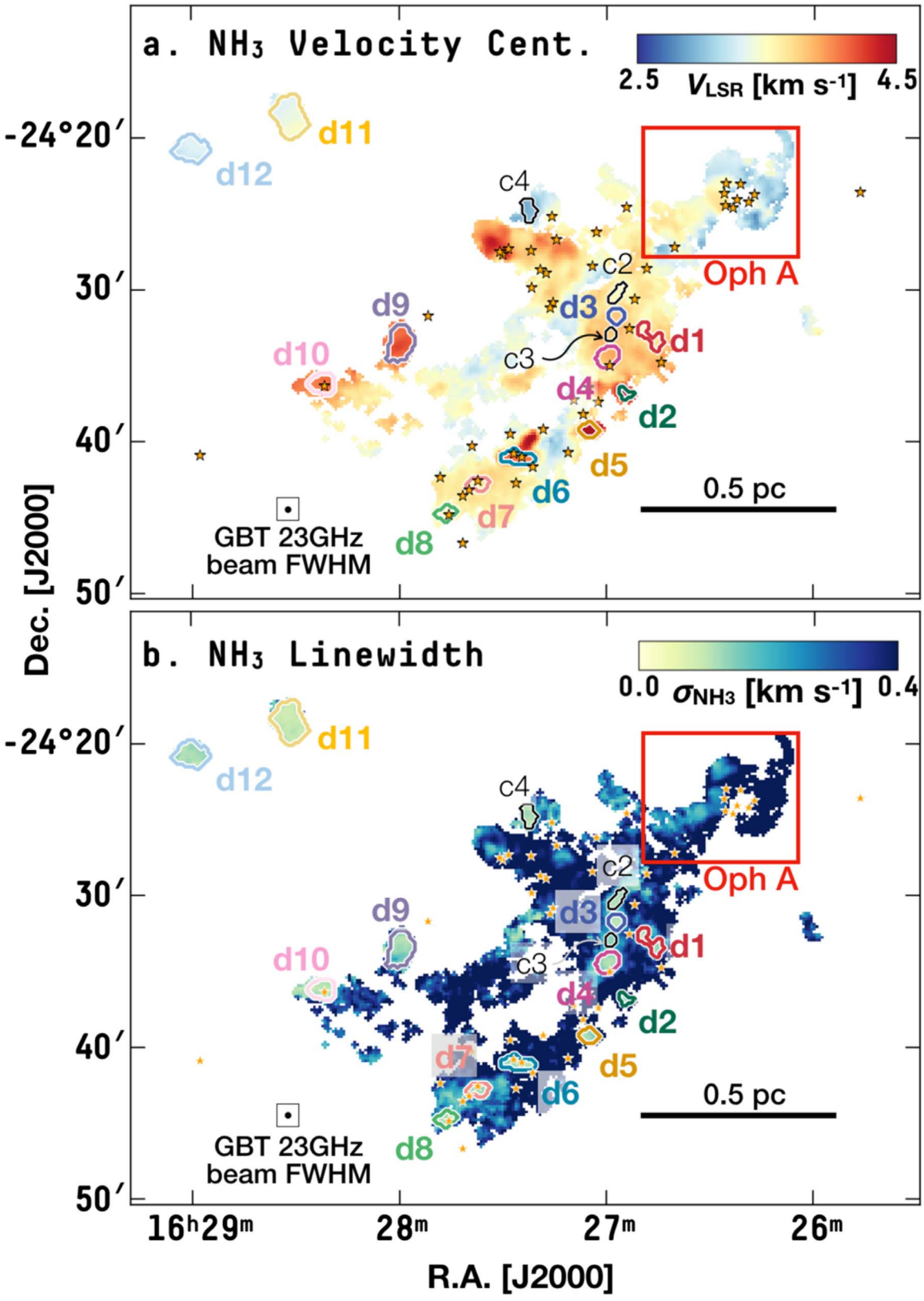

Figure 2. Like Figure 1, but for maps of (a) velocity centroid, V_{LSR}, and (b) velocity dispersion, σ_{NH_3}.

N_2H^+). The interiors of these eight sources show signs of a uniform and nearly thermal distribution of velocity dispersion. However, unlike B5 and the newly identified coherent structures in this paper, the "transition to coherence" was not spatially resolved with a single tracer for these eight coherent cores. For the ease of discussion, we refer to the entire sample of 43 sources as the "dense cores," as they were originally referred to by Goodman et al. (1993). However, note that some of the 43 sources have

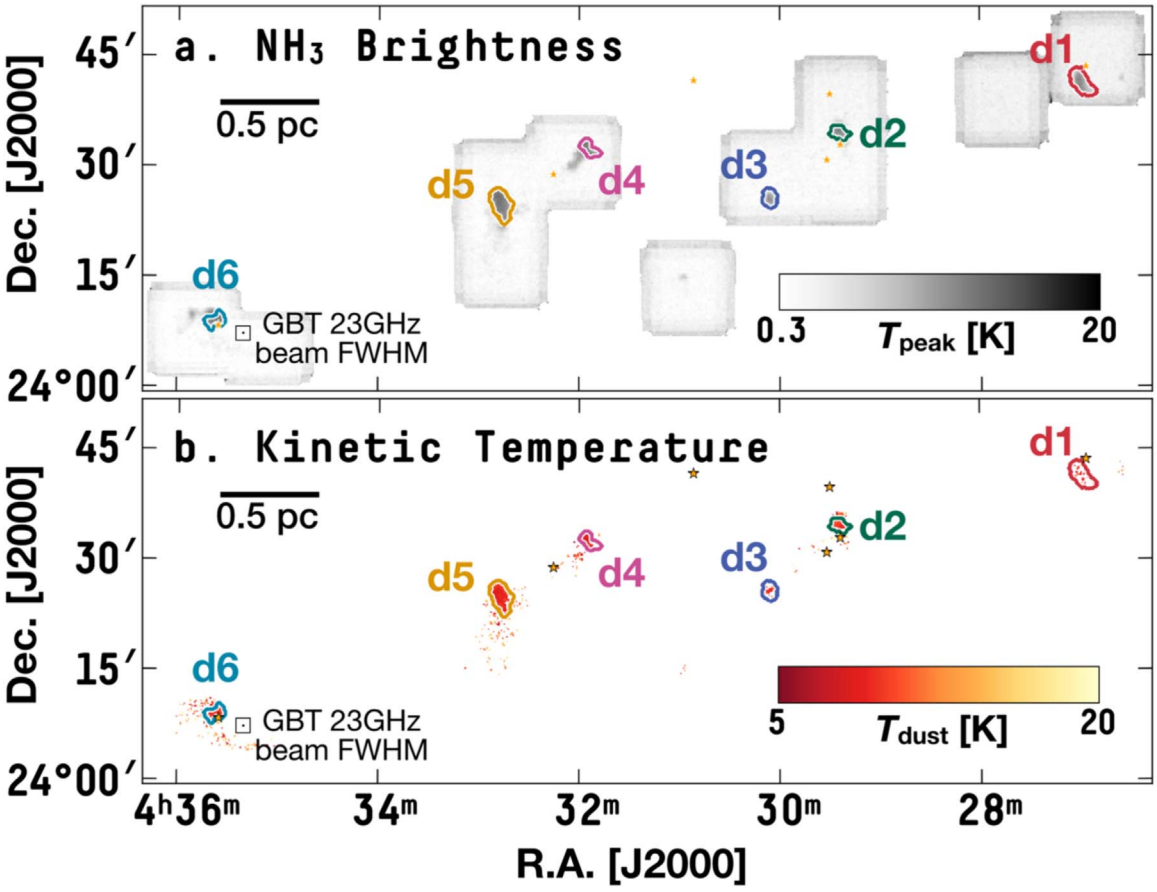

Figure 3. Like Figure 1, but for B18 in Taurus, showing maps of (a) peak NH_3 (1, 1) brightness in the unit of main-beam temperature, T_{peak}, and (b) kinetic temperature, T_{kin}. Here, the stars mark the positions of Class 0/I and flat-spectrum protostars with a reliability grade of A- or higher from Rebull et al. (2010). The scale bar at the bottom right corner corresponds to 0.5 pc at the distance of Taurus.

masses and sizes up to $\sim 100\,M_\odot$ and ~ 1 pc, respectively. These larger-scale structures do not strictly fit in the definition of a dense core (with a small size and a nearly thermal velocity dispersion; see Section 4.3 for further discussion) and might be better categorized as "dense clumps" (as in McKee & Ostriker (2007)).

2.3.2. Coherent Core in B5

Using GBT observations of NH_3 hyperfine line emission with a setup similar to GAS, Pineda et al. (2010) observed a coherent core in the B5 region in Perseus and spatially resolved the "transition to coherence"—NH_3 line widths changing from supersonic values outside the core to subsonic values inside—for the first time. The coherent core sits in the eastern part of the molecular cloud in Perseus, at a distance of 315 ± 32 pc (the quantities measured by Pineda et al. (2010) assuming a distance of 250 pc are updated according to the new distance measurement; see Schlafly et al. (2014)). At 315 pc, the GBT resolution at 23 GHz corresponds to a spatial resolution of ~ 0.05 pc. The coherent core has an elongated shape, with a size of ~ 0.2 pc.

Pineda et al. (2010) identified the coherent core in B5 as a peak in NH_3 brightness surrounded by an abrupt change in NH_3 velocity dispersion ($\sim 4\,\mathrm{km\,s^{-1}\,pc^{-1}}$). In the following analysis, we search the new GAS data for coherent structures reminiscent of the B5 core, looking for abrupt drops in NH_3 line width to nearly thermal values around local concentrations of dense gas traced by NH_3 (see Section 3.1 for details). Below, in the comparison between B5 and the newly identified coherent structures, we consistently follow the same methods adopted by Pineda et al. (2010) to derive the basic physical properties using GBT observations of NH_3 hyperfine line emission and *Herschel* column density maps derived from SED fitting (Section 2.2; see also Section 3.2 for details on the measurements of the physical properties).

3. Analysis

3.1. Identification of the Droplets

In this work, we look for coherent structures defined by abrupt drops in NH_3 line width and an interior with uniform, nearly thermal velocity dispersion,[21] reminiscent of previously known coherent cores examined by Goodman et al. (1998), Caselli et al. (2002), and Pineda et al. (2010). We identify the coherent structures using data from the GAS (see Section 2.1 Friesen et al. 2017) and the *Herschel* maps of column density and dust temperature derived in Section 2.2, in order to enable a statistical analysis of coherent structures in two of the closest molecular clouds, Ophiuchus and Taurus.

With only the naked eye, one can already recognize many small plateaus of subsonic velocity dispersion associated with NH_3-bright structures throughout L1688 and B18 in the maps

[21] The data and the codes used for the analyses presented in this work are made public on GitHub at the repository: hopehhchen/Droplets (https://github.com/hopehhchen/Droplets/tree/master/Droplets/).

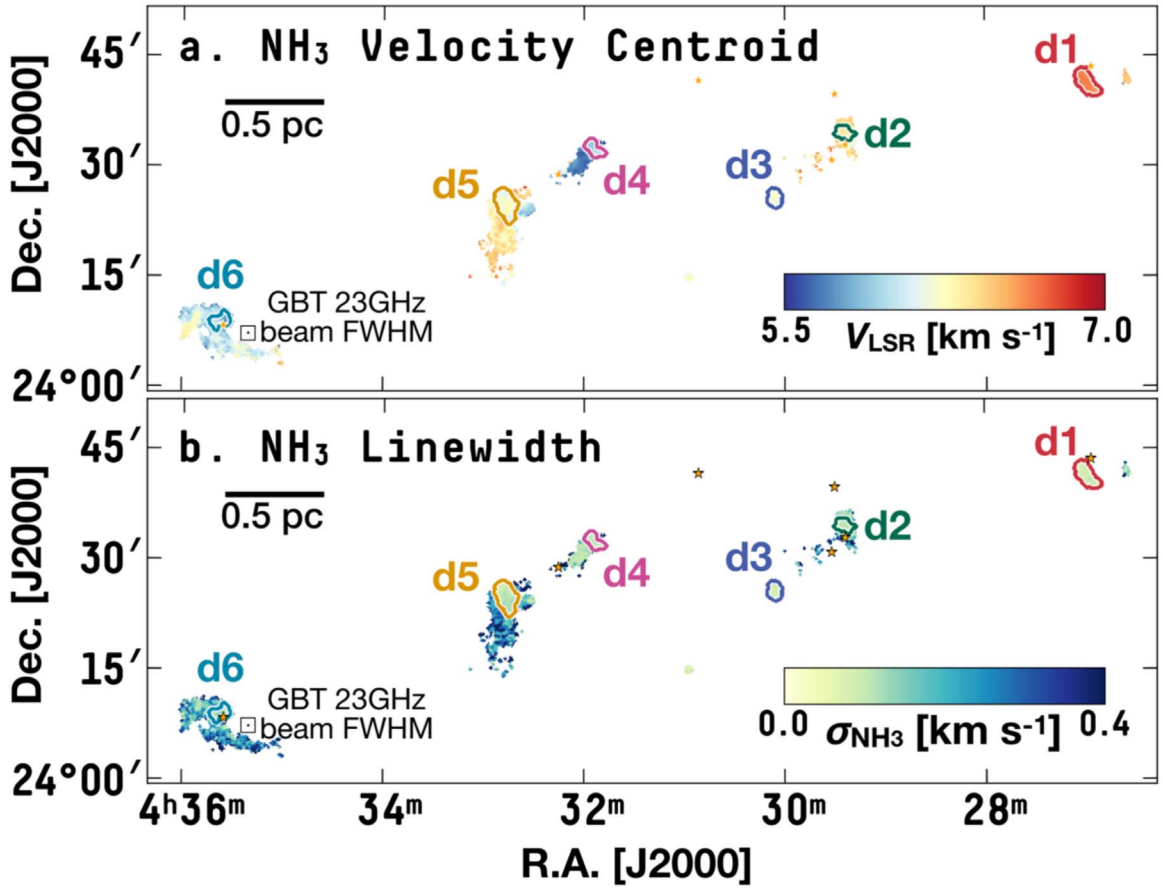

Figure 4. Like Figure 3 but for maps of (a) velocity centroid, $V_{\rm LSR}$, and (b) velocity dispersion, $\sigma_{\rm NH_3}$.

of observed velocity dispersion ($\sigma_{\rm NH_3}$) and NH_3 brightness (Figures 1–4). In order to quantitatively identify these coherent structures, we follow the procedure adopted by Pineda et al. (2010) to identify the coherent core region in B5. The set of criteria we use in this work to define the boundaries of coherent structures starts with the transition in velocity dispersion, $\sigma_{\rm NH_3}$, from a supersonic to a subsonic value, and continues with the spatial distribution of NH_3 brightness, $T_{\rm peak}$, and the velocity centroid, $V_{\rm LSR}$. A set of quantitative prescriptions for defining the boundary of a coherent structure is given below as a step-by-step procedure:

1. We start with the intersection of areas enclosed by two contours: one of the NH_3 velocity dispersion and one of the NH_3 brightness. First, we find the contour where the NH_3 velocity dispersion ($\sigma_{\rm NH_3}$) has a nonthermal component equal to the thermal component at the median kinetic temperature measured in the targeted region. (See Section 3.2 and Equation (1) for details on the definition of velocity dispersion components.) Second, we select the contour that corresponds to the 10σ level, where the NH_3 brightness ($T_{\rm peak}$) is equal to 10 times the local rms noise, to match the extents of the contiguous regions where successful fits to the NH_3 (1, 1) profiles were found in Friesen et al. (2017). The intersection of the areas enclosed by these two contours is then used to define an initial mask. By this definition, the initial mask encloses a region where we have subsonic velocity dispersion *and* a signal-to-noise ratio greater than 10.
2. We expect the pixels within the mask defined in Step 1 to have a continuous distribution of velocity centroids ($V_{\rm LSR}$). In this step, we remove pixels with $V_{\rm LSR}$ that leads to local velocity gradients (between the targeted pixel and its neighboring pixels within the mask) larger than the overall velocity gradient found for all pixels within the mask by a factor of $\sim$2. This procedure generally removes pixels with local velocity gradients greater than 20–30 $\rm km\,s^{-1}\,pc^{-1}$, which is larger than the velocity gradients known to exist because of realistic physical processes in these regions. The mask editing is done with the aid of Glue.[22]
3. We then check whether the mask from Step 2 contains a single local peak in NH_3 brightness. If there is more than one NH_3 brightness peak, we find the contour level that corresponds to the saddle point between the peaks. This contour level is then used to separate the mask from Step 2 into regions, each of which has a single NH_3 brightness peak. However, if a region has an NH_3 brightness peak no more than three times the local rms noise level above the saddle point, the region is excluded, and only its sibling region with the brighter peak is kept. We examine and categorize the regions excluded in this step as candidates (see below).

[22] A GUI Python library built to explore relationships within and among related data sets, including image arrays (Beaumont et al. 2015; Robitaille et al. 2017). See http://glueviz.org/ for documentation.

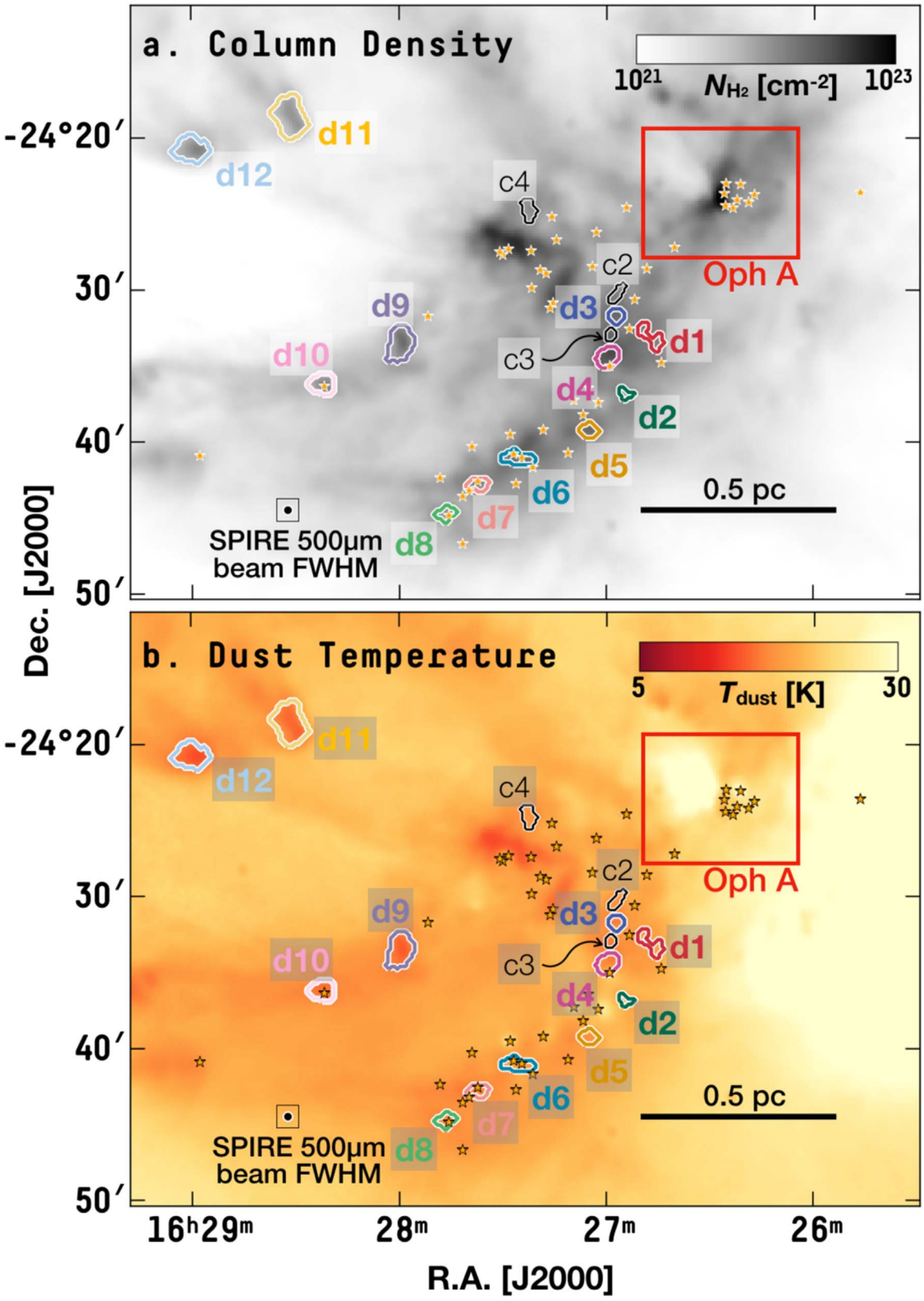

Figure 5. Like Figure 1, but for maps of (a) total column density, N_{H_2}, and (b) dust temperature, T_{dust}, derived from *Herschel* observations.

4. The *Herschel* maps of column density and dust temperature are then used to make sure that the defined structure (a region from Step 3) is centered around a local rise in column density and a dip in dust temperature, consistent with the expectation of dense cores (Crapsi et al. 2007).

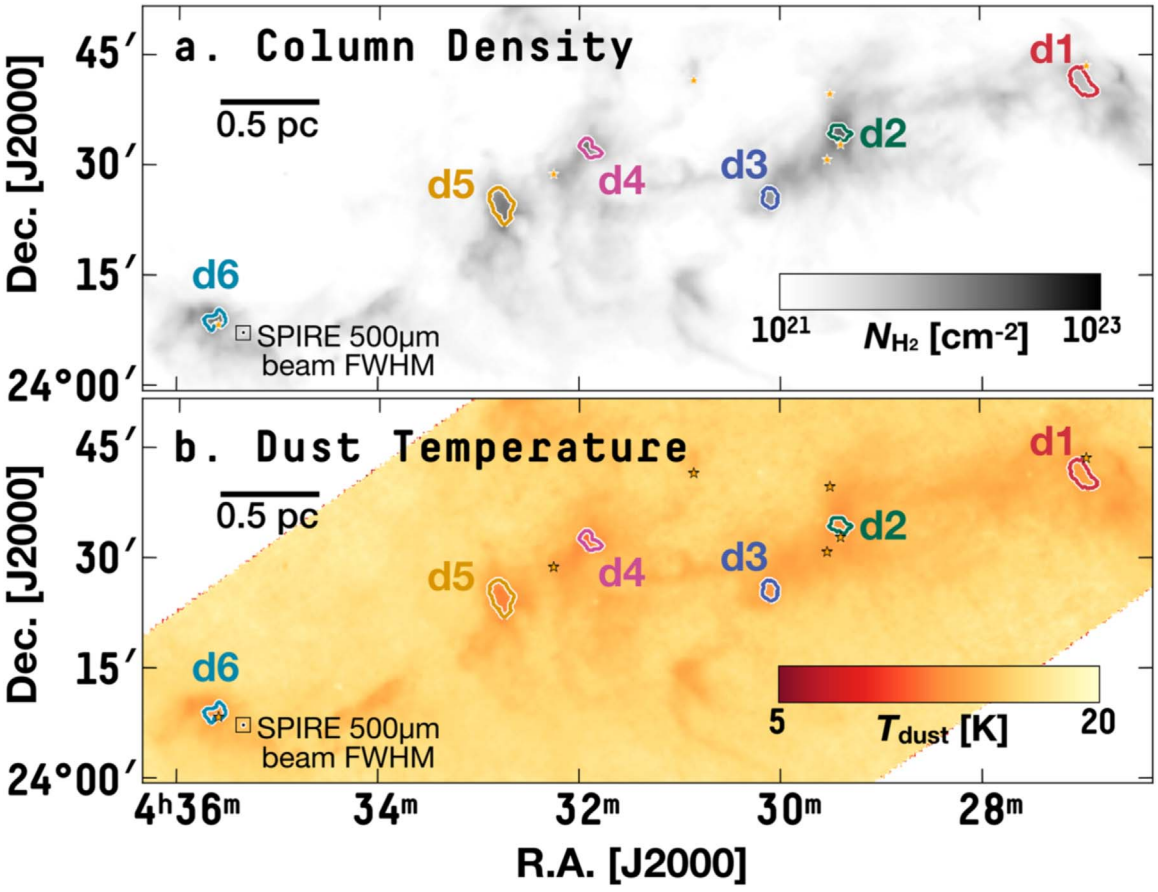

Figure 6. Like Figure 3, but for maps of (a) total column density, N_{H_2}, and (b) dust temperature, T_{dust}, derived from *Herschel* observations.

5. Finally, we make sure that the resulting structure is resolved by the GBT beam at 23 GHz (32″). We impose two criteria: (1) the projected area needs to be larger than a beam, and (2) the effective radius (the geometric mean of the major and minor axes; see Section 3.2) needs to be larger than the beam FWHM.

Using these criteria, we identify 12 coherent structures in L1688 and six coherent structures in B18. In Figures 1–6, the boundaries of the identified coherent structures in L1688 and B18 are shown as colored contours. Although the criteria are consistent with those used by Pineda et al. (2010) to define the coherent core in B5 and do not impose any limits on size, the newly identified coherent structures in L1688 and B18 are generally smaller than previously known coherent cores (see Section 3.2). As mentioned in Section 1, we refer to the newly identified coherent structures as "droplets" for ease of discussion.

As the criteria indicate, each droplet has a high NH_3 peak brightness and a subsonic velocity dispersion—in contrast to the ambient region, where if NH_3 emission is detected, we find a mostly supersonic velocity dispersion and a moderate distribution of NH_3 brightness. Figure 7 shows the distributions of NH_3 line widths and peak NH_3 brightness in main-beam units, for all pixels where there is significant detection of NH_3 emission and for pixels within the droplet boundaries (for the criteria used to determine the significance of detection, see Friesen et al. (2017)). We observe an overall anticorrelation between the observed NH_3 line width and NH_3 brightness, and the relation between the two quantities flattens toward the high NH_3 brightness end when the NH_3 line width approaches a thermally dominated value. The droplets are found in this regime of high NH_3 brightness and thermally dominated NH_3 line widths.

Figure 8 shows the radial profile of NH_3 velocity dispersion; the virtually constant NH_3 velocity dispersion in the interiors is consistent with what Goodman et al. (1998) found for coherent cores (see also Pineda et al. 2010). See Appendix B for a gallery of the close-up views of the droplets.

Two of the 18 droplets, L1688-d11 and B18-d4, are found at the positions of the dense cores analyzed by Goodman et al. (1993), L1696A and TMC-2A, respectively. The two droplets correspond to the central parts of the corresponding dense cores and have radii a factor of ∼0.7 times the radii measured for these dense cores (Benson & Myers 1989; Goodman et al. 1993; Ladd et al. 1994). See Appendix C for a comparison of measured properties.

In Figures 1–6, we also plot the positions of Class 0/I and flat spectrum protostars in the catalogs presented by Dunham et al. (2015) and Rebull et al. (2010), for L1688 and B18, respectively. Within the boundaries of six (out of 18) droplets —L1688-d4, L1688-d6, L1688-d7, L1688-d8, L1688-d10, and B18-d6—we find at least one protostar along the line of sight. Consistent with the results presented by Seo et al. (2015) and Friesen et al. (2009), none of the six droplets where we find protostar(s) within the boundaries show a strong signature of increased T_{kin} or σ_{NH_3} around the protostar(s). While the existence of young stellar objects (YSOs) within the boundary of a droplet in the plane of the sky does not necessarily indicate actual associations of these six droplets with protostars, it is

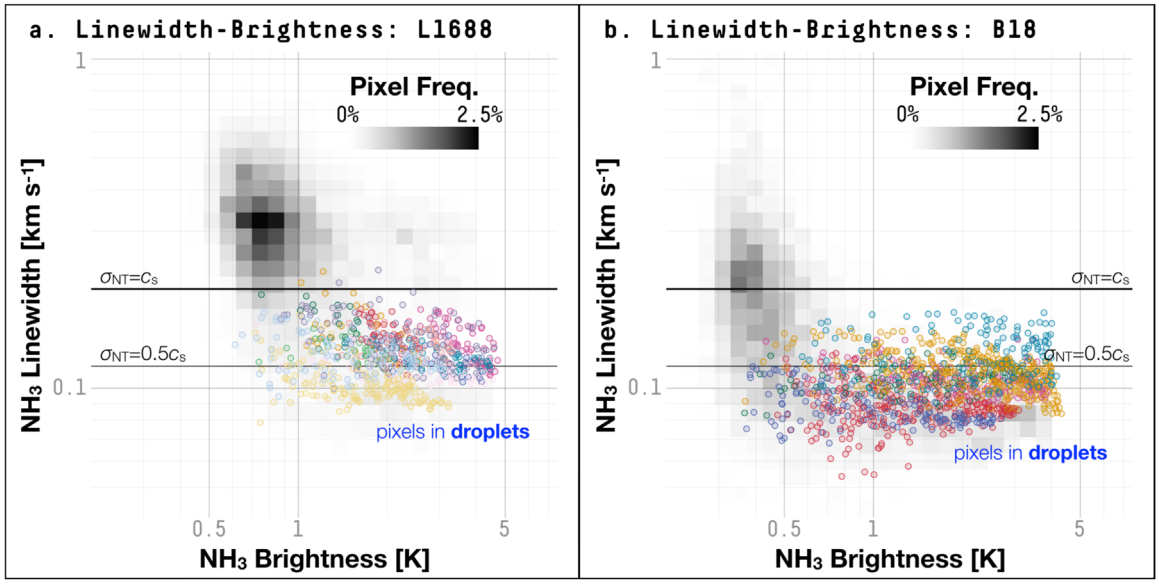

Figure 7. Distributions of NH_3 line widths and peak NH_3 brightness in main-beam units, for every pixel with significant detection of NH_3 (1, 1) emission (a) in L1688 and (b) in B18. The 2D histogram in each panel shows the distribution of pixels in the entire map, with the pixel frequency defined as the percentage of pixels on the map falling in each 2D bin in the 2D histogram. The colored dots are individual pixels inside droplets, with colors matching the contours in Figures 1, 2, and 5 for L1688, and Figures 3, 4, and 6 for B18. The horizontal lines are the expected NH_3 line widths when the nonthermal component of velocity dispersion is respectively equal to the sonic speed (thicker line) and half the sonic speed (thinner line), for a medium with an average particle mass of 2.37 u and a temperature of 10 K.

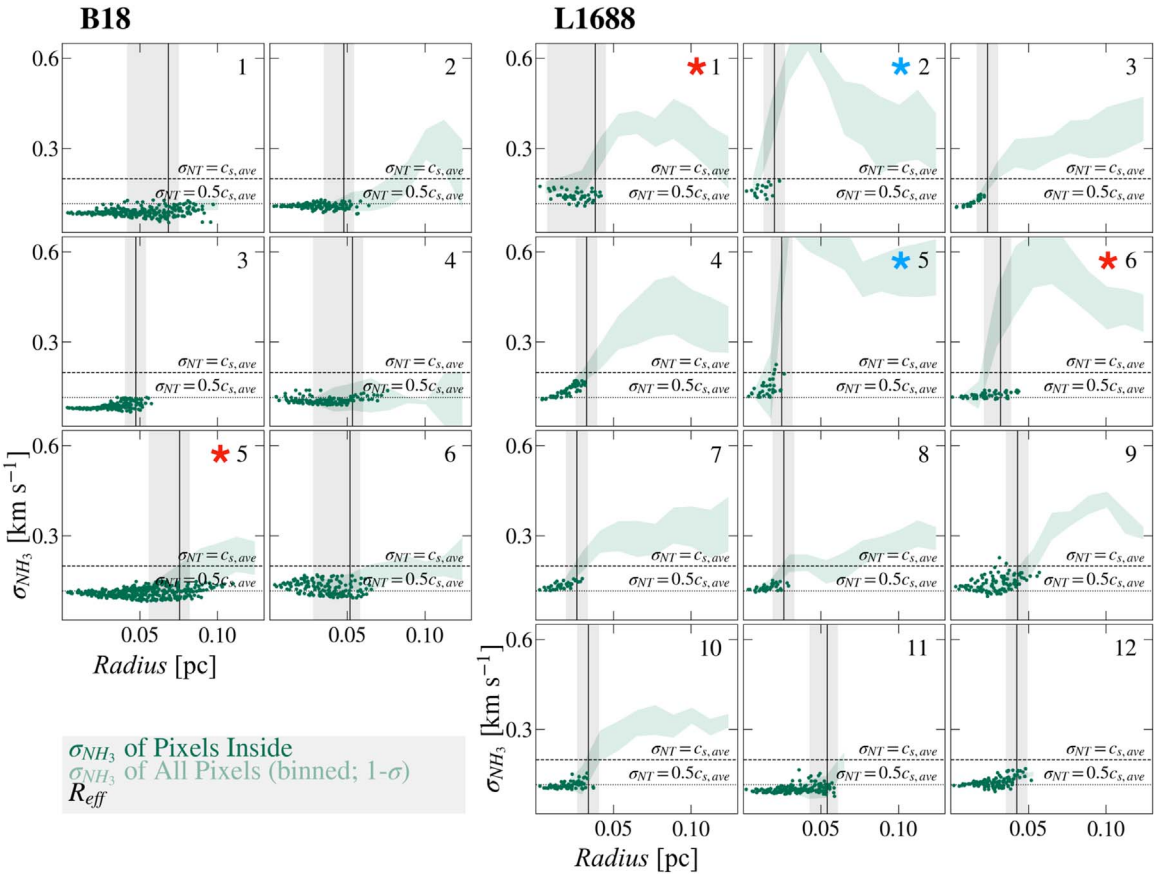

Figure 8. NH_3 velocity dispersion as a function of distance from the center of each droplet. The dark green dots represent individual pixels inside the boundary of each droplet. The transparent green band shows the 1σ distribution of pixels in each distance bin, with a bin size equal to the beam FWHM of GAS observations. The dashed and dotted lines show the expected NH_3 line widths when the velocity dispersion nonthermal component is equal to the sonic speed and half the sonic speed, respectively. The vertical black line marks the effective radius, $R_{\rm eff}$, and the gray vertical band marks the uncertainty in $R_{\rm eff}$. A red asterisk indicates that the droplet has an elongated shape with an aspect ratio larger than 2 that could bias the measurements using equidistant annuli (L1688-d1, L1688-d6, and B18-d5), and a blue asterisk indicates that the droplet sits near the edge of the region where NH_3 emission is detected, resulting in the measurements at larger radii being dominated by fewer pixels (L1688-d2 and L1688-d5).

possible that some of the droplets are associated with at least one YSO. See Section 4.3 for more discussion on the association between cores and YSOs and how it might be used as a way to define subsets of cores.

3.1.1. Droplet Candidates

Apart from the total of 18 droplets identified in L1688 and B18, we also include five *droplet candidates* in L1688 (black contours in Figures 1, 2, and 5). Each droplet candidate is identified by a spatial change from supersonic velocity dispersion outside the boundary to subsonic velocity dispersion inside. However, they do not meet at least one criterion listed above. The detailed reasons why each of these coherent structures is identified as a *droplet candidate*, instead of a droplet, are listed below:

1. L1688-c1E and L1688-c1W: These two droplet candidates are the eastern and western parts of the droplet L1688-d1, each of which has a local peak in NH_3 brightness. However, neither peak is more than three times the local rms noise level above the saddle point between them, i.e., neither satisfies the criterion described in Step 3. Thus, we identify the entire region as a single droplet, L1688-d1, and include the eastern and the western parts of L1688-d1 as two droplet candidates.
2. L1688-c2: This droplet candidate shows a local dip in NH_3 velocity dispersion and a local peak in NH_3 brightness. However, the local peak in NH_3 brightness cannot be separated from the emission in the droplet L1688-d3 by more than three times the local rms noise in NH_3 (1, 1) observations, nor do we find an independent local peak corresponding to L1688-c2 on the *Herschel* column density map. (That is, L1688-c2 does not meet the criteria described in Steps 3 and 4 above.)
3. L1688-c3: Similar to L1688-c2, L1688-c3 shows a local dip in NH_3 velocity dispersion and a local peak in NH_3 brightness. However, the local peak in NH_3 brightness cannot be separated from the emission in the droplet L1688-d4 by more than three times the local rms noise in NH_3 (1, 1) observations, nor do we find an independent local peak corresponding to L1688-c3 on the *Herschel* column density map. While the projected area of L1688-c3 is larger than a beam, its effective radius is only $\sim$2.6 times the beam FWHM. (That is, L1688-c3 does not meet the criteria described in Steps 3–5 above.)
4. L1688-c4: While L1688-c4 does show a significant dip in NH_3 velocity dispersion and an independent peak in NH_3 brightness, it sits close to the edge of the region where the signal-to-noise ratio of the NH_3 (1, 1) emission is sufficient for us to obtain a confident fit to the hyperfine line profile (Friesen et al. 2017). We do not find a strong and independent local peak corresponding to L1688-c4 on the *Herschel* column density map, either. Thus, we classify L1688-c4 as a droplet candidate. (That is, L1688-c4 does not meet the criterion described in Step 4 above.)

In the following analyses, when we discuss the properties of the droplets—or, together with previously known coherent cores, the coherent structures—we exclude the droplet candidates. The droplet candidates are included on the plots to show the distributions of physical properties of potential coherent structures at even smaller scales, which are only marginally resolved by the GAS observations. The Oph A region (marked by the red rectangles in Figures 1, 2, and 5) could potentially host more droplets/droplet candidates. However, Oph A is known to also host a cluster of YSOs—and as Figures 2(b) and 5(b) show, the extent of cold and subsonic dense gas identifiable on the maps of dust temperature and NH_3 velocity dispersion is limited. No coherent structure that satisfies the above criteria can be identified.

The same methods devised here to identify the boundaries and derive the physical properties of the coherent structures in L1688 and in B18 are applied on the data obtained by Pineda et al. (2010) to derive the physical properties of the coherent core in Perseus B5 in the following analyses.

3.1.2. Contrast with Velocity Coherent Filaments

We note that Hacar et al. (2013) and Tafalla & Hacar (2015) used the term "coherent" to describe continuous structures in the position–position–velocity space, with continuous distributions of line-of-sight velocity (V_{LSR}). The method they adopted is a friend-of-friend clustering algorithm and does not impose any criteria on the velocity dispersion. In Step 2, we require a coherent structure to have a continuous distribution of V_{LSR}; ergo, the newly identified coherent structures could theoretically be parts of "velocity coherent filaments." However, the same can be said of any structures that are identified to have continuous structures on the plane of the sky and continuous distributions of line-of-sight velocity. We do not recommend equating the coherent structures, including the newly identified droplets in this work and the coherent cores previously analyzed by Goodman et al. (1998), Caselli et al. (2002), and Pineda et al. (2010), to "velocity coherent filaments" identified by Hacar et al. (2013). Specifically, the droplets and other coherent structures are defined by abrupt drops in velocity dispersion from supersonic to subsonic values around their boundaries, which none of the "velocity coherent filaments" examined by Hacar et al. (2013) show. Moreover, in contrast to the elongated shapes of the "velocity coherent filaments" examined by Hacar et al. (2013), the droplets are mostly round, with aspect ratios generally between 1 and 2. (There are three exceptions: L1688-d1, with an aspect ratio of $\sim$2.50; L1688-d6, with an aspect ratio of $\sim$2.52; and B18-d5, with an aspect ratio of $\sim$2.03. These exceptions are marked with red asterisks on Figure 8).

3.2. Mass, Size, and Velocity Dispersion

With the droplet boundary defined in Section 3.1, we calculate the mass of each droplet using the column density map derived from SED fitting of *Herschel* observations (see Section 2.2). To remove the contribution of line-of-sight material, the minimum column density within the droplet boundary is used as a baseline and subtracted off. The mass is then estimated by summing column density (after baseline subtraction) within the droplet boundary. This baseline subtraction method is similar to the "clipping paradigm" studied by Rosolowsky et al. (2008b), and has been applied by Pineda et al. (2015) to estimate the mass of structures within the coherent core in B5. For the droplets, we find a typical mass[23] of $0.4^{+0.4}_{-0.3}\,M_\odot$. Table 1 lists the mass of each droplet. In Appendix E, we discuss the reasons for adopting the clipping

[23] Unless otherwise noted, the typical value of each physical property presented in this work is the median value of the entire sample of 18 droplets—excluding the droplet candidates—with the upper and lower bounds being the values measured at the 84th and 16th percentiles, which would correspond to ±1 standard deviation around the median value if the distribution is Gaussian.

Table 1
Physical Properties of Droplets and Droplet Candidates

ID[a]	Position [J2000] R.A.	Position [J2000] Decl.	Mass[b] (M) ($M_\odot$)	Effective Radius[c] ($R_{\rm eff}$) (pc)	NH_3 Line Width[d] (σ_{NH_3}) (km s^{-1})	NH_3 Kinetic Temp. ($T_{\rm kin}$) (K)	Total Vel. Dispersion[e] ($\sigma_{\rm tot}$) (km s^{-1})	YSO(s)[f]
L1688-d1	$16^h26^m47\overset{s}{.}07$	$-24°33'8\overset{''}{.}3$	0.17 ± 0.03	$0.038^{+0.007}_{-0.031}$	0.14 ± 0.01	12.0 ± 0.6	0.24 ± 0.01	N
L1688-d2	$16^h26^m54\overset{s}{.}54$	$-24°36'52\overset{''}{.}4$	0.03 ± 0.01	$0.020^{+0.007}_{-0.008}$	0.16 ± 0.01	12.8 ± 0.9	0.25 ± 0.01	N
L1688-d3	$16^h26^m57\overset{s}{.}07$	$-24°31'44\overset{''}{.}8$	0.08 ± 0.03	$0.024^{+0.007}_{-0.007}$	0.12 ± 0.01	10.2 ± 0.3	0.21 ± 0.01	N
L1688-d4	$16^h26^m59\overset{s}{.}59$	$-24°34'28\overset{''}{.}8$	0.73 ± 0.05	$0.033^{+0.007}_{-0.007}$	0.14 ± 0.01	10.6 ± 0.2	0.23 ± 0.01	Y
L1688-d5	$16^h27^m4\overset{s}{.}96$	$-24°39'17\overset{''}{.}6$	0.13 ± 0.03	$0.025^{+0.007}_{-0.007}$	0.14 ± 0.01	12.4 ± 0.6	0.24 ± 0.01	N
L1688-d6	$16^h27^m25\overset{s}{.}50$	$-24°41'6\overset{''}{.}2$	0.22 ± 0.04	$0.032^{+0.018}_{-0.011}$	0.12 ± 0.01	12.6 ± 0.4	0.23 ± 0.01	Y
L1688-d7	$16^h27^m37\overset{s}{.}27$	$-24°42'50\overset{''}{.}2$	0.10 ± 0.02	$0.026^{+0.009}_{-0.007}$	0.13 ± 0.01	13.2 ± 0.4	0.24 ± 0.01	Y
L1688-d8	$16^h27^m46\overset{s}{.}44$	$-24°44'45\overset{''}{.}4$	0.10 ± 0.01	$0.026^{+0.009}_{-0.007}$	0.13 ± 0.01	12.7 ± 0.7	0.23 ± 0.01	Y
L1688-d9	$16^h27^m59\overset{s}{.}43$	$-24°33'33\overset{''}{.}0$	0.55 ± 0.03	$0.043^{+0.021}_{-0.008}$	0.14 ± 0.01	11.2 ± 0.5	0.23 ± 0.01	N
L1688-d10	$16^h28^m22\overset{s}{.}12$	$-24°36'16\overset{''}{.}8$	0.22 ± 0.02	$0.034^{+0.009}_{-0.007}$	0.11 ± 0.01	11.5 ± 0.5	0.22 ± 0.01	Y
L1688-d11	$16^h28^m31\overset{s}{.}53$	$-24°18'36\overset{''}{.}1$	0.46 ± 0.02	$0.054^{+0.010}_{-0.012}$	0.10 ± 0.01	10.1 ± 0.8	0.20 ± 0.01	N
L1688-d12	$16^h28^m59\overset{s}{.}99$	$-24°20'45\overset{''}{.}2$	0.38 ± 0.02	$0.042^{+0.014}_{-0.007}$	0.12 ± 0.01	10.1 ± 0.5	0.21 ± 0.01	N
L1688-c1E[g]	$16^h26^m49\overset{s}{.}36$	$-24°32'39\overset{''}{.}0$	0.02 ± 0.02	$0.020^{+0.007}_{-0.007}$	0.14 ± 0.01	12.4 ± 0.7	0.24 ± 0.01	N
L1688-c1W[h]	$16^h26^m45\overset{s}{.}22$	$-24°33'30\overset{''}{.}5$	0.07 ± 0.02	$0.022^{+0.007}_{-0.007}$	0.15 ± 0.01	11.9 ± 0.5	0.24 ± 0.01	N
L1688-c2	$16^h26^m56\overset{s}{.}89$	$-24°30'18\overset{''}{.}7$	0.10 ± 0.02	$0.024^{+0.011}_{-0.010}$	0.12 ± 0.01	11.3 ± 0.4	0.22 ± 0.01	N
L1688-c3	$16^h26^m58\overset{s}{.}74$	$-24°33'1\overset{''}{.}4$	0.06 ± 0.02	$0.019^{+0.007}_{-0.007}$	0.15 ± 0.01	11.7 ± 0.4	0.24 ± 0.01	N
L1688-c4	$16^h27^m22\overset{s}{.}28$	$-24°24'52\overset{''}{.}2$	0.05 ± 0.02	$0.028^{+0.007}_{-0.007}$	0.12 ± 0.01	12.8 ± 0.9	0.23 ± 0.01	N
B18-d1	$4^h26^m58\overset{s}{.}95$	$24°41'16\overset{''}{.}6$	0.34 ± 0.02	$0.064^{+0.027}_{-0.025}$	0.09 ± 0.01	10.5 ± 1.2	0.20 ± 0.01	N
B18-d2	$4^h29^m24\overset{s}{.}13$	$24°34'42\overset{''}{.}2$	1.24 ± 0.05	$0.045^{+0.021}_{-0.012}$	0.11 ± 0.01	10.0 ± 0.4	0.21 ± 0.01	N
B18-d3	$4^h30^m5\overset{s}{.}71$	$24°25'40\overset{''}{.}6$	0.49 ± 0.02	$0.044^{+0.014}_{-0.007}$	0.08 ± 0.01	9.8 ± 0.9	0.19 ± 0.01	N
B18-d4	$4^h31^m54\overset{s}{.}48$	$24°32'28\overset{''}{.}2$	0.56 ± 0.03	$0.050^{+0.022}_{-0.024}$	0.11 ± 0.01	9.1 ± 0.3	0.20 ± 0.01	N
B18-d5	$4^h32^m46\overset{s}{.}54$	$24°24'51\overset{''}{.}9$	1.87 ± 0.05	$0.071^{+0.034}_{-0.019}$	0.11 ± 0.01	9.5 ± 0.4	0.20 ± 0.01	N
B18-d6	$4^h35^m36\overset{s}{.}32$	$24°9'0\overset{''}{.}7$	0.72 ± 0.04	$0.048^{+0.017}_{-0.022}$	0.13 ± 0.01	9.9 ± 0.3	0.22 ± 0.01	Y

Notes.
[a] L1688-c1E to L1688-c4 are droplet candidates.
[b] Based on the column density map derived from SED fitting of *Herschel* observations. See Section 2.2.
[c] The geometric mean of the $T_{\rm peak}$ weighted spatial dispersions along the major and the minor axes. See Section 3.2. See also Appendix D for details on determining the uncertainties.
[d] The best-fit Gaussian σ.
[e] Derived from NH_3 line widths and kinetic temperatures. See Equation (1).
[f] A value of "Y" means that there is at least one YSO within the droplet boundary defined on the plane of the sky (see Section 3.1), and a value of "N" means that there is no YSO within the droplet boundary. The YSO positions are taken from the catalog presented by Rebull et al. (2010) for B18, and the catalog presented by Dunham et al. (2015) for L1688. Because we are interested in the association between cores/droplets and the YSOs potentially forming inside, only Class 0/I and flat spectrum protostars are considered here.
[g] The eastern part of L1688-d1.
[h] The western part of L1688-d1.

method and the uncertainty therein, and in Appendix F, we examine the uncertainty in mass measurements due to the potential bias in SED fitting.

We define the radius of each droplet based on the NH_3 brightness–weighted second moments along the major and minor axes. We designate the major axis direction as the one with the greatest dispersion in T_{peak} according to a principal component analysis (PCA), and the minor axis is oriented perpendicular to the major axis.[24] The effective radius is then the geometric mean of sizes along the major and minor axes, $R_{eff} = \sqrt{r_{maj} r_{min}}$, where r_{maj} and r_{min} are derived by multiplying the NH_3 brightness–weighted second moments by a factor of $2\sqrt{2\ln 2}$, the scaling factor between the second moment and the FWHM for a Gaussian shape. The multiplication of the scaling factor of $2\sqrt{2\ln 2}$ is done in the same way as the method applied by Benson & Myers (1989) and Goodman et al. (1993) to estimate the radii of dense cores, and is applied to approximate the "true radius" of the droplet.

The resulting effective radii of droplets are listed in Table 1 and have a typical value of 0.04 ± 0.01 pc. The effects of the resolution and the irregular shape of the boundary are included in the uncertainties listed in Table 1. Figure 8 shows that the effective radius, R_{eff}, plotted on top of the radial profile of velocity dispersion, σ_{NH_3}, of each droplet, well-characterizes the change from supersonic to subsonic velocity dispersion. See Appendix B for a comparison between a circle with a radius equal to R_{eff} and the actual boundary of a droplet on the plane of the sky, and see Appendix D for details on estimating the uncertainty and for a discussion on other common ways to derive the "effective radius."

From the GAS observations, we derive the NH_3 velocity dispersion, σ_{NH_3}, and the gas kinetic temperature, T_{kin} (Figures 1–4; see Section 2.1.1 for details). Assuming that the bulk molecular component is in thermal equilibrium with the NH_3 component and assuming also that the nonthermal component of the velocity dispersion is independent of the chemical species observed, we can estimate a total velocity dispersion, σ_{tot}, from the thermal component, σ_T, and the nonthermal (turbulent) component, σ_{NT}:

$$\sigma_{tot}^2 = \sigma_{NT}^2 + \sigma_T^2 \quad (1)$$
$$= \left(\sigma_{NH_3}^2 - \frac{k_B T_{kin}}{m_{NH_3}}\right) + \frac{k_B T_{kin}}{m_{ave}},$$

where k_B is the Boltzmann constant, and m_{NH_3} and m_{ave} are the molecular weight of NH_3 and the mean molecular weight in molecular clouds, respectively. Note that the thermal component, σ_T, is by definition equal to the sonic speed, c_s, in a medium with a particle mass of m_{ave} at a temperature of T_{kin}. Following Kauffmann et al. (2008), we use the mean molecular weight per free particle of 2.37 u (μ_p in Kauffmann et al. 2008).

For each droplet, we obtain characteristic values of the NH_3 velocity dispersion, σ_{NH_3}, and the kinetic temperature, T_{kin}, by taking the median value for the pixels within the droplet boundary on the parameter maps. Following Equation (1), we then estimate σ_{NT}, σ_T, and σ_{tot} for each droplet. Note that σ_{tot} is sometimes referred to as the "1D velocity dispersion," concerning the motions along the line of sight, as opposed to the "3D velocity dispersion," which cannot be observed but can be estimated by multiplying the 1D velocity dispersion by a factor of $\sqrt{3}$ assuming isotropy. We find a typical σ_{tot} of $0.22 \pm 0.02\,km\,s^{-1}$ for the droplets (see Table 1). For reference, the purely thermal velocity dispersion at 10 K is $0.19\,km\,s^{-1}$.

Figure 9 shows the distributions of mass, M, and total velocity dispersion, σ_{tot}, plotted against the effective radius, R_{eff}, of droplets/droplet candidates in comparison with previously known coherent cores as well as other dense cores (see Section 2.3 for details on how the physical properties were estimated for the dense cores). Figure 9(a) shows that droplets seem to fall along the same mass–radius relation as the dense/coherent cores. Using a gradient-based MCMC sampler to find a power-law relation between the mass and effective radius, $M \propto R_{eff}^p$, for all the previously known dense/coherent cores (including B5) and the droplets (excluding droplet candidates), we find a power-law index, $p = 2.4 \pm 0.1$.[25] This exponent lies between those expected for structures with constant surface density, $M \propto R^2$, and those for structures with constant volume density, $M \propto R^3$. As a reference, Larson (1981) found a scaling law, $M \propto R^{1.9}$, for larger-scale molecular structures (with sizes of 0.1–100 pc and masses of $1\,M_\odot$ to $3 \times 10^5\,M_\odot$), using a compilation of observations of molecular line emission from species including ^{12}CO, ^{13}CO, H_2CO, and for a few objects, NH_3, and other N-bearing species.

Figure 9(b) shows the relationship between σ_{tot} and R_{eff}. At scales below 0.1 pc, all structures shown have a subsonic velocity dispersion. The continuity of the distribution of M, R_{eff}, and σ_{tot} between the newly identified coherent structures (droplets) and the previously known coherent cores, as well as other dense cores, suggests that the identification of droplets is robust—and that droplets fall toward the smaller-size end of a potentially continuous population of coherent structures across different size scales. We discuss this continuity in detail, in Section 4.3.

3.3. Virial Analysis: Kinetic Support, Self-gravity, and Ambient Gas Pressure

To investigate the stability of the coherent structures, we follow Pattle et al. (2015) to consider the balance between internal kinetic energy, self-gravity, and the ambient gas pressure, with respect to the equilibrium expression:

$$2\Omega_K = -(\Omega_G + \Omega_P) \quad (2)$$

where Ω_K is the internal kinetic energy, Ω_G is the gravitational potential energy, and Ω_P is the energy term representing the confinement provided by the ambient gas pressure acting on the structure. The "external pressure" comes from thermal and nonthermal (turbulent) motions of the ambient gas (see the analysis in Section 3.3.3). Because we do not have the observations needed to estimate magnetic energy, the magnetic energy term, Ω_M, is omitted (compared to Equation (27) in Pattle et al. (2015)). Here, we focus on pressure exerted on a structure by thermal and nonthermal (turbulent) motions of the ambient gas for Ω_P, and we ignore any contribution of ionizing photons to pressure (see discussions in Ward-Thompson et al. (2006) and Pattle et al. (2015)).

[24] The same process is used to define the major and minor axes in the *Python* package for computing the dendrogram, `astrodendro`. See http://dendrograms.org/ for documentation.

[25] The gradient-based MCMC sampling is implemented using the *Python* package, `PyMC3`. See http://docs.pymc.io/index.html for documentation.

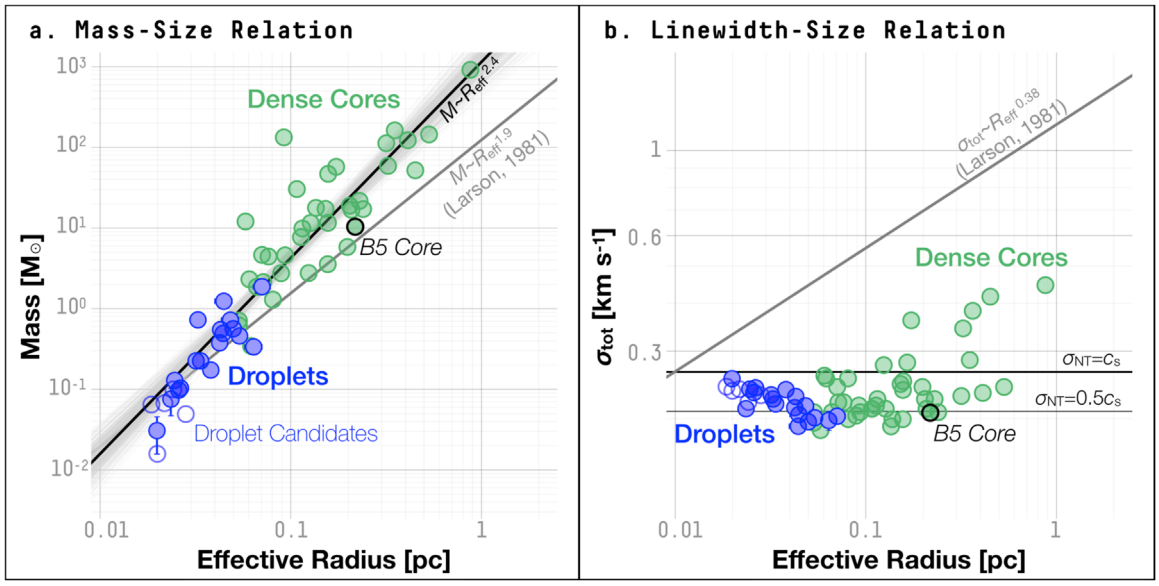

Figure 9. (a) Mass, M, plotted against the effective radius, $R_{\rm eff}$, for dense cores (green circles), the coherent core in B5 (a green circle marked with a black edge), and the newly identified coherent structures: droplets (filled blue circles) and droplet candidates (empty blue circles). The black line shows a power-law relation between the mass and the effective radius, found for both the dense cores (including B5) and the droplets (excluding droplet candidates) by a gradient-based MCMC sampler. A randomly selected 10% of the accepted parameters in the MCMC chain are plotted as transparent lines for reference. The solid gray line shows the empirical relation based on observations of larger-scale structures examined by Larson (1981). (b) The total velocity dispersion, $\sigma_{\rm tot}$, plotted against the effective radius, $R_{\rm eff}$, for the same structures as in (a). The horizontal lines show $\sigma_{\rm tot}$ expected for structures where the nonthermal component is equal to the sonic speed ($c_{\rm s}$; thicker line) and half the sonic speed (thinner line) of a medium with an mean molecular weight of 2.37 u at a temperature of 10 K. The gray line shows an empirical relation adopted from Larson (1981). Here, we convert the line width in the relation presented by Larson (1981) to $\sigma_{\rm tot}$ by assuming that the line width was measured from the CO (1–0) line emission with a gas temperature of 10 K.

3.3.1. Internal Kinetic Energy, Ω_K

The internal kinetic energy, $\Omega_{\rm K}$, is given by:

$$\Omega_{\rm K} = \frac{3}{2} M \sigma_{\rm tot}^2 \tag{3}$$

where M is the mass and $\sigma_{\rm tot}$ is the total velocity dispersion, estimated from the observed NH_3 velocity dispersion, $\sigma_{\rm NH_3}$, and gas kinetic temperature, $T_{\rm kin}$, following Equation (1) (see Section 3.2 for details). The factor of 3 stands for the correction applied to the "1D velocity dispersion," $\sigma_{\rm tot}$, to obtain an estimate of the 3D velocity dispersion, assuming isotropy (see Section 3.2). For droplets, we measure a typical kinetic energy of $4.5^{+5.8}_{-2.8} \times 10^{41}$ erg. Table 2 gives results for each droplet.

3.3.2. Gravitational Potential Energy, Ω_G

Assuming spherical geometry, gravitational potential energy, $\Omega_{\rm G}$, can be estimated from total mass and an effective radius; we adopt a gravitational potential energy expression:

$$\Omega_{\rm G} = \frac{-3}{5} \frac{GM^2}{R_{\rm eff}} \tag{4}$$

where we assume that the sphere of material has a uniform density distribution. In comparison, a sphere of material with a power-law density distribution, $\rho \propto r^{-2}$, has an absolute value of gravitational potential energy, $|\Omega_{\rm G}|$, a factor of $\sim$1.7 larger than that expressed in Equation (4), and a sphere with a Gaussian density distribution has $|\Omega_{\rm G}|$ a factor of $\sim$2 smaller than that expressed in Equation (4) (Pattle et al. 2015; Kirk et al. 2017b). In the following analysis, we include the deviation in $\Omega_{\rm G}$ due to different assumptions of density distributions in the estimated errors. In Section 4.1.1, we show that the density distributions in droplets are nearly uniform at small radii with relatively shallow drops toward the outer edges, validating the assumption of a uniform density distribution used to derive Equation (4).

For droplets, we measure a typical gravitational potential energy of $1.3^{+5.0}_{-1.1} \times 10^{41}$ erg (absolute value; see Table 2). Figure 10(a) shows that most of the dense cores, including previously known coherent cores such as the one in B5, are close to an equilibrium between the gravitational potential energy and the internal kinetic energy. This indicates that the self-gravity of these coherent cores is substantial and may provide the binding force needed to keep the cores from dispersing. On the other hand, gravity in the newly identified droplets appears to be less dominant compared to the internal kinetic energy. For most of the droplets, the internal kinetic energy is close to an order of magnitude larger than the gravitational potential energy.

That larger structures have more dominant gravitational potential energies than smaller structures is expected for structures with a nearly flat $\sigma_{\rm tot}$-size relation and a steep mass–size relation (Figure 9). For the coherent structures under discussion, we observe a power-law mass–size relation, $M \propto R_{\rm eff}^{2.4}$, and with a constant $\sigma_{\rm tot}$, we would expect a power-law relation between the gravitational potential energy and the size, $|\Omega_{\rm G}| \propto R_{\rm eff}^{3.8}$, and a power-law relation between the internal kinetic energy and the size, $\Omega_{\rm K} \propto R_{\rm eff}^{2.4}$. Consequently, a smaller coherent structure would have a smaller ratio between the gravitational potential energy and the internal kinetic energy, $|\Omega_{\rm G}|/\Omega_{\rm K}$. For reference, structures with a constant $|\Omega_{\rm G}|/\Omega_{\rm K}$ are expected to have a mass–size relation of $M \propto R_{\rm eff}$.

Table 2
Virial Properties of Droplets and Droplet Candidates

ID[a]	Internal Kinetic Energy[b] (Ω_K) (erg)	Gravitational Potential Energy[c] ($\lvert\Omega_G\rvert$) (erg)	Ambient Gas Pressure[d] (P_{amb}/k_B) (K cm^{-3})	Energy Term for Ambient Pressure[e] ($\lvert\Omega_P\rvert$) (erg)
L1688-d1	$2.9 \pm 0.5 \times 10^{41}$	$4.0^{+2.7}_{-2.0} \times 10^{40}$	$7.0 \pm 0.7 \times 10^{5}$	$2.0 \pm 0.3 \times 10^{42}$
L1688-d2	$5.9 \pm 2.9 \times 10^{40}$	$2.4^{+1.6}_{-2.4} \times 10^{39}$	$8.4 \pm 1.3 \times 10^{5}$	$3.3 \pm 0.6 \times 10^{41}$
L1688-d3	$1.0 \pm 0.4 \times 10^{41}$	$1.2^{+0.8}_{-0.9} \times 10^{40}$	$6.8 \pm 0.7 \times 10^{5}$	$4.5 \pm 0.6 \times 10^{41}$
L1688-d4	$1.1 \pm 0.1 \times 10^{42}$	$8.3^{+5.5}_{-4.1} \times 10^{41}$	$6.7 \pm 0.8 \times 10^{5}$	$1.2 \pm 0.2 \times 10^{42}$
L1688-d5	$2.2 \pm 0.5 \times 10^{41}$	$3.4^{+2.3}_{-1.7} \times 10^{40}$	$1.5 \pm 0.2 \times 10^{6}$	$1.1 \pm 0.2 \times 10^{42}$
L1688-d6	$3.6 \pm 0.6 \times 10^{41}$	$8.1^{+5.4}_{-4.1} \times 10^{40}$	$9.7 \pm 1.4 \times 10^{5}$	$1.6 \pm 0.3 \times 10^{42}$
L1688-d7	$1.8 \pm 0.3 \times 10^{41}$	$2.1^{+1.4}_{-1.0} \times 10^{40}$	$4.1 \pm 0.6 \times 10^{5}$	$3.8 \pm 0.6 \times 10^{41}$
L1688-d8	$1.6 \pm 0.2 \times 10^{41}$	$1.9^{+1.3}_{-0.9} \times 10^{40}$	$2.7 \pm 0.4 \times 10^{5}$	$2.4 \pm 0.4 \times 10^{41}$
L1688-d9	$8.5 \pm 0.6 \times 10^{41}$	$3.6^{+2.4}_{-1.8} \times 10^{41}$	$2.6 \pm 0.5 \times 10^{5}$	$1.1 \pm 0.2 \times 10^{42}$
L1688-d10	$3.2 \pm 0.3 \times 10^{41}$	$7.7^{+5.1}_{-3.8} \times 10^{40}$	$2.8 \pm 0.5 \times 10^{5}$	$5.4 \pm 1.0 \times 10^{41}$
L1688-d11	$5.5 \pm 0.5 \times 10^{41}$	$2.0^{+1.3}_{-1.0} \times 10^{41}$	$5.0 \pm 1.0 \times 10^{4}$	$4.0 \pm 0.9 \times 10^{41}$
L1688-d12	$5.1 \pm 0.4 \times 10^{41}$	$1.7^{+1.1}_{-0.9} \times 10^{41}$	$9.7 \pm 1.3 \times 10^{4}$	$3.8 \pm 0.6 \times 10^{41}$
L1688-c1E[f]	$2.6 \pm 3.3 \times 10^{40}$	$6.5^{+4.3}_{-6.5} \times 10^{38}$	$7.7 \pm 0.8 \times 10^{5}$	$3.1 \pm 0.4 \times 10^{41}$
L1688-c1W[g]	$1.1 \pm 0.3 \times 10^{41}$	$1.1^{+0.7}_{-0.6} \times 10^{40}$	$7.8 \pm 0.8 \times 10^{5}$	$4.1 \pm 0.6 \times 10^{41}$
L1688-c2	$1.5 \pm 0.3 \times 10^{41}$	$2.1^{+1.4}_{-1.1} \times 10^{40}$	$6.4 \pm 0.7 \times 10^{5}$	$4.6 \pm 0.7 \times 10^{41}$
L1688-c3	$1.1 \pm 0.4 \times 10^{41}$	$1.2^{+0.8}_{-0.9} \times 10^{40}$	$7.9 \pm 0.8 \times 10^{5}$	$2.6 \pm 0.4 \times 10^{41}$
L1688-c4	$7.8 \pm 3.0 \times 10^{40}$	$4.4^{+2.9}_{-3.3} \times 10^{39}$	$1.2 \pm 0.1 \times 10^{6}$	$1.3 \pm 0.2 \times 10^{42}$
B18-d1	$3.9 \pm 0.5 \times 10^{41}$	$9.1^{+6.0}_{-4.5} \times 10^{40}$	$6.8 \pm 1.2 \times 10^{4}$	$9.0 \pm 3.3 \times 10^{41}$
B18-d2	$1.5 \pm 0.1 \times 10^{42}$	$1.8^{+1.2}_{-0.9} \times 10^{42}$	$1.8 \pm 0.3 \times 10^{5}$	$8.2 \pm 3.0 \times 10^{41}$
B18-d3	$5.4 \pm 0.5 \times 10^{41}$	$2.8^{+1.9}_{-1.4} \times 10^{41}$	$1.2 \pm 0.1 \times 10^{5}$	$5.2 \pm 1.7 \times 10^{41}$
B18-d4	$6.5 \pm 0.4 \times 10^{41}$	$3.3^{+2.2}_{-1.6} \times 10^{41}$	$6.6 \pm 0.9 \times 10^{4}$	$4.2 \pm 1.4 \times 10^{41}$
B18-d5	$2.3 \pm 0.1 \times 10^{42}$	$2.5^{+1.7}_{-1.3} \times 10^{42}$	$1.4 \pm 0.3 \times 10^{5}$	$2.5 \pm 1.0 \times 10^{42}$
B18-d6	$1.0 \pm 0.1 \times 10^{42}$	$5.5^{+3.7}_{-2.8} \times 10^{41}$	$1.8 \pm 0.4 \times 10^{5}$	$1.0 \pm 0.4 \times 10^{42}$

Notes.
[a] L1688-c1E to L1688-c4 are droplet candidates.
[b] See Equation (3).
[c] A potential energy, with the zero point defined at infinity. The effects of various assumptions regarding the geometry are considered in error estimation. Absolute values are listed in this table. See Equation (4) and the text.
[d] Measured in the region immediately outside each droplet. See Equation (6).
[e] A potential energy, with the zero point defined at equilibrium. Absolute values are listed in this table. See Equation (5).
[f] The eastern part of L1688-d1.
[g] The western part of L1688-d1.

The above comparison between the gravitational potential energy and the internal kinetic energy, without considering the ambient turbulent pressure, is analogous to an analysis of stability using a virial parameter, $\alpha_{vir} = \frac{a\sigma_{tot}^2 R_{eff}}{GM}$, where the leading factor, a, varies according to the assumption of the density distribution (e.g., $a = 5$ for a spherical structure with a uniform density, and $a = 3$ for a spherical structure with a power-law density profile with an index of 2, $\rho \propto r^{-2}$; see Bertoldi & McKee (1992)). Conventionally, structures with $\alpha_{vir} \leqslant 2$ would be considered "gravitationally bound." By this measure, only the most massive droplets (with masses on the order of $1\,M_\odot$) along with most of the dense cores are "gravitationally bound" (Figure 10(a)).

3.3.3. Energy Term Representing Ambient Pressure Confinement, Ω_P

The pressure term, Ω_P, in the virial equation (Equation (2)) is characteristic of the pressure exerted on a structure by thermal and nonthermal (turbulent) motions of the ambient gas. To avoid the impression that there is a clear-cut boundary between the interior and the exterior of the targeted structure, we call the pressure provided by the ambient gas motions the "ambient gas pressure," P_{amb}, which is sometimes called the "external pressure" and denoted by P_{ext} in previous works (Ward-Thompson et al. 2007; Pattle et al. 2015; Kirk et al. 2017b).

For a spherical structure with a radius of R_{eff}, the pressure term is given by

$$\Omega_P = -3P_{amb}V = -4\pi P_{amb}R_{eff}^3\,, \quad (5)$$

where P_{amb} is the ambient gas pressure and V is the volume of the structure under discussion (Ward-Thompson et al. 2006; Pattle et al. 2015). The pressure exerted on the structure can be estimated from

$$P_{amb} = \rho_{amb}\sigma_{tot,amb}^2, \quad (6)$$

where ρ_{amb} is the volume density of the ambient gas and $\sigma_{tot,amb}$ is the total velocity dispersion, including both thermal and nonthermal motions of the ambient gas (same as σ_{tot} defined in Equation (1) for the gas in the core). The leading factor of 3 in Equation (5) is applied to estimate the effects of gas motions in the 3D space, because for $\sigma_{tot,amb}$, we use the "1D (line-of-sight)

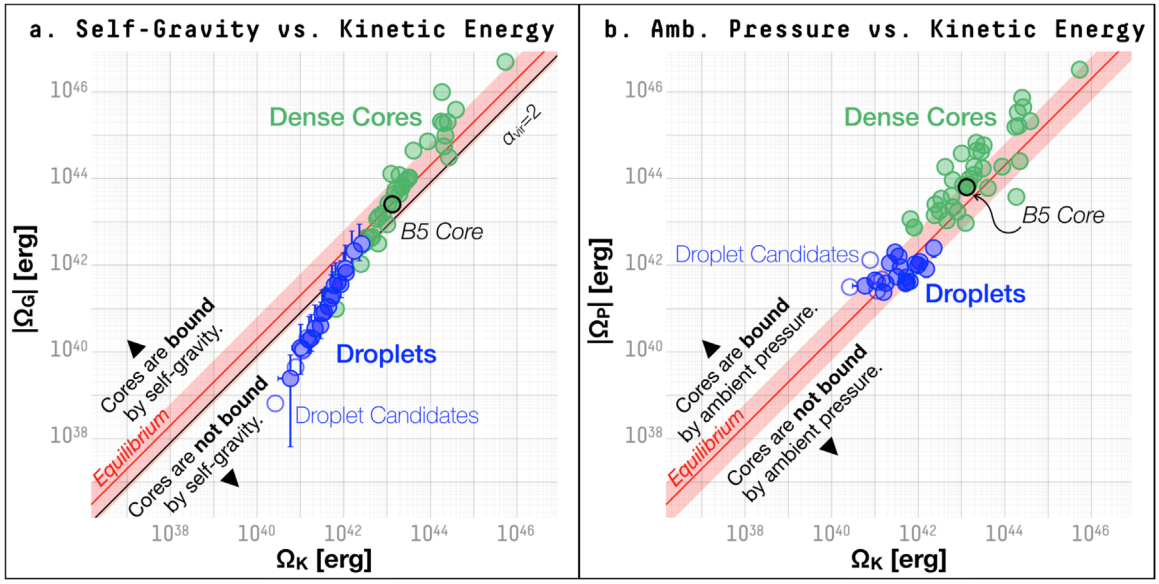

Figure 10. (a) Gravitational potential energy, Ω_G, plotted against internal kinetic energy, Ω_K, for dense cores (green circles), the coherent core in B5 (a green circle marked with a black edge), and the newly identified coherent structures: droplets (filled blue circles) and droplet candidates (empty blue circles). The red band from the lower left to the top right marks the equilibrium between Ω_G and Ω_K (solid red line) within an order of magnitude (pink band). The black line marks where the conventional virial parameter, α_{vir}, has a value of 2. (b) The energy term representing the confinement provided by the ambient gas pressure, Ω_P, plotted against the internal kinetic energy, Ω_K, for the same structures shown in (a). Similarly, the red band from the lower left to the top right marks an equilibrium between Ω_P and Ω_K (solid red line) within an order of magnitude (pink red band).

Table 3
External Pressure of Droplets Compared to Previous Works[a]

	Region	P_{amb}/k_B[b] (K cm^{-3})	Ω_P[b=c] (erg)	Sizes of Targeted Structures (pc)	Tracer of σ_{amb}	$n_{amb} = \rho_{amb}/m_{ave}$[d] (cm^{-3})
Droplets	Oph/Tau	$2.7^{+4.7}_{-1.8} \times 10^5$	$6.8^{+3.0}_{-6.3} \times 10^{41}$	0.02–0.08	NH_3 (1, 1)	*Herschel* N_{H_2}
B5	Per	1.2×10^5	6.3×10^{43}	0.2	NH_3 (1, 1)	*Herschel* N_{H_2}
Johnstone et al. (2000)	Oph	2×10^7	(2.2×10^{41}–1.3×10^{44})	0.006–0.05	CO (1–0)	3×10^4
Lada et al. (2008)	Pipe	5×10^4	(3.2×10^{41}–4.5×10^{43})	0.05–0.26	^{13}CO (1–0)	1×10^3
Maruta et al. (2010)	Oph	3×10^6	(1.6×10^{42}–5.0×10^{43})	0.022–0.069	$H^{13}CO^+$ (1–0)	$(0.5–1.0) \times 10^5$
Pattle et al. (2015)	Oph	1.8×10^7	9×10^{41}	0.01	$C^{18}O$ (3–2)	$\leqslant 1 \times 10^5$
Kirk et al. (2017b)	Ori	9.5×10^5	(2.7×10^{41}–1.1×10^{44})	0.017–0.13	$C^{18}O$ (1–0)	5×10^3

Notes.
[a] This table compares estimates of the ambient pressure and the corresponding virial energy term presented in Section 3.3.3 with previous estimates for other density structures found in molecular clouds. We only include estimates based on direct observations of the velocity dispersion of the ambient material in this table, and it is by no means meant to be comprehensive. Other efforts to estimate the ambient pressure include the work presented by Seo et al. (2015), where estimates are made by modeling the surface pressure using measurements at the peripheries of cores, and that presented by Fischera & Martin (2012), where estimates are made for filamentary structures based on surface brightness models of near-equilibrium cylinders, for example. See discussion in Section 3.3.3.
[b] The pressure due to the thermal and nonthermal motions of the gas surrounding the targeted structures. See Section 3.3.3 for details.
[c] The energy term is calculated according to Equation (5). Numbers in parentheses are not reported by the original authors and are instead derived here based on the ambient gas pressures and the radii of corresponding structures.
[d] For each of the droplets and the coherent core in B5, the density of the ambient gas is estimated based on the *Herschel* column density map. Other works derived the ambient gas density by assuming a "critical density" that the velocity dispersion tracer traces. The number density assumed to be traced by the ambient gas tracer is listed for reference.

velocity dispersion" measured from observations. See the discussion in Section 3.2.

We base our calculation of the pressure, P_{amb}, on the maps of σ_{NH_3} and T_{kin} from fitting the NH_3 hyperfine line profiles (for estimating $\sigma_{tot,amb}$; Figures 1–4) and the *Herschel* column density maps (for estimating ρ_{amb}; Figures 5 and 6). The former is possible because there is significant detection of NH_3 (1, 1) emission in regions surrounding the droplets and the coherent core in B5, which appear embedded in the dense gas components of the clouds (see Figures 2 and 4). We use the region (on the plane of the sky) immediately outside the targeted structure but within (R_{eff} + 0.1) pc from the center of the structure to obtain an estimate of the ambient gas pressure. Because the typical sonic scale in nearby molecular clouds is roughly 0.1 pc (Federrath 2013), our hope is that the selected region represents the projection of the volume within a sonic scale from the surface of the structure and that the estimated pressure is from the motions of the gas relevant in confining the structure. The volume density

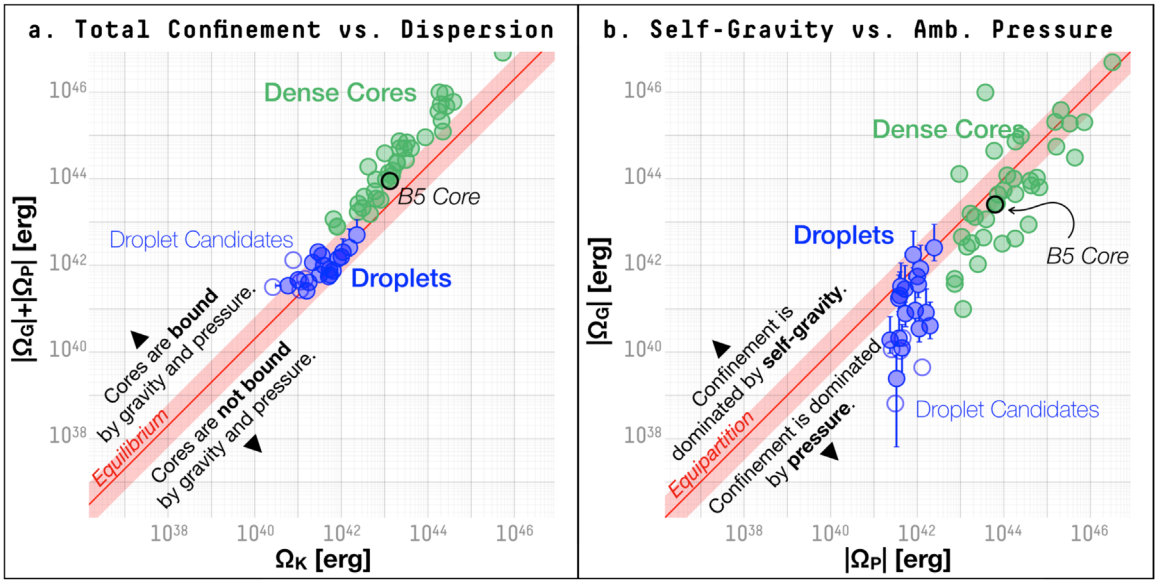

Figure 11. (a) Sum of gravitational potential energy, Ω_G, and the energy term representing the confinement provided by the ambient gas, Ω_P, plotted against the internal kinetic energy, Ω_K, for dense cores (green circles), the coherent core in B5 (a green circle marked with a black edge), and the newly identified coherent structures: droplets (filled blue circles) and droplet candidates (empty blue circles). The red band from the lower left to the top right marks the equilibrium between the sum of confining terms and the internal kinetic energy (solid red line) within an order of magnitude (pinkish red band). (b) The gravitational potential energy, Ω_G, plotted against the ambient pressure energy, Ω_P, for the same structures as in (a). The red band from the lower left to the top right marks an equipartition between Ω_G and Ω_P.

of the ambient gas is estimated in the same fashion as demonstrated above in Section 3.2 and Figure 27, by taking the difference between the mass measured within $(R_{\rm eff}+0.1)$ pc from the core center, $\Delta M = M\,(r < (R_{\rm eff}+0.1\ {\rm pc})) - M_{\rm core}$, and dividing it by the difference in volume assuming a spherical geometry, $\Delta V = \frac{4}{3}\pi((R_{\rm eff}+0.1\ {\rm pc})^3 - R_{\rm eff}^3)$. The total velocity dispersion of the ambient gas, $\sigma_{\rm tot,amb}$, is estimated by taking the median value of $\sigma_{\rm tot}$ measured at pixels within the same projected region (outside the core, but within $(R_{\rm eff}+0.1)$ pc from the core center). For cores where we do not have significant detection toward every pixel within this projected region, we estimate an uncertainty up to $\lesssim$50%. We emphasize that the measurement of the ambient gas pressure and the energy term representing the ambient gas pressure, Ω_P, using this method is independent of the measurement of the kinetics within the core (e.g., $\sigma_{\rm tot}$ and the internal kinetic energy, Ω_K), because nonoverlapping projected regions are used for the measurements. We also note that, in contrast to previous works, it is possible to measure the local variation in ambient gas pressure through this method with the GAS observations (Friesen et al. 2017; Kirk et al. 2017b).

Plugging the measured $\rho_{\rm amb}$ and $\sigma_{\rm tot,amb}$ in Equation (6), we get a typical value of $P_{\rm amb}/k_{\rm B} \approx 2.7^{+4.7}_{-1.8} \times 10^5\,{\rm K\,cm^{-3}}$ for the droplets (see Table 2 for the result of each droplet) and $P_{\rm amb}/k_{\rm B} \approx 1.2 \times 10^5\,{\rm K\,cm^{-3}}$ for the coherent core in B5. Following Equation (5), we then estimate the virial energy term corresponding to the ambient pressure confinement of the droplets to be $|\Omega_P| \approx 6.8^{+3.0}_{-6.3} \times 10^{41}$ erg and that of the coherent core in B5 to be $|\Omega_P| \approx 6.3 \times 10^{43}$ erg. See Table 2 for the estimated $P_{\rm amb}/k_{\rm B}$ and Ω_P of each droplet.

Since the 1980s, there have been efforts to find predominantly pressure-confined structures and to estimate the magnitude of such pressure confinement. The earlier works focused on estimating the magnitude of "inter-clump" pressure based on models of pressure-confined clumps (Keto & Myers 1986; Bertoldi & McKee 1992). These models of pressure-confined clumps often presumed an equilibrium between the internal kinetic energy, the gravitational potential energy, and the energy terms representing pressure confinement through various physical processes. For example, using observations of molecular line emission and extinction to estimate the kinetic energy and the gravitational potential energy of dense clumps, Keto & Myers (1986) estimated that an inter-clump pressure, $P/k_{\rm B}$, between $10^{3.5}$ and $10^{4.5}\,{\rm K\,cm^{-3}}$ was needed to keep the dense clumps at virial equilibrium. In a similar fashion, Bertoldi & McKee (1992) estimated that the "molecular cloud pressure" acting on the dense clumps within the molecular cloud ranged from $1.2 \times 10^4\,{\rm K\,cm^{-3}}$ in Cepheus to $1.1 \times 10^5\,{\rm K\,cm^{-3}}$ in Ophiuchus, balancing the observed internal pressure in both cases. Because of the relatively coarse resolution available at that time, these works focused on clumps with sizes between ~0.5 and 1.0 pc.

At smaller size scales, work has been done to estimate the core confining pressure using direct observations of velocity dispersion in the host molecular clouds. An incomplete summary is provided in Table 3; examples include Johnstone et al. (2000), Lada et al. (2008), Maruta et al. (2010) and Kirk et al. (2017b). In these works, observations of molecular line emission were devised to estimate the velocity dispersion. Then, by assuming that the molecular line emission traces a certain (range of) density, the pressure was estimated by equations similar to Equation (6). While these works found a large range of gas pressure from $P_{\rm amb}/k_{\rm B} \approx 5 \times 10^4\,{\rm K\,cm^{-3}}$ to $2 \times 10^7\,{\rm K\,cm^{-3}}$ for structures with sizes from 0.006 to 0.26 pc, they similarly concluded that a substantial portion of the targeted structures were pressure-confined. However, these works were limited by the lack of observations suitable for estimating the variation in the confining pressure from structure to structure.

Notably, previous analyses done by Pattle et al. (2015) of structures in Ophiuchus with sizes slightly smaller than the droplets gave an estimate of the ambient pressure two orders of

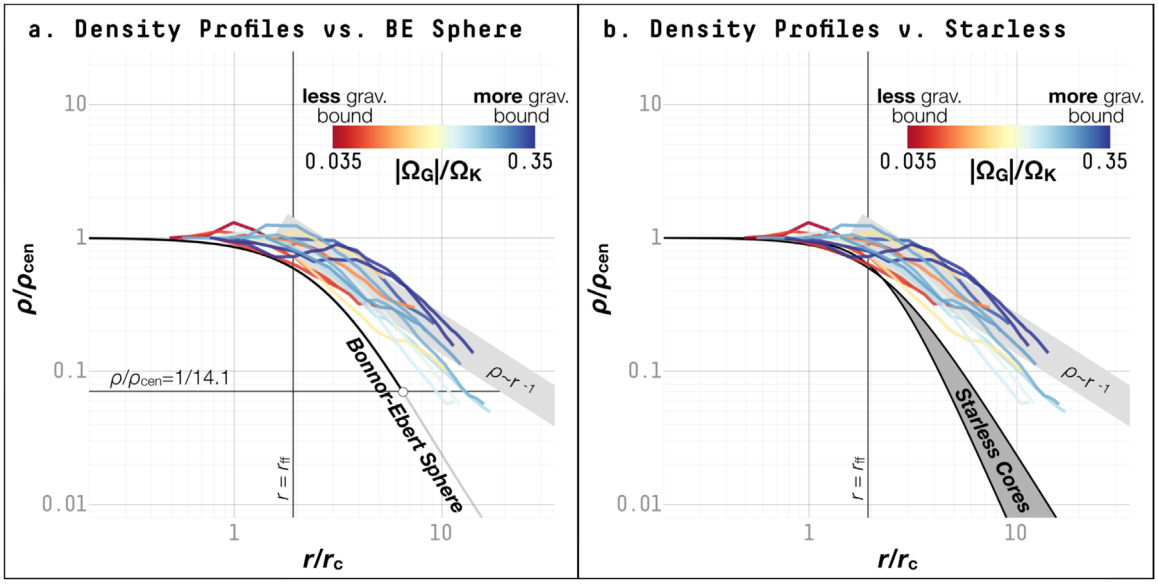

Figure 12. (a) Radial profile of volume density in normalized units of each droplet, compared to a critical Bonnor–Ebert density profile. Each curve is the average radial profile of a droplet, color coded according to the ratio between gravitational potential energy and internal kinetic energy. The thick black curve plots the density profile of a critical Bonnor–Ebert sphere, and the lower horizontal line marks the critical contrast in volume density. The light gray band shows the slope of a density profile as a power-law function of the radius, $\rho \propto r^{-1}$. The vertical gray line marks the freefall length scale, $r_{\rm ff}$. (b) Same as (a), the radial profile of volume density in normalized units of each droplet, this time plotted as a dark gray band against previous observations of starless cores (Tafalla et al. 2004). Because the dumbbell shape of L1688-d1 affects this analysis, which assumes spherical geometry, L1688-d1 is not included in these plots. The typical uncertainty for each volume density measurement along a density profile is ∼25%.

magnitude larger than that estimated for the droplets. However, Pattle et al. (2015) found $|\Omega_{\rm P}| \approx 9 \times 10^{41}$ erg for the same structures, which was comparable to the typical value found for the droplets, $|\Omega_{\rm P}| \approx 7.6 \times 10^{41}$ erg. This is because the estimation of the virial energy term, $\Omega_{\rm P}$, representing the confinement provided by the ambient gas pressure, is dominated by the size of the targeted structure, $\Omega_{\rm P} \propto R^3$ (Equation (5)), and so a size difference of a factor of 2 amounts to roughly an order of magnitude difference in $\Omega_{\rm P}$. Similarly, Johnstone et al. (2000) found a larger ambient gas pressure, $P_{\rm amb}/k_{\rm B} \approx 2 \times 10^7\,{\rm K\,cm^{-3}}$, and a comparable energy term, $|\Omega_{\rm P}| \approx 2.2 \times 10^{41}$ to 1.3×10^{44} erg, for even smaller structures with sizes between 0.006 and 0.05 pc. On the other hand, Maruta et al. (2010) found both an ambient pressure larger than that estimated for the droplets, $P_{\rm amb}/k_{\rm B} \approx 3 \times 10^6\,{\rm K\,cm^{-3}}$, and a pressure energy term larger than that estimated for the droplets, $|\Omega_{\rm P}| \approx 1.6 \times 10^{42}$ to 5.0×10^{43} erg, for structures in Ophiuchus with sizes of 0.022–0.069 pc. To some extent, the difference between the ambient gas pressure estimated in this work for the droplets and the gas pressure estimated for structures in the same region given by previous works can be attributed to the effects of a large uncertainty in the assumed critical density. Moreover, in previous works, the tracer used for estimating the gas pressure is usually different from the tracer used to define the structures themselves. This could result in the estimated gas pressure deviating from the actual local ambient gas pressure that is relevant in confining the structures under discussion.

Figure 10(b) shows a comparison between the kinetic energy and the energy term representing the ambient pressure confinement. Before including the gravitational potential energy (due to self-gravity acting as a confining force; see Equation (2)), it already seems that the ambient gas pressure is substantial in both the droplets and the dense cores compared to the kinetic energy. Here, for the dense cores, due to the lack of molecular line observations of the ambient gas, we follow Kirk et al. (2017b) and adopt a single value of $P_{\rm amb}/k_{\rm B} = 9.5 \times 10^5\,{\rm K\,cm^{-3}}$ based on observations of $C^{18}O$ (1–0) emission in nearby molecular clouds. The result is consistent with the conclusion drawn by Johnstone et al. (2000) that the ambient gas pressure is "instrumental" in confining the dense structures in the Ophiuchus cloud.

It is worth mentioning that a similar effort to obtain the local turbulent pressure structure-by-structure is done by Seo et al. (2015) for cores identified in the B218 region in Taurus. Seo et al. (2015) used the velocity dispersion and column density measurements at the circumference of the targeted core to estimate the work done by the ambient gas pressure, $W_{\rm amb} \approx 5 \times 10^{40}$ to 1×10^{42} erg; by assuming that the density distribution of the core follows the density profile of a critical Bonnor–Ebert sphere, Seo et al. (2015) estimated that the pressure at the surface of the core is $P/k_{\rm B} \approx 8 \times 10^5\,{\rm K\,cm^{-3}}$. Both numbers are similar to the numbers we get for the droplets, and similarly, Seo et al. (2015) conclude that some of the cores in the B218 region are pressure-confined. A similar value of the ambient pressure, $P/k_{\rm B} \approx 2 \times 10^4\,{\rm K\,cm^{-3}}$, is found structure-by-structure for filamentary structures in molecular clouds by Fischera & Martin (2012), by modeling *Herschel* surface brightness profiles with near-equilibrium cylinders. See discussion in Section 4.3.

3.3.4. Full Virial Analysis

Combining the estimates of $\Omega_{\rm K}$, $\Omega_{\rm G}$, and $\Omega_{\rm P}$, we can assess the balance between the internal kinetic energy and the sum of "confining forces" in the form of the gravitational potential energy and the energy term representing the confinement provided by the ambient gas motions (Equation (2)). Figure 11(a) shows the distribution of the sum of the energy terms on the right-hand side of Equation (2) ($\Omega_{\rm G}$ and $\Omega_{\rm P}$) plotted against the internal kinetic energy, $\Omega_{\rm K}$. Both the newly

identified droplets and the dense cores appear to be virially bound (by self-gravity and the ambient gas pressure combined) or at least within an order of magnitude around an equilibrium. The dense cores appear to have the sum of Ω_G and Ω_P roughly half an order of magnitude larger than Ω_K. By contrast, the newly identified droplets and droplet candidates appear to be slightly closer to an equilibrium between the internal kinetic energy and the sum of energy terms representing the confining forces. That is, Equation (2) holds for the droplets within an order of magnitude.

In Figure 11(b), we examine the equipartition between the gravitational potential energy, Ω_G, and the energy term measuring the confinement provided by the ambient gas pressure, Ω_P. Most of the coherent cores, including the droplets, have $|\Omega_P| \geqslant |\Omega_G|$, showing that the ambient gas pressure is substantial even for dense cores—which are often gravitationally bound. The full results from the virial analysis are listed in Table 2, and we discuss the nature of the confinement provided by the ambient gas pressure in Section 4.1.

4. Discussion

4.1. Nature of the Pressure Confinement

The fact that the newly identified coherent structures, *droplets*, are dominated by the ambient gas pressure but relatively less so by self-gravity (Section 3.3; see also Figures 10 and 11) seems to suggest that the confinement of the droplets is primarily provided by the ambient gas pressure. Understanding the nature of such pressure confinement and the related velocity structures is key to understanding the formation of the droplets. It is also crucial to understanding the potential role the droplets, as well as the coherent structures, play in star/structure formation in nearby molecular clouds.

4.1.1. Comparison to the Bonnor–Ebert Sphere

The droplets are likely confined by the pressure exerted on the surface by the ambient gas (Section 3.3), and the subsonic velocity dispersion in the droplets indicates that the internal kinetic energy is largely provided by the thermal motions (Section 3.2). The interior of each droplet has a virtually uniform distribution of the velocity dispersion dominated by the thermal motions, with the nonthermal component being roughly half of the thermal component (see Figures 8 and 9). These results prompt us to compare the droplets to the Bonnor–Ebert model, which describes an isothermal core embedded in a pressurized medium (Ebert 1955; Bonnor 1956; Spitzer 1968).

Using an approach similar to that described in Section 3.2, we derive the radial profiles of volume density, assuming a spherical geometry (see also Appendix E and Figure 27). In the analysis below, we repeat the procedure for layers of regions at different distances, in order to obtain the radial density profile. We use one-half of the GBT beam FWHM as the bin size in the radial direction. The resulting radial density profiles are shown in Figure 12. The typical uncertainty in the density measurement due to the assumption of spherical geometry is ~25%, estimated based on the variation in column density at pixels within each radial distance bin.

We then compare the resulting density profiles of the droplets to the density profile of a Bonnor–Ebert sphere (Figure 12). A Bonnor–Ebert sphere describes an isothermal sphere of gas in a pressurized medium. Assuming a pressure distribution satisfying the ideal gas law, $P = \rho c_s^2$, a Bonnor–Ebert sphere satisfies the Lane–Emden equation:

$$\frac{1}{r^2}\frac{d}{dr}\left(\frac{r^2}{\rho}\frac{d\rho}{dr}\right) = -\frac{4\pi G}{c_s^2}\rho, \quad (7)$$

where r, ρ, and P are the radial distance from the center, the density as a function of the radius, and the pressure at r, respectively (Ebert 1955; Bonnor 1956). A set of nonsingular numerical solutions can be found for Equation (7). Following analyses presented by Ebert (1955), Bonnor (1956), and Spitzer (1968), we compare the observed density profiles with the density profile of a critical Bonnor–Ebert sphere in the normalized and dimensionless units of the density, $y = \rho/\rho_{cen}$, where ρ_{cen} is the density at the center ($r = 0$), and of the distance, $x = r/r_c$, where $r_c = c_s/\sqrt{4\pi G\rho_{cen}}$, corresponding to the y-axis and the x-axis of Figure 12, respectively. Note that x is proportional to the freefall length scale, $r_{ff} \simeq 1.92 r_c$.

Figure 12(a) shows the result of the comparison, with the observed density profiles shown as curves color coded by the ratio between Ω_G and Ω_K, and the density profile of the critical Bonnor–Ebert sphere plotted as the thick black line. The resulting Bonnor–Ebert sphere has a critical minimum radius for which the sphere is stable, $x_{crit} = 6.5$, corresponding to a critical density contrast of $y_{crit} = 1/14.1$ (the horizontal dashed line in Figure 12(a); see discussions in Bonnor (1956) and Ebert (1955) for details). In a *critical* Bonnor–Ebert sphere, the kinetic support and self-gravity is at a critical equilibrium, and the noncritical, stable solutions form a set of density profiles shallower than the critical Bonnor–Ebert sphere. In this model, a core with a density profile steeper than that of the critical Bonnor–Ebert sphere would collapse under self-gravity.

Figure 12(a) shows that the density profiles at $r \lesssim r_{ff}$ appear to be near-constant, while the density profiles at $r \gtrsim r_{ff}$ appear to be shallower than the critical Bonnor–Ebert sphere. On the outer edge, the density profiles of the droplets approach $\rho \propto r^{-1}$, which can arise from structures having a constant column density and thus following a mass–size relation of $M \propto R^2$. This mass–size relation has been observed for cloud-scale structures (see examples in Larson (1981) and discussions in Kauffmann et al. (2010a, 2010b)). The noncritical, shallow density profiles can be consistent with the virial analysis presented in Section 3.3, where the droplets are found to be bound by ambient pressure but not self-gravity. For reference, we also compare the radial density profiles of the droplets to previously observed starless cores (Tafalla et al. 2004), and we find that the droplets have shallower density profiles than starless cores (Figure 12(b); see also Appendix G for the radial profiles in physical units).

Because the Bonnor–Ebert sphere describes a thermal (no turbulent motions) and isothermal (uniform temperature) sphere, the radial profile of the gas pressure, derived from the ideal gas law, $P = \rho c_s^2$, in the Bonnor–Ebert model, is the same as the density profile of a Bonnor–Ebert sphere in dimensionless units. In Figure 13(a), we compare the observed radial profiles of the gas pressure (due to the turbulent and thermal motions of the gas) in droplets to the pressure profile of a critical Bonnor–Ebert sphere. Intriguingly, L1688-d2, L1688-d5, and L1688-d6 have pressure profiles increasing *outward*, and these droplets also appear to be less gravitationally bound (redder curves in Figure 13). However, note that L1688-d2 and

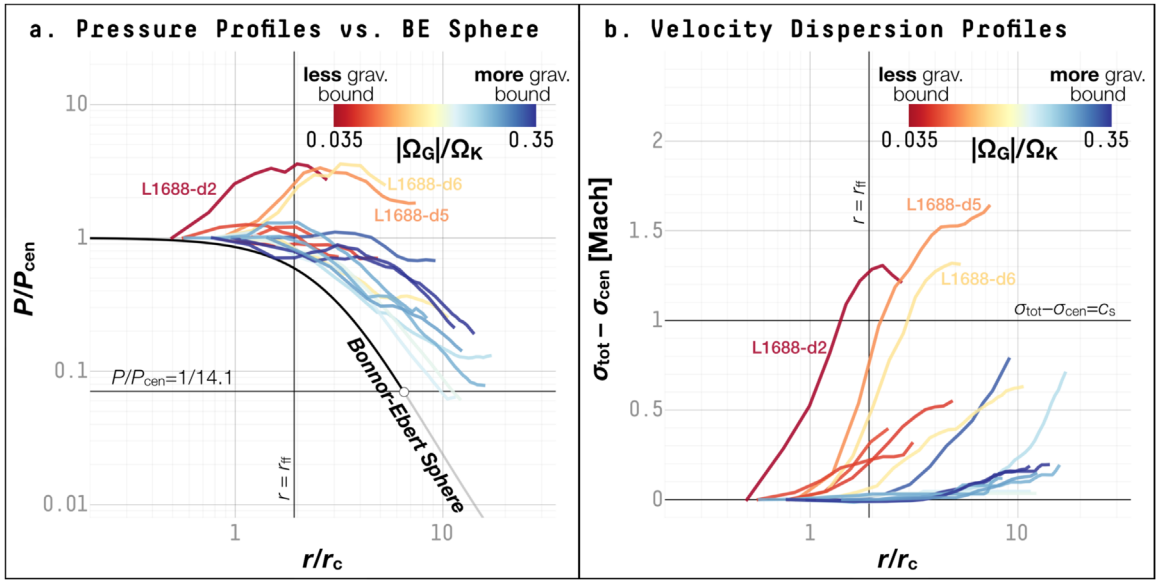

Figure 13. (a) Like Figure 12(a), but for the radial profile of pressure in normalized units of each droplet. Because L1688-d2 and L1688-d5 sit near the edge of the regions with significant detection of NH_3 (1, 1) emission, the profiles at larger radii could be dominated by fewer pixels, and thus the corresponding curves are specifically marked. L1688-d6 is also marked due to its highly elongated shape, for which the measurements using equidistant annuli could be biased. (b) The radial profile of total velocity dispersion, $\sigma_{\rm tot}$, relative to the value at the center of the droplet, $\sigma_{\rm tot,cen}$, in Mach numbers (ratios to the sonic velocity). The horizontal line marks when the change in $\sigma_{\rm tot}$ with respect to $\sigma_{\rm tot,cen}$ is equal to the sonic speed. Because the dumbbell shape of L1688-d1 affects this analysis, which assumes spherical geometry, L1688-d1 is not included in these plots.

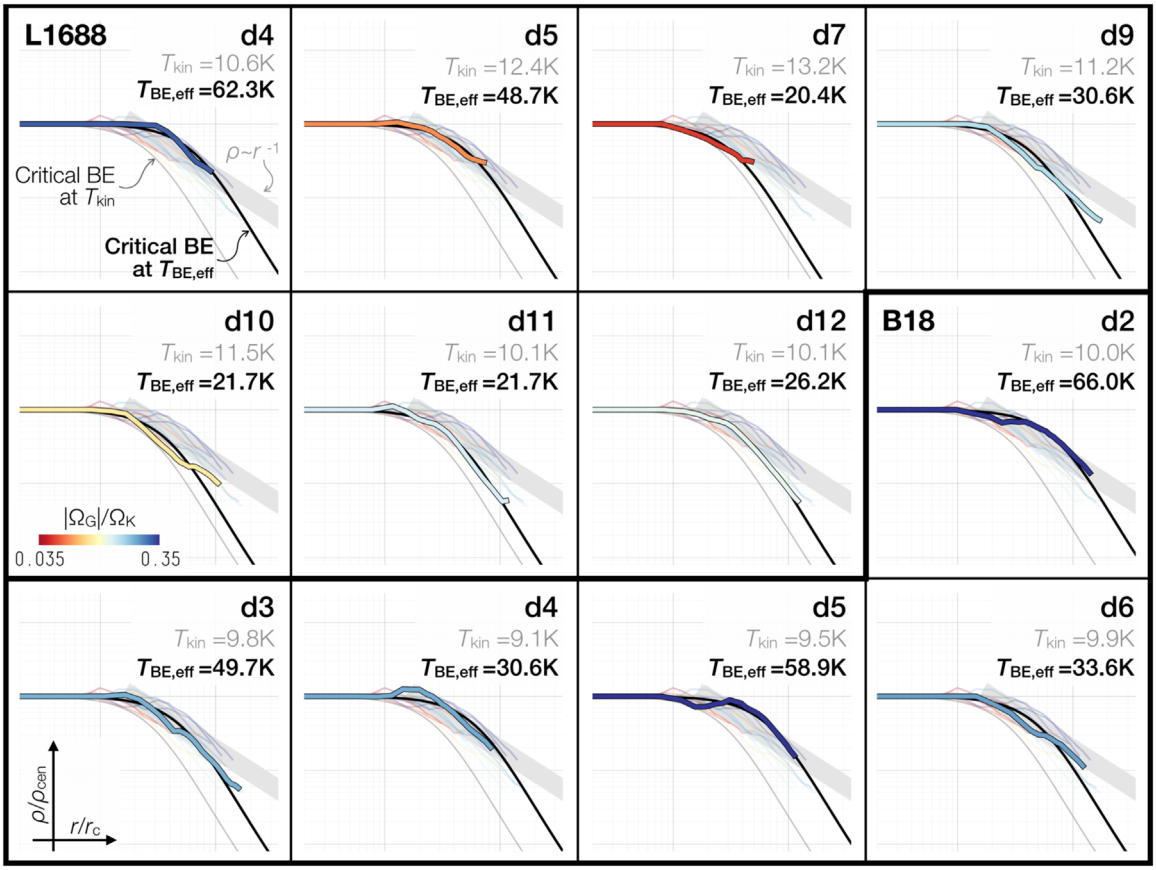

Figure 14. Individual radial profiles of normalized volume density, compared to critical Bonnor–Ebert spheres at best-fit effective temperatures. Each panel shows the radial density profile of a droplet, with the ID labeled at the top right of the panel. The observed radial density profile in each panel is plotted as thick curves, color coded according to $\Omega_{\rm G}/\Omega_{\rm K}$. The radial density profile of a Bonnor–Ebert sphere at the best-fit effective temperature are shown as black curves (see surrounding text for details). The radial density profile of a Bonnor–Ebert sphere at the observed $T_{\rm kin}$, corresponding to the radial density profile of the critical Bonnor–Ebert sphere shown in Figure 12, is plotted as a light gray curve in each panel. The gray band corresponds to a power-law density profile, $\rho \propto r^{-1}$. Density profiles of droplets other than the one highlighted in each panel are plotted as transparent curves.

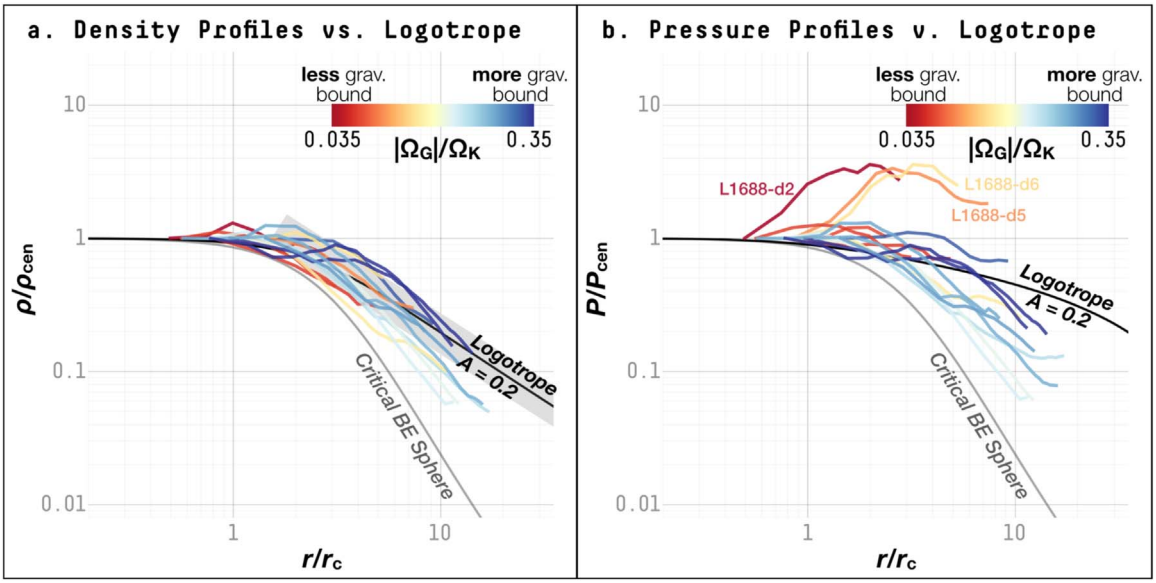

Figure 15. (a) Radial profile of volume density in normalized units of each droplet, compared to a logotropic density profile. Each curve is the radial profile of a droplet, color coded according to Ω_G/Ω_K. The thick black curve plots the density profile of a logotropic sphere, and the gray curve shows the density profiles of a critical Bonnor–Ebert sphere. The light gray band shows the slope of the power-law density profile, $\rho \propto r^{-1}$. The typical uncertainty for each volume density measurement along a density profile is ∼25%. (b) The radial profile of pressure in normalized units of each droplet, same as the color-coded curves shown in Figure 13(a). The black curve plots the radial profile of normalized pressure for a logotropic sphere, and the gray curve plots the radial pressure profiles of the critical Bonnor–Ebert sphere. As in Figure 13, L1688-d2, L1688-d5, and L1688-d6 are marked either because the droplet sits near the edge of the regions with significant detection of NH_3 (1, 1) emission or because of the highly elongated shape.

L1688-d5 sit near the edge of the region where NH_3 emission is detected, such that the profiles at larger radii are dominated by fewer pixels. Note also that the assumption of spherical geometry could break down due to the elongated shape of L1688-d6. Figure 13(b) shows that the increases in velocity dispersion across the edges of the droplets are usually more abrupt than the change in the density profiles (Figure 12). See Appendix G for the radial profiles of density and pressure in physical units.

Using a free parameter—the "effective temperature," $T_{\rm BE,eff}$—instead of the observed kinetic temperature, $T_{\rm kin}$, to derive c_s in the ideal gas law, we can fit the critical Bonnor–Ebert profile to the observed density profiles of the droplets. Figure 14 shows the resulting critical Bonnor–Ebert spheres at best-fit effective temperatures for droplets where we have reliable measurements of radial density profiles beyond the characteristic size scale. As Figure 14 shows, most of the droplets have an excess in density compared to the best-fit critical Bonnor–Ebert profile at larger distances, approaching a power-law like density profile. For most droplets, the best-fit effective temperature, $T_{\rm BE,eff}$, is unreasonably higher than the kinetic temperature measured from NH_3 line fitting. Again, the results suggest that density and pressure profiles of the droplets cannot be modeled well with a critical Bonnor–Ebert sphere.

4.1.2. Comparison to the Logotropic Sphere

Based on the observational results obtained in the 1990s that (1) the density distribution at large radial distances from the center of a core is close to a power-law expression, $\rho \propto r^{-1}$ (instead of the singular isothermal solution, $\rho \propto r^{-2}$; Shu (1977)), (2) the core is supported by both thermal and nonthermal (turbulent) velocity distributions, and (3) the total velocity dispersion is close to being purely thermal at the center and increases outward, McLaughlin & Pudritz (1996, 1997) proposed that a dense core has a velocity dispersion distribution with a constant (isothermal) thermal component and a purely logotropic nonthermal component, i.e., $P_{\rm T} \propto \rho$ and $P_{\rm NT} \propto \ln \rho/\rho_{\rm cen}$ in terms of pressure distribution, respectively. The resulting solution, known as the logotropic sphere, has an equation of state

$$P = \rho_{\rm cen} c_s^2 \left[1 + A \ln\left(\frac{\rho}{\rho_{\rm cen}}\right)\right], \tag{8}$$

where $A > 0$ is an adjustable parameter of the logotropic component. Replacing the pressure term, derived from the ideal gas law, in the Bonnor–Ebert model with Equation (8), we can find a nonsingular numerical solution of pressure distribution for the logotropic sphere.

Following the analysis presented by McLaughlin & Pudritz (1996, 1997) and similar to the comparison with the Bonnor–Ebert model, we compare the observed radial profiles of density and pressure to a logotropic sphere with $A = 0.2$ (Equation (8), also used by McLaughlin & Pudritz (1996)) in dimensionless units (Figure 15). While Figure 15(a) shows that a logotropic sphere has a density profile generally matching the droplet density profiles, the observed pressure profiles of the droplets decrease faster at increasing distances than the pressure profile of a logotropic sphere (see Figure 15(b)). The result suggests that the logotropic solution cannot describe the droplets, either.

In summary, we find that neither a critical Bonnor–Ebert sphere or a logotropic sphere describes the density and pressure profiles of the droplets well. Instead, the shallow radial density and pressure profiles of the droplets can be approximated by a uniform density at smaller radii and a power-law density distribution approaching $\rho \propto r^{-1}$ at larger radii, the latter of which has also been observed for cloud-scale structures.

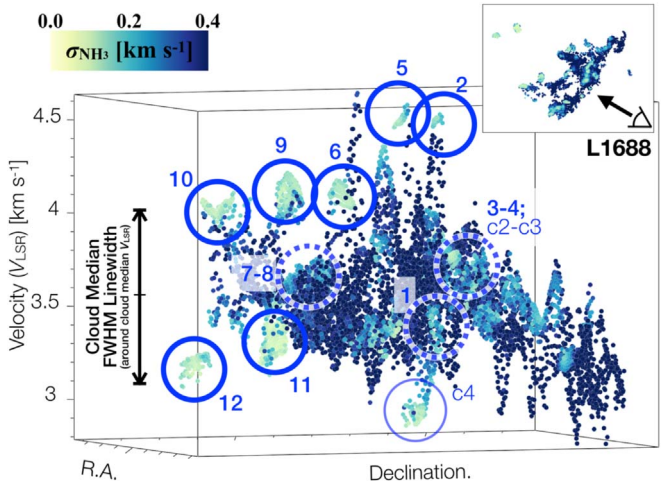

Figure 16. PPV distribution of the best Gaussian fits to the NH_3 hyperfine line profiles, color-coded by the NH_3 velocity dispersion, σ_{NH_3}. Each dot corresponds to a pixel in the plane of the sky. The map at the top right corner shows the projected point of view on the plane of the sky. The droplets that are distinguishable in PPV space from the distribution of the bulk material in the cloud (as traced by NH_3 hyperfine line emission; usually the darker points) are marked by solid circles, while the approximate positions of the droplets that are more embedded in the cloud in PPV space are marked by dashed circles. The numbers correspond to the droplet IDs in Table 1, with the header "L1688-" removed for better visualization. The visualization is made with the aid of Glue.

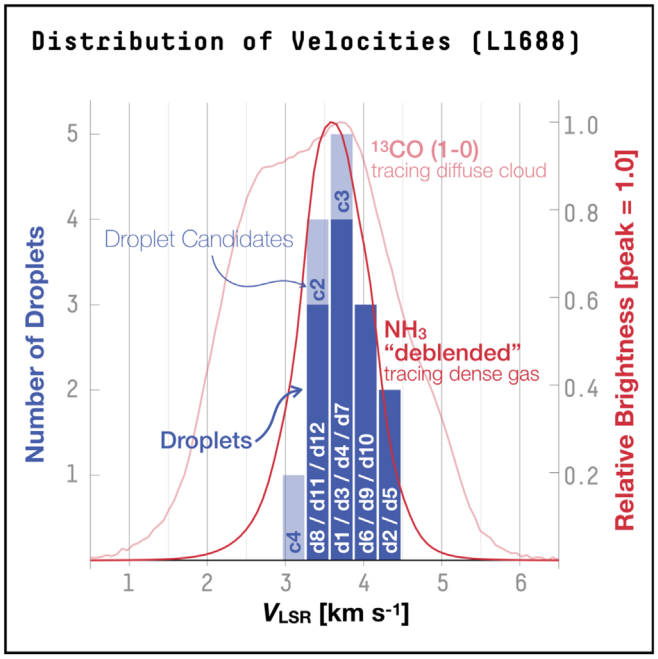

Figure 17. Distribution of velocity centroids of the droplets and droplet candidates (blue histogram; lighter parts correspond to droplet candidates), plotted against the average spectra of NH_3 (dark red curve) and ^{13}CO (1–0) emission (light red curve). The NH_3 average spectrum is calculated from a "deblended" data cube created based on the results of NH_3 line fitting, such that each spectrum is a Gaussian with a center the same as the velocity centroid and a spread (σ) the same as the velocity dispersion. The structure IDs of the structures included in each bin of the histogram are noted, with the leading "L1688-" removed for better visualization. The spectra are shown in relative units wherein the peak has a value of 1.

4.1.3. Velocity Distribution of the Droplet Ensemble

The virial analysis presented in Section 3.3 suggests that the confinement of the droplets is primarily provided by the ambient gas pressure. Consistently, we find that the droplets have noncritical and relatively shallow density profiles approaching $\rho \propto r^{-1}$ at the outer edges. Both results point to a close relation between the droplets and the local cloud environment. Below, to investigate this relationship between the droplets and the surrounding cloud, we examine the distribution of emission in the position–position–velocity (PPV) space.

Figure 16 shows the PPV distribution of the best fits to the NH_3 hyperfine line profiles observed at the pixels shown in Figure 2(b), with the locations along the velocity axis equal to the velocity centroids of the best fits. With each data point (the location of the Gaussian peak) color-coded by σ_{NH_3}, several features with low line widths stand out as having line-of-sight velocities that differ from the system velocity of the cloud by $\sim$0.5 km s^{-1}. Overall, we find that roughly half of the total 12 droplets in L1688 sit at the local extremes in V_{LSR}, while the other half appear more embedded in the main cloud component in the PPV space. Note that the distribution of emission in the PPV space does not correspond to the distribution of material in the position–position–position space (Beaumont et al. 2013), and the deviation in V_{LSR} from the main cloud component does not necessarily suggest that the droplet is separated from the cloud in the position–position–position space.

Notably, the typical V_{LSR} difference of $\sim$0.5 km s^{-1} between the V_{LSR} of droplets found at local velocity extremes and the system velocity of the cloud component traced by the NH_3 emission is comparable to half of the median FWHM line width of the NH_3 (1, 1) emission, $\sim$0.46 km s^{-1} (shown as a vertical line along the velocity axis in Figure 16; $FWHM_{NH_3} \approx 0.92$ km s^{-1}, measured for pixels outside the droplet boundaries—dark blue regions in Figure 2(b)). A more detailed comparison shows that the dispersion in the velocity centroids of the droplets (analogous to the "core-to-core velocity" examined by Kirk et al. (2010)) agrees well with the median NH_3 velocity dispersion measured at pixels outside the droplet boundaries (see Table 4). In Figure 17, we compare the distribution of droplet V_{LSR} to the average "deblended" spectrum of the entire L1688 region,[26] and show that the distribution of droplet V_{LSR} has a shape similar to the deblended NH_3 line profile. Given that the NH_3 velocity dispersion, σ_{NH_3}, is associated with the thermal and turbulent motions of the dense gas, the results suggest that the droplets

Table 4
Velocity Distribution of the Droplets and the Entire Cloud in the L1688 Region

	Median Velocity	Velocity Dispersion
Entire Cloud[a]	$3.54^{+0.23}_{-0.22}$	$0.39^{+0.16}_{-0.14}$
Droplets[b]	$3.68^{+0.42}_{-0.23}$	0.39[c]

Notes.
[a] Measured from pixel-by-pixel distributions on the maps of V_{LSR} and σ_{NH_3}, excluding pixels within the droplet boundaries.
[b] Measured from the droplet samples, as listed in Table 1.
[c] Measured by taking the standard deviation of the V_{LSR} distribution (see Table 1); the velocity resolution of the observations is $\sim$0.07 km s^{-1}.

[26] Friesen et al. (2017) constructed "deblended" spectral cubes from the results of the NH_3 hyperfine line fitting, assuming a single Gaussian line profile with the mean and the dispersion equal to V_{LSR} and σ_{NH_3} from the best fit for each pixel. The deblending removes the NH_3 hyperfine line components and allows direct comparison with other spectra and velocity distributions.

Table 5
Comparison between the Droplets and the Structure Found in the MHD Simulation

	Mass ($M_\odot$)	Effective Radius (pc)	$\sigma_{\rm tot}$ (km s^{-1})	Difference in LOS Velocity from the Cloud (km s^{-1})
Droplets (Observation)[a]	$0.4^{+0.4}_{-0.3}$	0.04 ± 0.01	0.22 ± 0.02	$0.39/\sim 0.5$[b]
Droplets (MHD Simulation)[c]	0.2 ± 0.1	0.04 ± 0.01	0.24 ± 0.02	0.37
Sim-d1 (MHD Simulation)[c]	0.96	0.036	0.24	0.63
Sim-c1 (MHD Simulation)[d]	0.44	0.031	0.23	0.14

Notes.
[a] Median values with the lower and the upper bounds correspond to the 16th and 84th percentiles, respectively.
[b] The standard deviation of the droplet $V_{\rm LSR}$ distribution is 0.39 km s^{-1} (see Table 4). For droplets that sit at local velocity extremes, the typical $V_{\rm LSR}$ difference is $\sim$0.5 km s^{-1}.
[c] The droplets in the MHD simulation, including Sim-d1, are identified in the synthesized NH_3 spectral cube following the same procedure described in Section 3.1; see our Figure 18 and Section 4.2, as well as R.A. Smullen et al. (2019, in preparation)
[d] Sim-c1 is found to associate with a shock-induced structure not unlike the one associated with Sim-d1. While Sim-c1 also has a subsonic velocity dispersion, it is less clear whether a transition to coherence happens at its periphery (see Figure 18). Thus, it is categorized as a "droplet candidate."

are traveling in the dense component of the cloud at velocities on par with the thermal and turbulent motions of the dense gas traced by NH_3 emission. The results further suggest that the velocities of the droplets are inherited from the velocity dispersion of materials in the environment.

For reference, we also compare the distribution of droplet $V_{\rm LSR}$ to the average ^{13}CO (1–0) spectrum[27] and find that ^{13}CO (1–0) has a line profile 2–3 times broader than the droplet-to-droplet velocity distribution. The result is consistent with what Kirk et al. (2010) observed in Perseus. Using the N_2H^+ emission to trace the dense core motions in the molecular cloud, Kirk et al. (2010) found that the core-to-core velocity dispersion is about half of the total ^{13}CO velocity dispersion in the region.

In the analyses presented in Sections 3.3 and 4.1, we find that: (1) the droplets generally appear to be predominantly confined by the ambient gas pressure and not bound by self-gravity, and that (2) there is a close relation between the droplets and the local cloud component traced by the NH_3 emission. Together, the results point to the possibility that the droplets, primarily defined by their subsonic and uniform interiors, are the result of compression due to the relatively more turbulent motions in the dense gas component of the cloud. in Section 4.2, we look for similar structures in a MHD simulation and speculate on the potential formation mechanism of the droplets.

4.2. Comparison with Hydrodynamic Models

Simple analytical models could hint at the formation mechanism of droplets. For example, by extending the Jeans model (Jeans 1902), Myers (1998) proposed a "kernel" model in which a condensation with a mass of 1 $M_\odot$ and a size of 0.03 pc can exist within a dense core under ambient pressure provided by the thermal and turbulent motions. Below, we demonstrate that formation of droplets is also possible in an MHD simulation of a turbulent cloud with self-gravity and sink particles (representing protostars).

We analyze an MHD simulation of a star-forming turbulent molecular cloud (R. A. Smullen et al. 2019, in preparation). The simulation is carried out with the ORION2 adaptive mesh refinement (AMR) code (Li et al. 2012). The domain represents a piece of a molecular cloud 5 pc on a side with physical parameters and initialization identical to those of the W2T2 simulation in Offner & Arce (2015). The mean gas density is $\rho = 440\,{\rm cm}^{-3}$ ($2.04 \times 10^{-21}\,{\rm g\,cm}^{-3}$). The initial gas temperature is 10 K. The ratio of thermal to magnetic pressure is $\beta = 8\pi c_s^2/B^2 = 0.1$ and becomes 0.02 after two crossing times of driving. The gas has a velocity dispersion of 1.98 km s^{-1}, which is set such that the cloud falls on the observed relation. The calculation has five AMR levels with a maximum resolution of 125 au. We analyze a snapshot at 0.52 Myr or 0.35 $t_{\rm ff}$ as measured from when the initial driving phase ends and self-gravity is turned on. At this time, 1.3% of the gas is in stars.

We use RADMC-3D[28] to calculate the NH_3 emission given the simulated gas density and temperature distribution. We adopt a uniform NH_3 abundance of $2 \times 10^{-9}\,n_{\rm H}$. We adopt the collisional parameters from the Leiden atomic and molecular database (Schöier et al. 2005) and compute the radiative transfer using the nonlocal thermodynamic equilibrium large velocity gradient approximation (Shetty et al. 2011). To look for structures that show (1) a sharp change in velocity dispersion and (2) locally concentrated emission, we derive the moment maps using the synthesized NH_3 spectral cube. We then follow the same identification procedure described in Section 3.1 and identify a total of eight droplets that show clear signs of a change in velocity dispersion and coincide with concentrated synthetic NH_3 emission, as well as another four droplet candidates.

The identified droplets in the MHD simulations have a typical effective radius of 0.04 ± 0.01 pc, a typical mass of $0.2 \pm 0.1\,M_\odot$, and a typical total velocity dispersion of 0.24 ± 0.02 km s^{-1}. The droplets found in the simulation also have a typical difference in $V_{\rm LSR}$ of 0.37 km s^{-1}. These values span a range similar to those found for the droplets identified in the observations within uncertainty (Table 5; see also Figure 19).

Following the virial analysis presented in Section 3.3, we find that, similar to the droplets found in L1688 and B18, the droplets identified in the MHD simulation are generally not bound by self-gravity and are instead confined by the ambient pressure. The ambient pressure of the droplets in the simulation

[27] The ^{13}CO spectrum is from the COMPLETE Survey of the molecular cloud in Ophiuchus (Ridge et al. 2006).

[28] See http://www.ita.uni-heidelberg.de/~dullemond/software/radmc-3d/index.html for documentation.

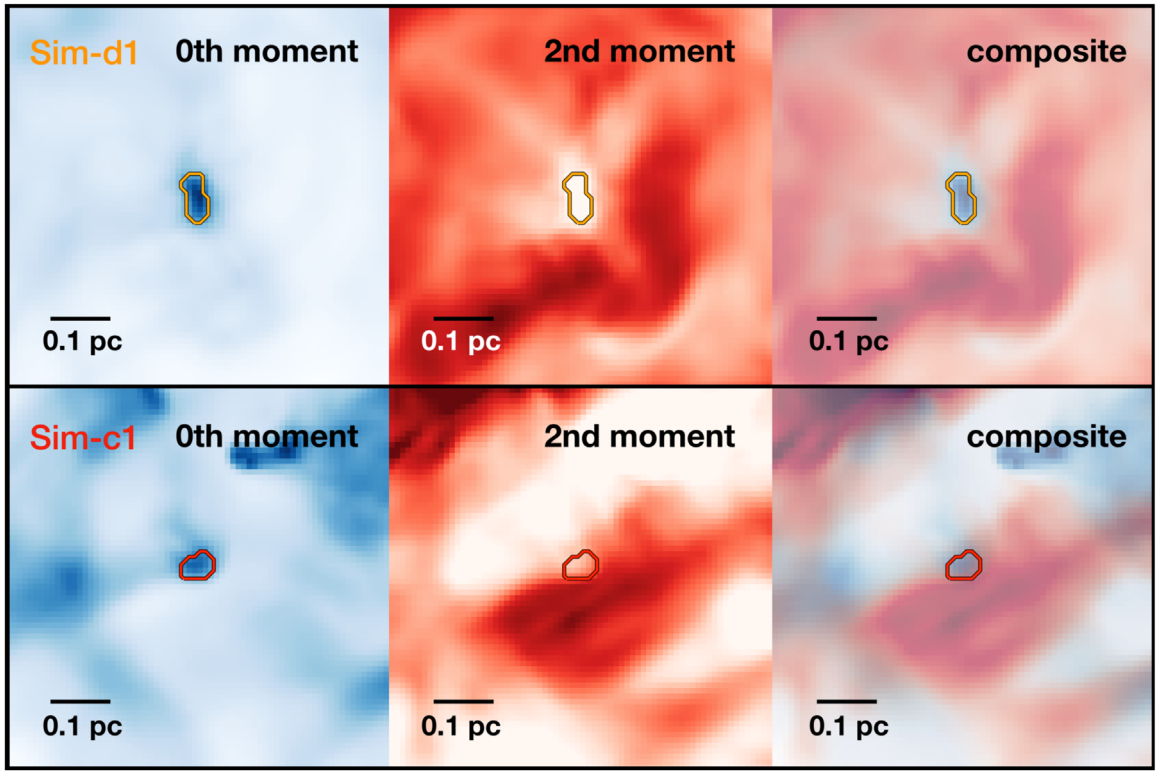

Figure 18. Top row depicts Sim-d1, a droplet identified in the MHD simulation following the procedure described in Section 3.1 (R. A. Smullen et al. 2019, in preparation), with an identifiable rise in integrated emission (zeroth moment; left panel) and a sharp drop in velocity dispersion (second moment; middle panel) near its edge. The rightmost panel shows an overlay of the zeroth and second moment maps. The bottom row is the same as the top, but showing Sim-c1. This is another structure associated with an isolated shock-induced feature that has a subsonic velocity dispersion, but where signs of a transition to coherence are less clear. Note that each panel shows only a 0.7 pc by 0.7 pc region near the dense structures.

is $P_{\rm amb}/k_{\rm B} \approx 1.4^{+1.7}_{-1.0} \times 10^5\,{\rm K\,cm^{-3}}$, comparable to the typical value of $P_{\rm amb}/k_{\rm B} \approx 2.7^{+4.7}_{-1.8} \times 10^5\,{\rm K\,cm^{-3}}$ for the droplets in L1688 and B18.

To gain insight into droplet formation, we select an isolated droplet, Sim-d1, and follow its evolution in the MHD simulation (Figures 18 and 20). We find that Sim-d1 corresponds to a relatively isolated shock-induced feature in the MHD simulation, moving generally toward the viewer along the line of sight on which we "observe" the synthesized NH_3 cube (see Figure 20 and the video showing the evolution of the MHD cube linked in the caption). Meanwhile, material seems to accumulate at the converging point of the shock-induced feature as the simulation evolves. The general movement of Sim-d1 toward the viewer is consistent with the relatively high line-of-sight velocity difference observed in the synthesized NH_3 cube, $\sim$0.63 km s^{-1}. The association between a droplet and a shock-induced feature, viewed from different angles, might explain why the observed droplets are sometimes found at local line-of-sight velocity extremes.

A significant portion of droplets and droplet candidates identified in the simulation are found to be associated with similar shock-induced features (e.g., Sim-c1, marked by the red square in Figure 20). These structures generally have subsonic internal velocity dispersions, but do not necessarily satisfy all criteria used for identification in Section 3.1. The droplet candidate Sim-c1 (Figure 18) is a typical example. We find that Sim-c1 has properties consistent with the physical properties of the droplets identified in observations (see Figure 19 and Table 5).

Notably, the most active star-forming regions are found near points where shocks are colliding and gas is converging. This creates local density enhancements, which are conducive to core formation if matter continues to accumulate (see Figure 20). It seems possible that the droplet-like features associated with isolated shock features might evolve into star-forming cores through continuing accumulation of material and/or through converging with other shock-induced features. See more discussion below in Section 4.3.

4.3. Cores and Droplets

In this work, we examine the physical properties of two closely related populations of structures: the droplets and the dense cores (among which many were found to be coherent cores). In the analyses presented above, we essentially use the terms "droplets" and "dense cores" to indicate structures identified in this work and those examined by Goodman et al. (1993), respectively. Although the two populations indeed have different physical properties, we are not satisfied with this rather arbitrary use of terminology. Thus, in what follows, we provide a more physical set of definitions for different groups of structures discussed in this paper.

We define droplets to be gravitationally unbound and pressure-confined coherent structures, wherein the coherent structures include any structures that have subsonic velocity dispersions and show transitions to coherence. In comparison, a *coherent core* is a gravitationally bound coherent structure, and a *dense core* is a centrally concentrated density feature with a velocity dispersion approaching a transonic or subsonic value

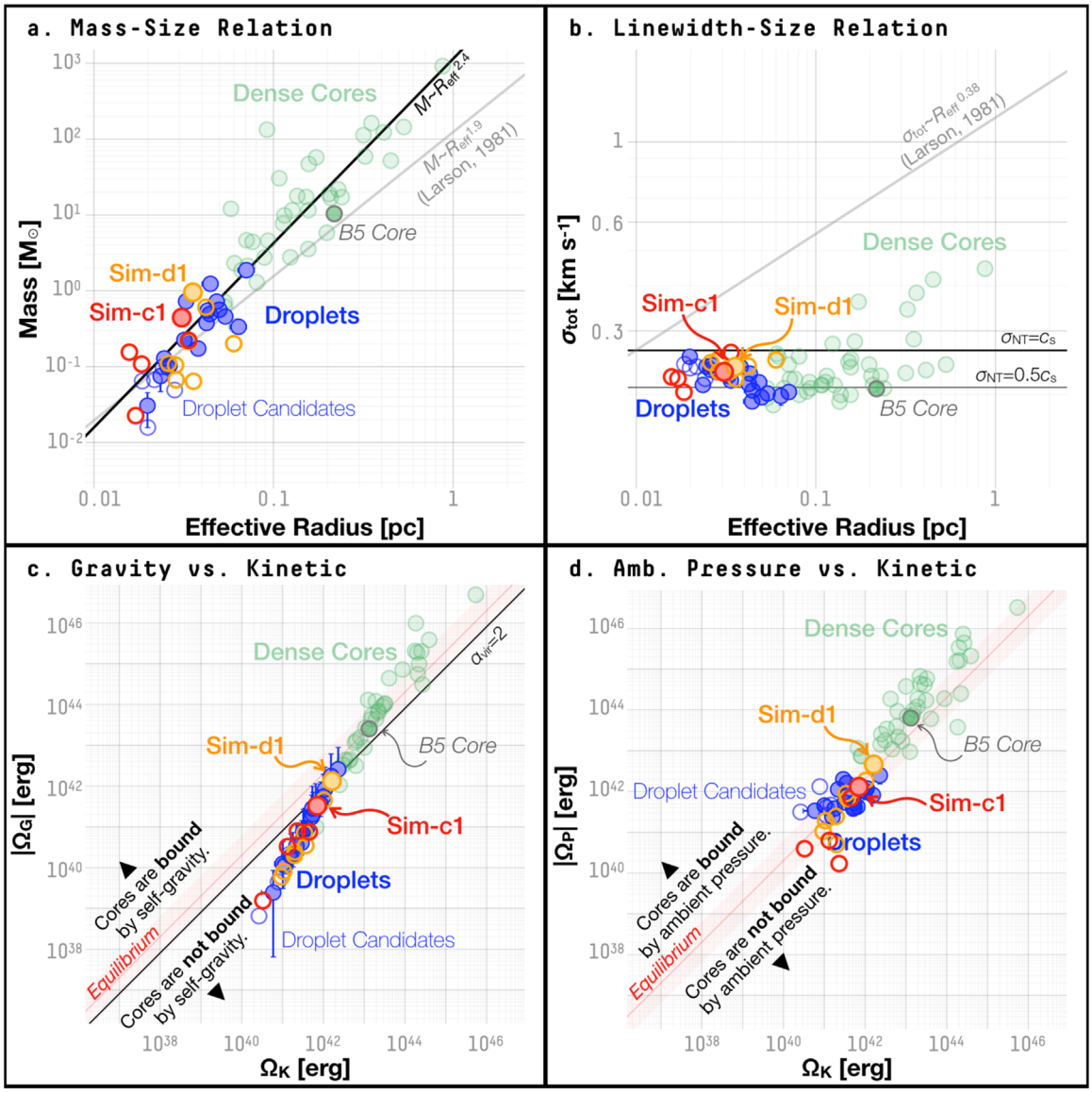

Figure 19. Same as Figures 9 and 10, but for droplets (yellow circles) and droplet candidates (red circles) in the MHD simulation. Sim-d1 and Sim-c1 (shown in Figure 18) are plotted as a filled yellow circle and a filled red circle, respectively, against the dense cores (green circles) and the droplets (blue circles). (a) The mass–size distribution (see Figure 9(a)). (b) The $\sigma_{\rm tot}$-size distribution (see Figure 9(b)). (c) Gravitational potential energy, $\Omega_{\rm G}$, plotted against internal kinetic energy, $\Omega_{\rm K}$ (see Figure 10(a)). (d) The energy term representing the confinement provided by the ambient gas pressure, $\Omega_{\rm P}$, plotted against the internal kinetic energy, $\Omega_{\rm K}$ (see Figure 10(b)).

(not necessarily showing a transition to coherence). Just like a coherent core may correspond to the densest region of a dense core, a droplet may be the innermost region of a larger structure. The definitions are summarized in Table 6.

Due to the lack of observations needed to determine whether the cores examined by Goodman et al. (1993) show any signs of a transition to coherence, we simplify the criteria and recategorize the structures identified in this work and those examined by Goodman et al. (1993) into two categories: (1) "droplets," structures not virially bound by self-gravity and with subsonic velocity dispersions; and (2) "dense cores," structures virially bound by self-gravity and with subsonic velocity dispersions. In the discussion below, we retain the quotation marks around these terms to differentiate them from the terms used throughout the analyses above.

Figure 21 shows how this recategorization would change the groupings of structures examined in the analyses in this paper. To proceed with caution and avoid uncertainty in using a virial analysis to determine the equilibrium state of a structure, we categorize those structures with subsonic velocity dispersions and within an order of magnitude of a virial equilibrium between the gravitational potential energy and the kinetic energy (see details in Section 3.3) as "dense core candidates." Notice in Figure 21 that most of these "dense core candidates" have virial parameters $\leqslant$2 and would conventionally be considered virially bound by self-gravity. In this recategorization, we temporarily omit structures with supersonic velocity dispersions, although the largest turbulent Mach number (the ratio between the turbulent component of velocity dispersion and the sonic speed) found in these structures is $\lesssim$1.5, i.e., nowhere close to the turbulence measured for the entire molecular cloud. For example, using observations of the ^{13}CO (1–0) emission, we measure a turbulent Mach number of $\sim$10 for Ophiuchus. In total, three out of 43 dense cores are

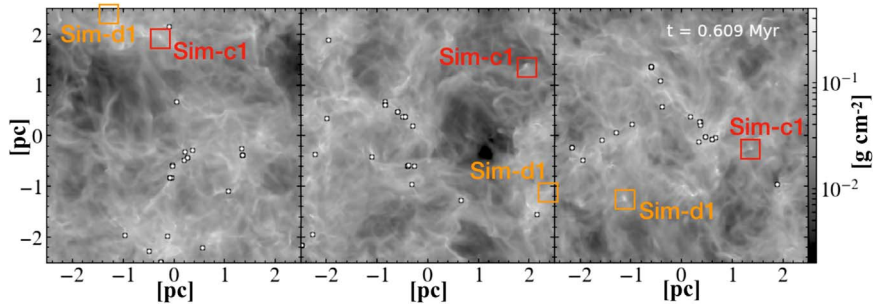

Figure 20. Integrated density along three different viewing directions of the MHD simulation examined in Section 4.2. The rightmost panel shows how the view adopted for the synthesized NH_3 cube is derived and used to calculate the moment maps shown in Figure 18. The yellow square marks the droplet-like structure identified following the same procedure described in Section 3.1 and shown in Figure 18. The red square marks another shock-induced feature, around which signatures of a subsonic velocity dispersion and a concentrated density distribution are found. The white dots mark the positions of the sink particles. In a 40 s animated version of this plot (available in the HTML version of this article), we show the evolution of the simulated density cube in the same integrated density units (g cm^{-2}) from 1.46×10^5 yr to 6.09×10^5 yr in the evolutionary time. In the animation, multiple filamentary structures as well as more isolated shock-induced features are found moving across the star-forming medium. The static version shown here corresponds to the last frame of the animation at 6.09×10^5 yr in the evolutionary time, at which time step we identified Sim-d1 and Sim-c1 using synthetic observations of NH_3 emission. We use a monotonic color map in the static version to better show the integrated density in contrast to the orange and red boxes used to mark the identified structures. The animation is also available at https://goo.gl/PEd9Pd.

(An animation of this figure is available.)

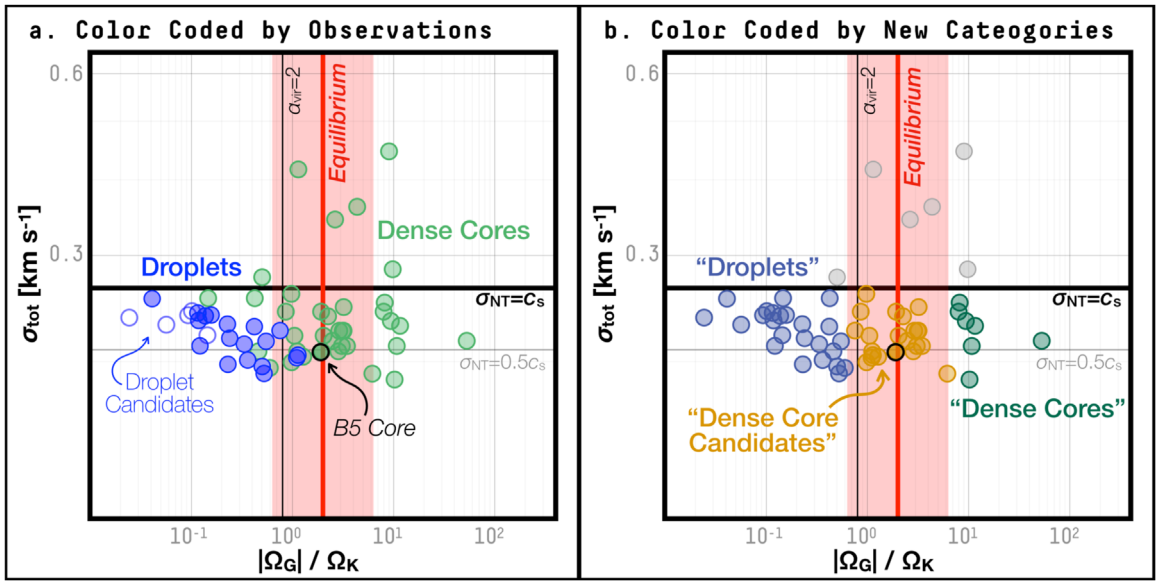

Figure 21. (a) Total velocity dispersion, σ_{tot}, plotted against the ratio between Ω_G and Ω_K. The droplets and droplet candidates are plotted as solid and empty blue circles, and the dense cores are plotted as green circles. The horizontal lines show the total velocity dispersions expected for structures where the nonthermal component is equal to the sonic speed (thicker, black line) and half the sonic speed (thinner, gray line) of a medium with a mean molecular weight of 2.37 u at a temperature of 10 K. The vertical red band marks an equilibrium between Ω_G and Ω_K (solid red line) within an order of magnitude (pink band). The vertical black line marks $\alpha_{vir} = 2$. (b) Same as (a), but with the data points color coded according to the proposed recategorization of structures into "dense cores" (dark green circles), "dense core candidates" (dark yellow circles), and "droplets" (dark blue circles; see Section 4.3). Structures that have supersonic velocity dispersions are omitted in this recategorization and plotted as gray circles.

recategorized as "droplets," and three out of 18 droplets are recategorized as "dense core candidates."

Figure 22 shows the distributions of the recategorized structures in various parameter spaces. It is evident that different populations (i.e., "droplets" and "dense cores") categorized according to their physical properties are mingled and form a continuous distribution. This continuity might suggest that different populations of coherent structures emerge from the same set of physical processes, although they differ in gravitational boundedness. Based on the MHD simulation examined in Section 4.2, one possible scenario is that both the gravitationally bound coherent structures (coherent cores) and the gravitationally unbound and pressure-confined coherent structures (droplets) arise from shock-induced overdensities. In this scenario, we would likely find star-forming coherent cores at the converging points of multiple shocks, and we would find droplets around more isolated shock-induced structures and/or isolated pairs of colliding shocks.

Based on an examination of the MHD simulation (Section 4.2), a shock-induced formation mechanism of coherent structures might point to an evolutionary sequence connecting droplets and coherent cores. If droplets are formed as isolated shock-induced structures, they might still evolve into star-forming and gravity-dominated coherent cores in the future, if the isolated shocks converge/collide with other shock-induced structures. Similarly, based on observations of

Table 6
Cores and Droplets[a]

	Therm. Dominated Line Widths[b]	Transition to Coherence[c]	Assoc. with YSOs	Gravitationally Bound	Pressure Bound
Droplets	Yes	Yes	Neutral	No	Yes
Dense Core[d]	Yes	Neutral	Neutral	(Yes)	Neutral
Coherent Core[e]	Yes	Yes	Neutral	Yes	Neutral
Starless Cores[f]	Neutral	Neutral	No	No	Neutral
Prestellar Cores[f]	Neutral	Neutral	No	Yes	Neutral
Protostellar Cores[g]	Neutral	Neutral	Yes	Yes	Neutral

Notes.
[a] This table lists the definitions of names commonly given to subsets of cores, as logical combinations of several criteria. A value of "Yes" means that a core needs to meet the criterion in order to be assigned to a certain category. A value of "No" means that a core needs to satisfy the *negation* of the criterion. A value of "Neutral" means that the definition of a certain category does not concern the criterion.
[b] The thermal component of the velocity dispersion is larger than the nonthermal (turbulent) component.
[c] Observation of "transition to coherence," as described by Goodman et al. (1998). The observation of "transition to coherence" may be done by observing the same core with multiple tracers and focusing on the change in the line width–size relation going from one tracer to the next (Type 4 in Figure 9 of Goodman et al. (1998), later used by Caselli et al. (2002) in observations of coherent cores). Another way to observe the "transition to coherence" is to spatially resolve the transition with a single tracer. Examples include observations of NH_3 emission in B5 (Pineda et al. 2010) and the droplets in this work. Note that the criterion of "transition to coherence" is stricter than "thermally dominated line widths." The thermally dominated line widths concern the overall measurement of velocity dispersion in the core but not the spatial change in velocity dispersion.
[d] The canonical example of dense cores (e.g., Myers et al. 1983) is simply defined by a centrally concentrated density distribution. Based on observations of NH_3 emission and emission from other higher-density molecular line tracers, Myers (1983) found that most of the dense cores examined by Myers et al. (1983) had velocity dispersions approaching transonic or subsonic values. Gravitational boundedness was less clear, oftentimes because of a lack of observations necessary to accurately estimate the boundedness of these structures. The dense cores analyzed by Goodman et al. (1993) and included in this paper are mostly gravitationally bound, as shown in Figure 10.
[e] As described by Goodman et al. (1998) and later observed by Caselli et al. (2002) and Pineda et al. (2010).
[f] In the literature, neither the starless cores nor the prestellar cores are associated with any YSOs. A criterion often used to distinguish between the two categories is gravitational boundedness. Prestellar cores are cores that are gravitationally bound, and starless cores are those that are not (e.g., Tafalla et al. 2004). In some cases, density features at smaller scales within the cores are used to further investigate the "starlessness" of the starless cores (e.g., Kirk et al. 2017a).
[g] By definition, protostellar cores are cores associated with YSOs.

core structures in the B218 region in Taurus, Seo et al. (2015) show that it is more likely to find Class 0/I YSOs associated with gravitationally bound cores than with pressure-confined structures. Thus, Seo et al. (2015) suggest that there exists an evolutionary sequence connecting the pressure-confined structures to the gravitationally bound cores. The evolutionary sequence suggested by Seo et al. (2015) might conform with the conventional evolutionary sequence observed toward the prestellar and the protostellar cores (see Table 6).

Because droplets are found within active star-forming regions, the projection effect makes it difficult to determine whether or not the droplets are associated with any YSOs. If we simply look at the existence of YSO(s) within the droplet boundary projected on the plane of the sky, we find that five out of twelve droplets in L1688 and one out of six droplets in B18 coincide with at least one YSO within each of their boundaries. This gives a $\lesssim$40% chance of finding at least one YSO within the droplet boundary. As described in Section 3.1, we do not find significant rises in $T_{\rm kin}$ in any of the droplets where we find YSOs, and as shown above in Section 3 and in Figure 23, we do not find a statistically significant difference in physical properties between the droplets with YSOs within their boundaries and those without. Compared to the coherent core in B5, where a YSO and at least three star-forming substructures are found, we do not find signs of star-forming substructures in the droplets with YSOs within their boundaries (see Section 3.3 and Pineda et al. 2015). These facts indicate that the innermost part not resolved by our observations may be gravitationally bound in these droplets, and if this is proved true, it is likely that there exists an evolutionary sequence connecting the pressure-confined droplets to the star-forming gravitationally bound coherent cores (such as the one in B5; see also discussions in Seo et al. (2015)). Higher-resolution follow-up observations are needed to establish the association between the droplets and the YSOs found within their boundaries and the effects of the YSOs on the evolution of droplets.

In conclusion, droplets are a previously omitted subpopulation of coherent structures. Although imminent star formation within droplets is unlikely because of the gravitational unboundedness, droplets might form from the same set of physical processes that lead to the formation of star-forming coherent cores. Because the subsonic velocity dispersion within a coherent core is expected to be disturbed by ongoing formation of stars, droplets may provide a precious chance to examine the internal kinematics and the formation of coherent structures. Furthermore, there could exist an evolutionary sequence connecting the pressure-dominated droplets to the star-forming coherent cores, but this cannot be confirmed with present data. More works to systematically examine droplets in simulations and to compare them with droplets and other cores identified in observations are needed to answer the following questions: How do droplets form? Do droplets evolve into star-forming cores, and if so, how? What is the relation between coherent structures, including both star-forming coherent cores and pressure-dominated droplets, and other populations of cores (e.g., starless and protostellar cores) and structures (e.g., filaments and bundles Hacar et al. 2013)? Are there observable velocity gradients and potentially associated rotational and/or shear motions in the interiors of coherent structures? Would the coherent structures fragment into smaller features in the future? We will address some of these questions in subsequent papers of this series.

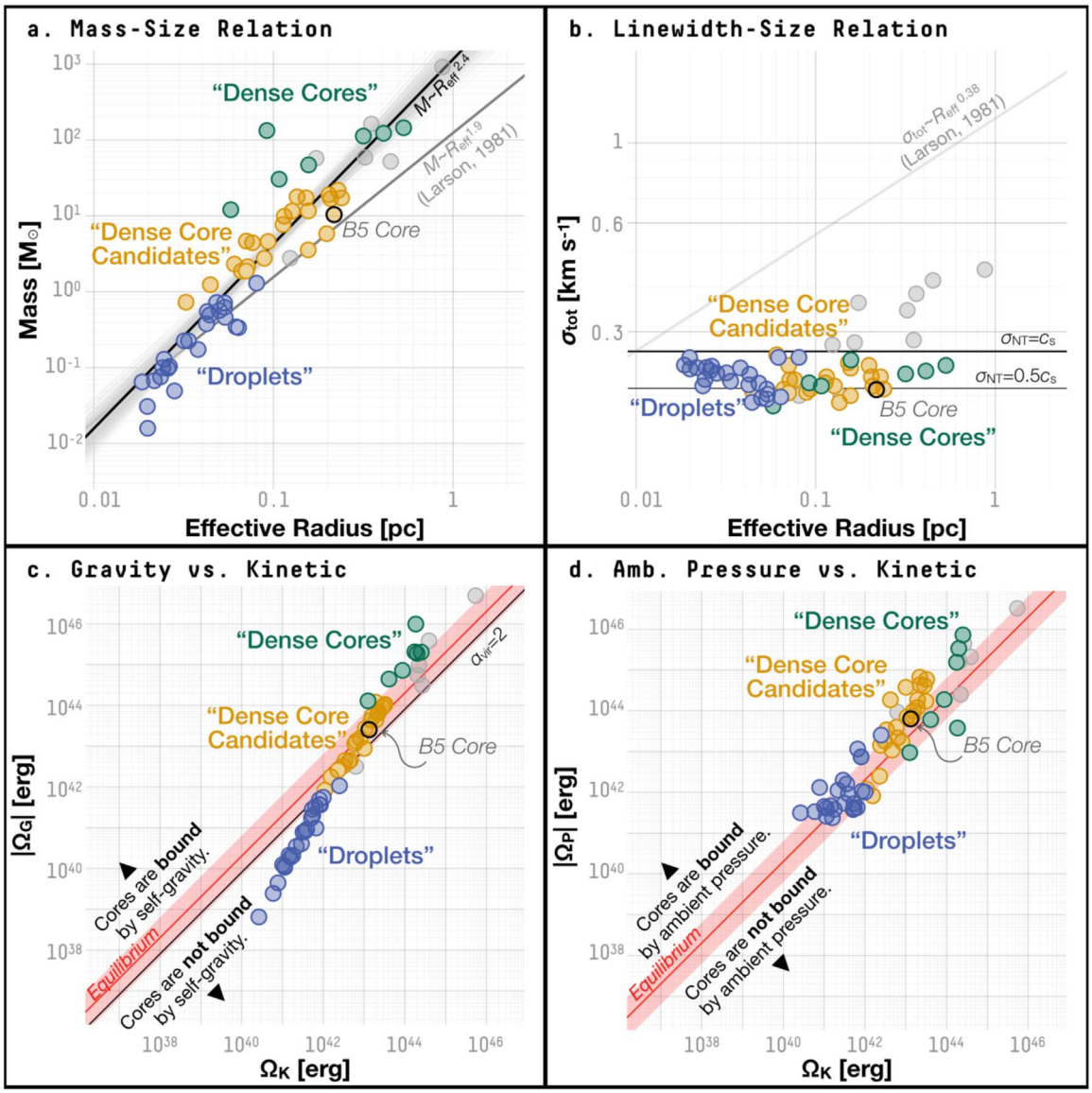

Figure 22. Like Figures 9 and 10, but color coded for recategorized structures: the "dense cores" (dark green circles), the "dense core candidates" (dark yellow circles), and the "droplets" (dark blue circles). Structures that have supersonic velocity dispersions are omitted in this recategorization and plotted as gray circles. (a) The mass–size distribution (see Figure 9(a)). (b) The $\sigma_{\rm tot}$-size distribution (see Figure 9(b)). (c) Gravitational potential energy, $\Omega_{\rm G}$, plotted against internal kinetic energy, $\Omega_{\rm K}$ (see Figure 10(a)). (d) The energy term representing the confinement provided by the ambient gas pressure, $\Omega_{\rm P}$, plotted against the internal kinetic energy, $\Omega_{\rm K}$ (see Figure 10(b)).

5. Conclusion

In search of coherent structures defined by a change in velocity dispersion from supersonic to nearly constant subsonic values (Section 3.1; Figures 1, 2, and 5 for L1688, and Figures 3, 4, and 6 for B18), we identify a total of 18 coherent structures in the L1688 region of Ophiuchus and the B18 region of Taurus, using data from the first data release of the GAS (see Section 2.1; Friesen et al. 2017). The 18 coherent structures newly identified within a total projected area of $\sim$0.6 pc^2 suggest that the coherent structures are ubiquitous in nearby molecular clouds and allow statistical analyses of coherent structures for the first time.

The newly identified coherent structures have a typical radius of 0.04 pc and a typical mass of 0.4 $M_\odot$ (Section 3.2; Table 1). They appear to follow the same relation between mass size and line width size as the dense cores previously examined by Goodman et al. (1993), many of which were later found to be coherent cores (Figure 9) (Goodman et al. 1998; Caselli et al. 2002; Pineda et al. 2010). In a virial analysis, we find that the newly identified coherent structures are not virially bound by self-gravity and are instead confined by the pressure provided by the ambient gas motions (see Section 3.3). This clearly differentiates the newly identified coherent structures from previously known coherent cores, which have been found to be gravitationally bound and sometimes hosting ongoing star formation (Pineda et al. 2010, 2015). We refer to this newly discovered population of gravitationally unbound and pressure confined coherent structures as droplets.

The radial density and pressure profiles of the droplets cannot be described well by either a critical Bonnor–Ebert sphere or a logotropic sphere (see Sections 4.1.1 and 4.1.2). The droplets have relatively shallow density profiles (e.g., compared to previously observed starless cores; see Figure 12(b)), and their density profiles can generally be

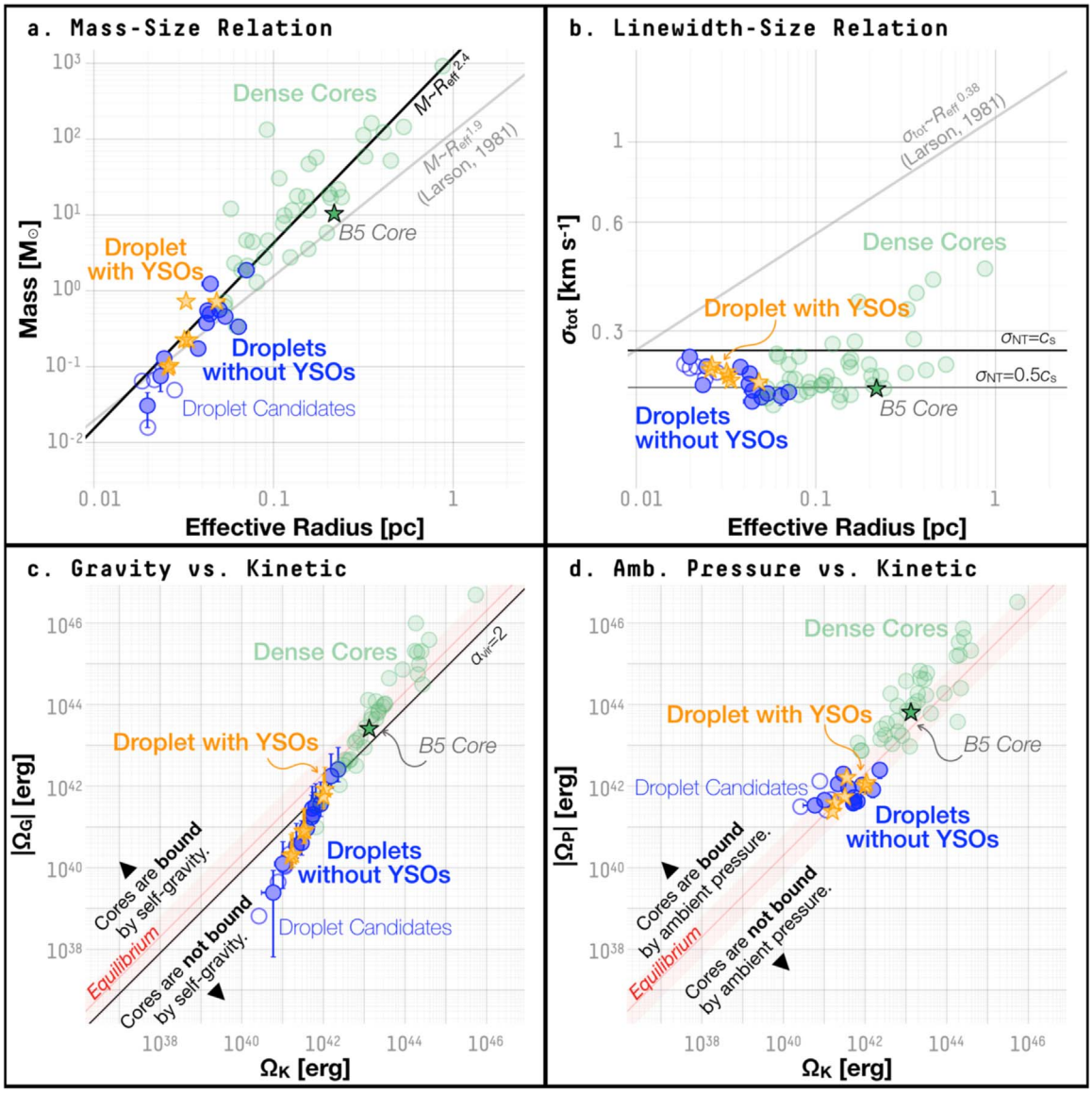

Figure 23. Like Figures 9 and 10, but marked for the droplets with YSOs within the boundaries (yellow star marks) and the droplets without YSOs within boundaries (blue circles), in comparison to the dense cores (green circles) and the coherent core in B5 (the green star mark; the coherent core in B5 has at least one YSO within its boundary). (a) The mass–size distribution (see Figure 9(a)). (b) The $\sigma_{\rm tot}$-size distribution (see Figure 9(b)). (c) Gravitational potential energy, $\Omega_{\rm G}$, plotted against internal kinetic energy, $\Omega_{\rm K}$ (see Figure 10(a)). (d) The energy term representing the confinement provided by the ambient gas pressure, $\Omega_{\rm P}$, plotted against the internal kinetic energy, $\Omega_{\rm K}$ (see Figure 10(b)).

approximated by a constant density at smaller radial distances and a power-law density distribution approaching $\rho \propto r^{-1}$ at larger distances, the latter of which has been observed toward cloud-scale structures (Figure 12). While the droplets are sometimes found at local extremes of the line-of-sight velocity, the $V_{\rm LSR}$ distribution of the droplets has a shape similar to that of the average NH_3 line profile (see Section 4.1.3; see also Figures 16 and 17). Both the power-law density profiles ($\rho \propto r^{-1}$) and the distribution of $V_{\rm LSR}$ suggest a close relation between the droplets and the natal cloud environment.

By identifying droplet-like structures in the synthesized NH_3 cube, we demonstrate that the formation of droplets is possible in an MHD simulation of a star-forming cloud. The droplet-like structures examined in Section 4.2 appear to correspond to shock-induced features in the simulation, and throughout the evolution, material accumulates at shock-induced converging points. Given that the active star formation in the same simulation emerges in regions near the converging points of multiple shocks, we speculate that a droplet might evolve into a star-forming core if accumulation continues and/or if the associated shock-induced feature converges/collides with other shocks.

More work is needed to understand the formation and evolution of droplets and coherent structures in general. With the GAS data, we hope to extend our analyses on coherent structures to other nearby molecular clouds. The GAS observations of NH_3 hyperfine line emission also allow an analysis of the internal velocity structures, which would shed light on the potential rotational and shear motions in the droplets/coherent cores. On the other hand, more targeted modeling and a statistical approach are needed to further understand the physical processes involved in the formation of droplets and the role droplets might play in star formation.

The National Radio Astronomy Observatory is a facility of the National Science Foundation operated under cooperative agreement by Associated Universities, Inc. This work was supported by a Cottrell Scholar Award. A.P. acknowledges the support of the Russian Science Foundation project 18-12-00351.

Facilities: GBT (KFPA+VEGAS), *Herschel Space Observatory* (PACS+SPIRE).

Software: astropy (The Astropy Collaboration et al. 2018), Glue (Beaumont et al. 2015; Robitaille et al. 2017), PySpecKit (Ginsburg & Mirocha 2011), RADMC-3D (Dullemond et al. 2012).

Appendix A
Summary of Updated Distances for Cores Presented by Goodman et al. (1993)

To compare the droplets identified in this work to previously known dense cores, we update the physical properties summarized in Goodman et al. (1993) to more recent distance measurements. The updated distances are summarized below:

1. Regions associated with the molecular cloud in Perseus: PER3, PER6, and B5. We adopt distances measured by Schlafly et al. (2014) using *PanSTARRS-1* photometry, which are 260 ± 26 pc for the western part of the Perseus molecular cloud (including PER3 and PER6) and 315 ± 32 pc for the eastern part (including B5).
2. Regions associated with the molecular cloud in Taurus: L1489, L1498, L1495, L1495NW, L1495SE, TAU11, TAU16, B217, L1524, TMC-2A, L1534 (TMC-1A), L1527, TMC-1C, and L1517B. We adopt a distance of 126.6 ± 1.7 pc, measured by Galli et al. (2018).
3. Regions associated with λ Orionis: L1582A and B35A. We adopt a distance of 420 ± 42 pc, measured by Schlafly et al. (2014).
4. A region associated with the molecular cloud and the YSO cluster in Ophiuchus (sometimes referred to as "ρ Oph"): L1696A. We adopt a distance of 137.3 ± 6 pc, measured by Ortiz-León et al. (2017) using parallax.
5. Regions associated with clouds and clumps in Oph N: L43/RNO90, L43, L260 (a.k.a. L255), L158, L234E, L234A, and L63. These regions are usually associated with the Ophiuchus complex—or, on a larger scope, the Upper Sco-Oph-Cen complex. Goodman et al. (1993) adopted the same distance for these regions as for L1696A. Here, we use an updated distance measurement of 125 ± 18 pc to the Ophiuchus complex from Schlafly et al. (2014). This is in good agreement with the widely used 125 ± 45 pc, measured by de Geus et al. (1989).
6. Regions associated with Cepheus Flare: the Cepheus Flare spans more than 10° from north to south on the plane of the sky, and is known to have a complicated structure with multiple concentrations of material at different distances. Here, we adopt different distance measurements for different regions in Cepheus Flare, and note that these distances were used by Kauffmann et al. (2008) side-by-side. Note that Schlafly et al. (2014) measured 360 ± 35 pc for the southern part of Cepheus Flare and 900 ± 90 pc for the northern part of Cepheus Flare. See discussions in Schlafly et al. (2014).
   (i) L1152: 325 ± 13 pc, measured by Straizys et al. (1992) using photometry.
   (ii) L1082C, L1082A, and L1082B: 400 ± 50 pc, measured by Bourke et al. (1995) using photometry.
   (iii) L1174 and L1172A: 288 ± 25 pc, measured by Straizys et al. (1992) using photometry.
   (iv) L1251A, L1251E, and L1262A: we update the distance used by Kauffmann et al. (2008) based on (Kun 1998, 300^{+50}_{-10} pc) with a more recent measurement of 286 ± 20 pc made by Zdanavičius et al. (2011) using photometry.
7. Regions with distances measured from masers:
   (i) L1400G and L1400K: 170 ± 50 pc, measured by Montillaud et al. (2015).
   (ii) L134A: 110 ± 10 pc, measured by Montillaud et al. (2015).
8. Other regions for which the distances have not updated since the 1990s but have been cited recently. Here, we provide a list of the original references and the most recent year when each reference was cited.
   (i) L483: 200 pc, from Dame & Thaddeus (1985), with citations as recent as 2017.
   (ii) L778: 200 pc, from Schneider & Elmegreen (1979), with citations as recent as 2017.
   (iii) B361: 350 pc, from Schmidt (1975), with citations as recent as 2010.
   (iv) L1031B: 900 pc, from Hilton & Lahulla (1995), with citations as recent as 2017.

The resulting change in distance, D, affects the measured radius, R, of each core listed in Table 1 in Goodman et al. (1993) according to a linear relation, $R \propto D$. Because Goodman et al. (1993) calculated the mass based on volume density derived from NH_3 hyperfine line fitting, the change in distance affects the mass by $M \propto D^3$. See Section 2.3.1 for details.

Appendix B
A Gallery of Close-up Views of the Droplets and the Droplet Candidates

In Section 3.1, we explain the steps we take to identify the droplets and the droplet candidates. The resulting droplets and droplet candidates are shown in Figures 1, 2, and 5 for L1688, and Figures 3, 4, and 6 for B18. Here, we provide a gallery of close-up views of these droplets and droplet candidates. The gallery can be found at https://github.com/hopehhchen/Droplets/tree/master/Droplets/plots/droplets.

The quantity shown in each panel of the figure is denoted in the top left corner, where N_{H_2} is the *Herschel* column density, T_{dust} is the *Herschel* dust temperature, T_{peak} is the NH_3 brightness, σ_{NH_3} is the observed NH_3 velocity dispersion, V_{LSR} is the velocity centroid from fitting the NH_3 (1, 1) hyperfine line profile, and T_{kin} is the kinetic temperature from fitting the NH_3 (1, 1) and (2, 2) profiles (hence its smaller footprint due to the lack of detection of the NH_3 (2, 2) emission at some pixels).

The thick contour (black or white) in each panel marks the outline of the mask used to define the boundary of the droplet. The crosshair and the circle (red or blue) show the position centroid and the effective radius (R_{eff}) of the droplet. The red contour in the panel that shows the observed NH_3 velocity dispersion (σ_{NH_3}) corresponds to the outline of the regions where velocity dispersion is found to be subsonic.

Due to the varying contrast, we adjust the color scale used in each panel from droplet to droplet, but the span of the color scale between the two extreme colors remains the same for

each quantity across different droplets. The gray scale used to plot N_{H_2} ranges from lower column density in lighter gray to higher column density in darker gray, and spans a total of one order of magnitude in column density (from white, signifying the lowest column density, to black, the highest column density). The color scale used to plot T_{dust} ranges from lower dust temperature in darker orange to higher dust temperature in lighter yellow, and spans a total of six degrees in dust temperature (from dark red, signifying the lowest dust temperature, to light yellow, the highest dust temperature). Similar to the gray scale used to plot N_{H_2}, the gray scale used to plot T_{peak} spans a total of an order of magnitude in NH_3 brightness (from white, signifying the lowest T_{peak}, to black, the T_{peak}). The color scale used to plot σ_{NH_3} is fixed and shows observed NH_3 velocity dispersion between 0.05 km s^{-1} (light yellow) to 0.40 km s^{-1} (dark blue). The color scale used to plot V_{LSR} ranges from more redshifted V_{LSR} in red to more blueshifted V_{LSR} in blue. Similar to the color scale used to plot T_{dust}, the color scale used to plot T_{kin} spans a total of six degrees in dust temperature (from dark red, signifying the lowest kinetic temperature temperature, to light yellow, the highest kinetic temperature temperature).

The physical scale on the plane of the sky is noted by the horizontal line in the top right corner. The black circular area in the lower left corner corresponds to the GAS beam at 23 GHz.

Appendix C
Droplets at Positions of Dense Cores and Other Known Structures

Two of the 18 droplets defined in Section 3.1 are found near the positions of two dense cores observed and analyzed by Benson & Myers (1989), Goodman et al. (1993), and Ladd et al. (1994). These droplets are L1688-d11 and B18-d4, with centroid positions found within one GBT FWHM beam size (32″) of the centers of L1696A and TMC-2A, respectively. Figure 24 shows how the basic properties measured in this work using data from the GAS compare to properties measured by Benson & Myers (1989), Goodman et al. (1993), and Ladd et al. (1994). We note that the observations done by Benson & Myers (1989) and Ladd et al. (1994) did not spatially resolve the "transition to coherence" (Goodman et al. 1998), as was done by Pineda et al. (2010) for B5. For reference, the spatial resolution of the observations done by Benson & Myers (1989) and Ladd et al. (1994) is a factor of ∼2.5 coarser than that of modern GBT observations. The velocity resolution (at 23 GHz) of the observations done by Benson & Myers (1989) and Ladd et al. (1994) ranges from 0.07 to 0.20 km s^{-1}, compared to 0.07 km s^{-1} of the GBT observations done by the GAS (Friesen et al. 2017). See Section 2 for details.

Here, we also list previously known cores and density features potentially associated with droplets in Tables 7 and 8, based on a thorough search of the SIMBAD Astronomical Database.[29]

We can also compare the physical properties of droplets to cores found similarly in nearby molecular clouds. Risking comparing measurements that are biased by the difference in observation setups and the methods used in analyses, Figure 25 shows a comparison of physical properties between the droplets and the core populations found in Ophiuchus, Orion B, and the Pipe Nebula, respectively observed and analyzed by Johnstone et al. (2000, 2001), and Lada et al. (2008) (see also Section 3.3.3; distances have been updated with modern measurements). Like droplets, many of these cores are also found to be unbound by self-gravity, and the ambient pressure likely contributes to the confinement of these cores (Johnstone et al. 2000; Lada et al. 2008). In general, these cores have physical properties comparable to those of the droplets and some of the dense cores. A more careful treatment of differences in observational setups and the methods used to define the structures is needed to fully understand the relation between the droplets and these cores. We leave a comprehensive comparison between droplets and previously observed cores to future work.

[29] The database can be accessed via http://simbad.u-strasbg.fr/simbad/. As pointed out on the SIMBAD Astronomical Database page, while the database includes most of the published catalogs, it is by no means complete.

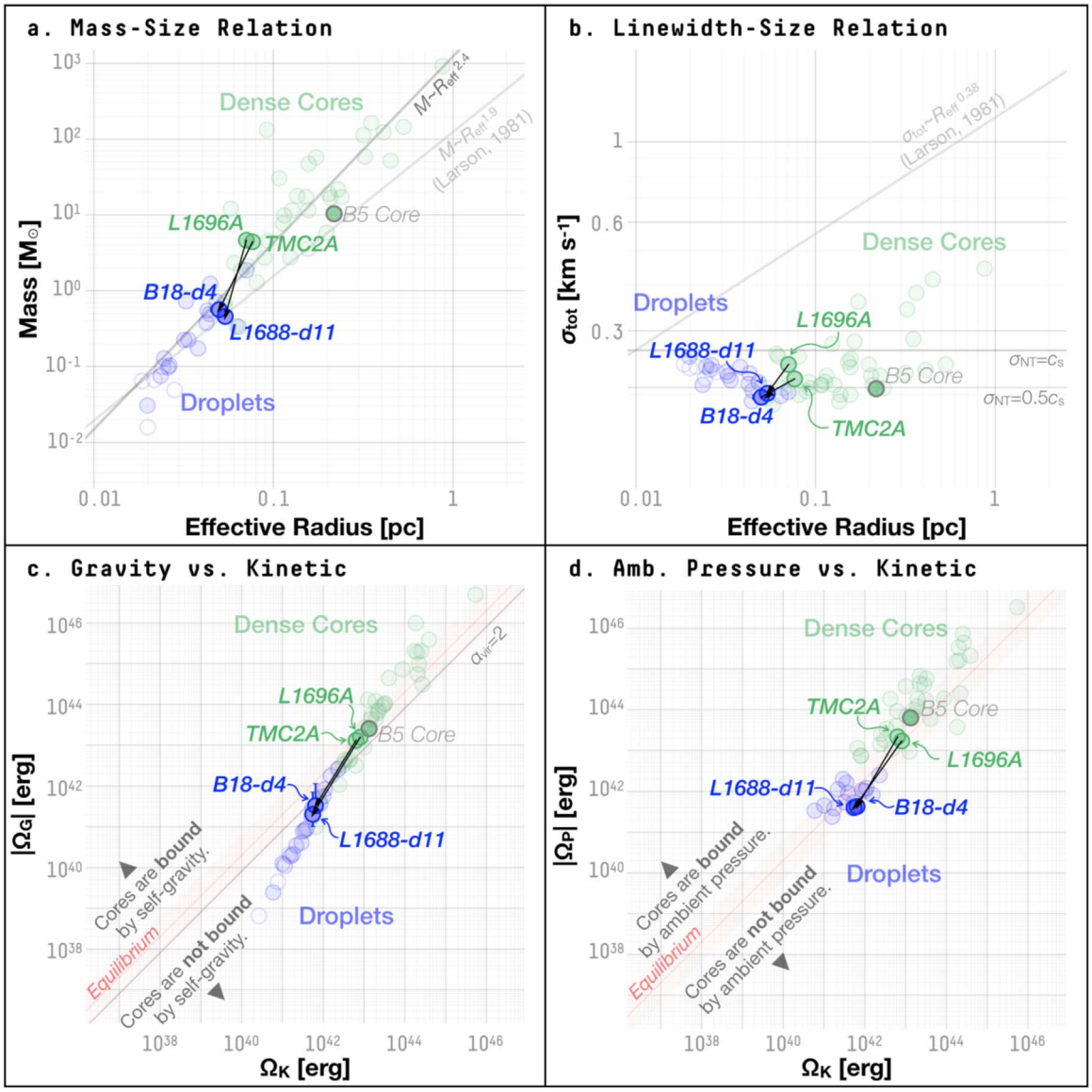

Figure 24. (a) The mass–size distribution of the droplets identified in this work (blue circles) and the dense cores examined by Goodman et al. (1993) (green circles). The droplets found at positions of known dense cores and the corresponding dense cores are highlighted and connected by black lines. These are L1688-d11, found at the position of L1696A, and B18-d4, found at the position of TMC-2A. As in Figure 9(a), the black line shows a power-law relation between the mass and the effective radius, and a randomly selected 10% of the accepted parameters in the MCMC chain used to find the power-law fit are plotted as transparent lines for reference. The solid gray line shows the empirical relation based on observations of larger-scale structures examined by Larson (1981). (b) The $\sigma_{\rm tot}$-size distribution of the same structures shown in (a). As in Figure 9(b), the horizontal lines show $\sigma_{\rm tot}$ expected for structures where the nonthermal component is equal to the sonic speed ($c_{\rm s}$; thicker line) and half the sonic speed (thinner line) of a medium with a mean molecular weight of 2.37 u at a temperature of 10 K. (c) Gravitational potential energy, $\Omega_{\rm G}$, plotted against internal kinetic energy, $\Omega_{\rm K}$ (Equation (2)), for the same structures shown in (a). As in Figure 10(a), the red band from the lower left to the top right marks the equilibrium between $\Omega_{\rm G}$ and $\Omega_{\rm K}$ (solid red line) within an order of magnitude (pink band), according to the virial equation (Equation (2); omitting the pressure term). The black line marks where the conventional virial parameter, $\alpha_{\rm vir}$, has a value of 2. (d) The energy term representing the confinement provided by the ambient gas pressure, $\Omega_{\rm P}$, plotted against the internal kinetic energy, $\Omega_{\rm K}$ (Equation (2)), for the same structures shown in (a). As in Figure 10(b), the red band from the lower left to the top right marks an equilibrium between $\Omega_{\rm P}$ and $\Omega_{\rm K}$ (solid red line) within an order of magnitude (pink red band), according to the virial equation (Equation (2); omitting the gravitational term). Structures in the parameter space above the red line (equilibrium) are expected to be dominated by the ambient gas pressure.

Table 7
Droplets and Previously Known Objects Potentially Associated with Each Droplet[a]

ID	Features Located within 32″[b]	
L1688-d1	Core 18 (M10[c])/MMS055 (S06[d])	
L1688-d2	Core 23, 24, 25 (M10)	
L1688-d3	[Oph C-N][e]/Core 27 (M10)	
L1688-d4	Bolo 12 (Y06[f])/Oph C-MM4, MM5, MM6 (M98[g])/Oph C-HC$_5$N, C$_2$S, A1, A3 (F09[h])/MMS022 (S06)	
L1688-d5	Oph E-MM2c, MM8 (M98)/Core 31 (M10)	
L1688-d6	Oph F-MM2b, MM3 (M98)/Core 46 (M10)/Oph F-A2, A3 (F09)/[Oph F-1]	
L1688-d7	[Oph F]/Oph F-MM8 (M98)	
L1688-d8	Core 59 (M10)/[Oph E-1]/MMS081 (S06)	
L1688-d9	Bolo 24 (Y06)	
L1688-d10	MMS126 (S06)/Core 67 (M10)	
L1688-d11	[L1696A]/[Oph D]	
L1688-d12	[L1696B]/MMS041, MMS075 (S06)	
L1688-c2[i]		…
L1688-c3	Oph C-A2 (F09)/Oph C-MM12 (M98)	
L1688-c4	Oph B3-N1 (F10[j])/Oph B3-A1 (F09)	
B18-d1		…
B18-d2		…
B18-d3	L1524-4 (L99[k])/L1524-4 C1 (K08[l])	
B18-d4	B18-1 C1 (K08)/MC 31 (O02[m])	
B18-d5	[TMC-2]	
B18-d6		…

Notes.
[a] This table is based on the SIMBAD Astronomical Database and lists only molecular clouds (or a subpart of it), cores, and features identified in millimeter/submillimeter emission. Other types of objects, including YSOs and Herbig-Haro objects, are excluded from this table. For many droplets, multiple objects identified using observations made with the Submillimeter Common-User Bolometer Array (SCUBA) on the James Clerk Maxwell Telescope (JCMT) are found within a GBT beam FWHM from the droplet centroid. To be concise, we omit these objects and point to catalogs presented by Johnstone et al. (2000), Jørgensen et al. (2008), and Gurney et al. (2008).
[b] Angular distances from the droplet centroids listed in Table 1. The angular distance of 32″ corresponds to the GBT beam FWHM at 23 GHz and is ∼0.02 pc at the distances of Ophiuchus and Taurus. The angular distance of 96″ is three times the GBT beam FWHM and is ∼0.06 pc at the distances of Ophiuchus and Taurus. The third column ("features located within 96″") does not repeat features listed in the second column ("features located within 32″"). See Section 2.1.
[c] M10: Maruta et al. (2010). The objects are grouped by catalogs and ordered by the distance of the the object closest to each droplet on the plane of the sky in each catalog.
[d] S06: Stanke et al. (2006).
[e] Object names enclosed in square brackets are names of molecular clouds or subparts of a molecular cloud. These often point to relatively loosely defined regions within a molecular cloud, and the names have often been in use in the literature for decades.
[f] Y06: Young et al. (2006).
[g] M98: Motte et al. (1998).
[h] F09: Friesen et al. (2009).
[i] Because L1688-c1E and L1688-c1W overlap with L1688-d1, they are not listed here where the associations are purely based on the locations of the objects.
[j] F10: Friesen et al. (2010).
[k] L99: Lee et al. (1999).
[l] K08: Kauffmann et al. (2008).
[m] O02: Onishi et al. (2002). MC stands for "molecular condensation."

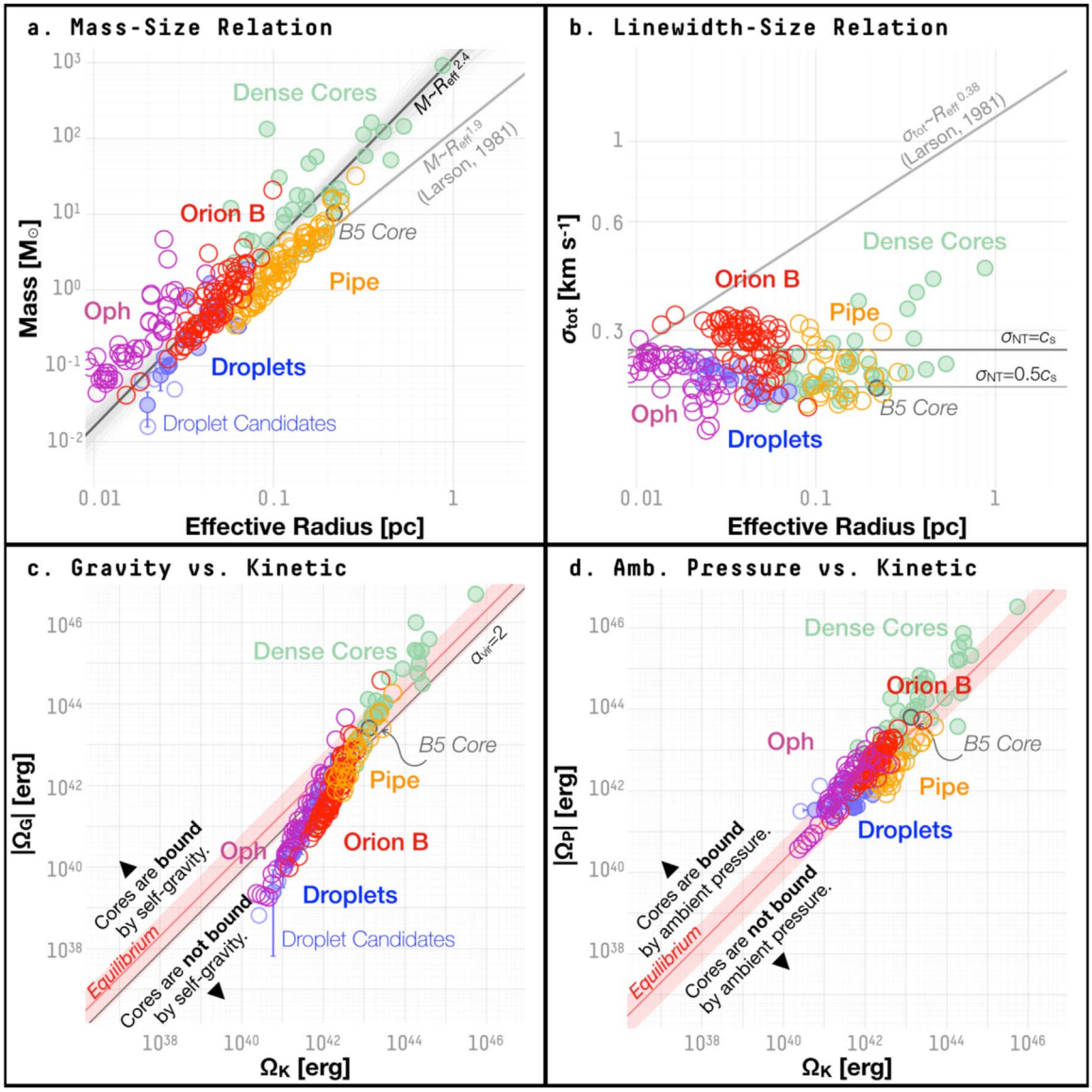

Figure 25. Like Figures 9 and 10, but plotted with previous observations of cores in Ophiuchus (purple circles), Orion B (red circles), and the Pipe Nebula (yellow circles). (a) The mass–size distribution (see Figure 9(a)). (b) The σ_{tot}-size distribution (see Figure 9(b)). (c) Gravitational potential energy, Ω_G, plotted against internal kinetic energy, Ω_K (see Figure 10(a)). (d) The energy term representing the confinement provided by the ambient gas pressure, Ω_P, plotted against the internal kinetic energy, Ω_K (see Figure 10(b)).

Table 8
Droplets and Previously Known Objects Potentially Associated with Each Droplet (3×GBT FWHM)[a]

ID	Features Located within 96″ (but Outside 32″)
L1688-d1	[Oph C-W]/Oph C-MM9 (M98)
L1688-d2	Oph E-MM1 (M98)/Core 28 (M10)/MMS068 (S06)
L1688-d3	MMS044 (S06)/Oph C-MM10, MM12 (M98)/Oph C-A2 (F09)
L1688-d4	Core 29 (M10)/MMS039, MMS059 (S06)/Oph C-MM1, MM2, MM7, MM12 (M98)/Oph C-A2 (F09)
L1688-d5	Oph E-MM2b, MM9 (M98)/[Oph E]/Core 34 (M10)
L1688-d6	Oph F-MM2, MM2a (M98)/Core 44, 51, 52 (M10)/Oph F-A1 (F09)/MMS040 (S06)
L1688-d7	Oph F-MM6, MM7, MM9 (M98)/[L1681B]/SMM073 (S06)/Core 57, 58 (M10)
L1688-d8	…
L1688-d9	Core 61, 62, 63, 64 (M10)/MMS051 (S06)
L1688-d10	Core 66, 68 (M10)/MMS060 (S06)
L1688-d11	R26 (L89[b])/Oph D-MM1, MM3, MM4, MM5 (M98)/MMS047, MMS052 (S06)/Bolo 27 (Y06)
L1688-d12	Oph I-MM1 (M98)
L1688-c2	Core 27 (M10)/MMS044 (S06)/[Oph C-N]
L1688-c3	Oph C-MM2, MM4, MM5, MM10 (M98)/Oph C-C_2S, A1, HC_5N (F09)/[Oph C]/Bolo 12 (Y06)/MMS044 (S06)
L1688-c4	[Oph B-3]/Core 42, 47 (M10)/MMS108, MMS 143 (S06)
B18-d1	…
B18-d2	MC 29 (O02)/[L1524]
B18-d3	MC 29 (O02)
B18-d4	B18-1 (L99)/[TMC-2A]
B18-d5	TMC-2 C1 (K08)/TMC-2 (L99)/MC 33b (O02)/Tau E2 (W94[c])
B18-d6	B18-4 C1 (K08)/MC 35 (O02)/[TMC-3B, 3A & B18-I]/B18-4 (L99)

Notes.
[a] This table is like Table 7, but lists objects that are within 96″ (but outside 32″) from the droplet centroids on the plane of the sky. The angular distance of 96″ is three times the GBT beam FWHM and is ∼0.06 pc at the distances of Ophiuchus and Taurus. The notations remain the same.
[b] L89: Loren (1989).
[c] W94: Wood et al. (1994).

Appendix D
Uncertainty in the Radius Measurement

The uncertainty in the radius measurement lies in two aspects. First, the radius measurement is limited by the intrinsic resolution of the observations. In the case of this paper, because the droplet boundary is defined by the change in line width based on GBT observations of NH_3 emission, the uncertainty in the radius measurement scales with the pixel size of the line width map. For the Nyquist-sampled line width map produced by Friesen et al. (2017), the pixel size equals ∼0.007 pc at the distance of L1688 and B18.

Second, because the droplet boundary is not perfectly circular, assigning a single number to describe the size (radius) of the droplet boundary is subject to the uncertainty due to the noncircular shape of the boundary. In this paper, we estimate the lower and the upper bounds of the radius by measuring the radius of the largest circle that can be enclosed by the droplet boundary and the smallest circle that can enclose the droplet boundary, respectively. See Figure 26.

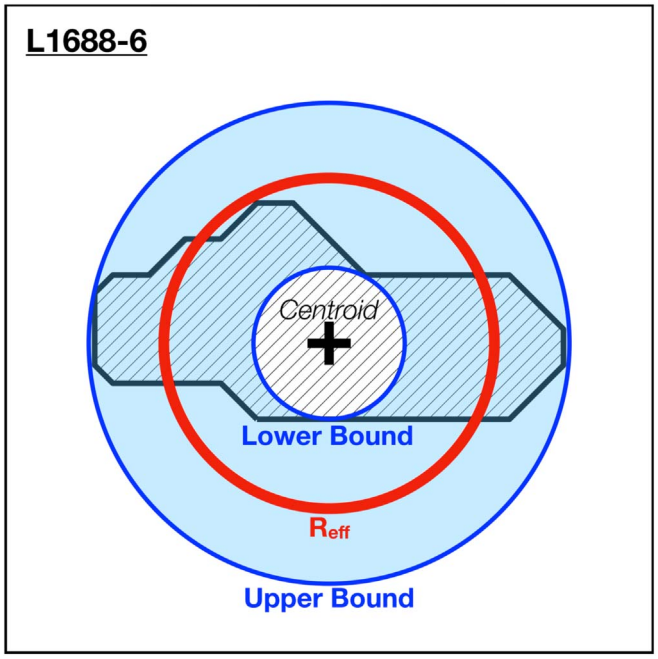

Figure 26. Droplet L1688-d6 as an example of how the lower and the upper bounds of the radius measurement are defined. The droplet is shown as an irregular hatched area. The red circle shows the effective radius, $R_{\rm eff}$, derived from the principal component analysis (PCA) weighted by the peak NH_3 brightness, $T_{\rm peak}$ (see Section 3.2). The inner blue circle marks the largest circle that can be enclosed by the droplet boundary, which we use as the lower bound in the radius measurement. The outer blue circle marks the smallest circle that can *enclose* the droplet boundary, which we use as the upper bound in the radius measurement. Notice that the circles used in determining the lower and upper bounds are required to center at the position centroid of the droplet (the positions listed in Table 1).

The difference between $R_{\rm eff}$ and the lower or upper bound of the radius is then required to be larger than the uncertainty due to the finite resolution of the GBT observations (i.e., $\gtrsim$0.02 pc at the distances of L1688 and B18). The resulting uncertainty is listed in Table 1.

Apart from using the PCA (see Section 3.2) to find the radius, another common way to determine "effective radius" for a noncircular shape is to measure the projected area, A, and find the radius of the circle that has the same area (e.g., Rosolowsky & Leroy 2006). The effective radius found through the projected area is then:

$$R_{\rm eff,A} = \sqrt{\frac{A}{\pi}}. \quad (9)$$

For each droplet, $R_{\rm eff,A}$ lies within the range between the lower and the upper bounds determined using the enclosed circles (see above and Figure 26), and deviates by less than 10% from $R_{\rm eff}$, determined from the PCA. For example, this translates to $\lesssim$10% of difference in the gravitational potential energy, Ω_G. In the analyses presented in this paper, the uncertainty in $R_{\rm eff}$ determined using the lower and upper bounds (Figure 26) is propagated to the uncertainties of other quantities, which are shown in corresponding plots and tables. Because $R_{\rm eff,A}$ lies between the lower and upper bounds determined for the radius measurement, using $R_{\rm eff,A}$, instead of $R_{\rm eff}$, in these analyses will only have an effect within the uncertainty reported throughout this paper.

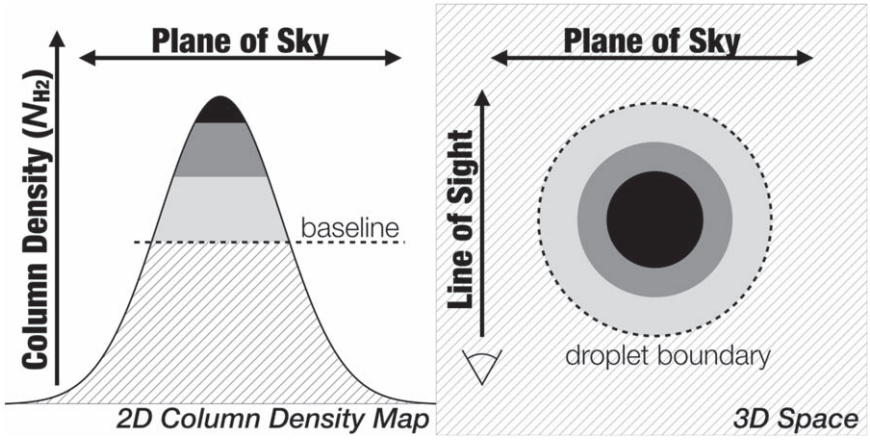

Figure 27. This cartoon shows the corresponding "layers" of material along a cut on the 2D column density map (left; with the vertical axis corresponding to the column density) and in a top-down view in the 3D space (right; with the line of sight along the vertical axis). The solid shaded area (in black/gray/dark gray) corresponds to materials inside a schematic spherical "droplet," while the hatched area corresponds to the material outside the droplet. On the right-hand side, the dashed line marks the boundary of the droplet in the 3D space. On the left-hand side, the dashed line shows how a constant column density baseline, corresponding to the minimum value of the solid shaded area, can be a reasonable estimate of the contribution from material outside the droplet (hatched area). The baseline subtraction method is similar to the "clipping paradigm" analyzed by Rosolowsky et al. (2008b) and applied by Pineda et al. (2015) to mass measurements of features with densities below 0.1 pc.

Appendix E
Baseline Subtraction

In the analyses presented in this paper, the mass and related quantities such as the density are estimated after a baseline correction for the line-of-sight material outside the targeted volume. The method we apply in this paper is similar to the "clipping paradigm" examined by Rosolowsky et al. (2008b) to estimate the physical properties of a compact structure. The clipping method produces a mass estimate that would correspond better to the mass calculated from fitting the NH_3 emission, which traces only the material within the targeted structure and was used by Goodman et al. (1993) to estimate the masses of the dense cores (see Section 2.3.1). Figure 27 schematically demonstrates how the clipping paradigm can be a reasonable way to remove the contribution to column density measurements from the material along the same line of sight but outside the targeted structure. In the virial analysis presented in Section 3.3 and in the analyses of the radial density profiles presented in Sections 4.1.1 and 4.1.2, we use the same method to estimate the density of the gas surrounding the volume under discussion.

In comparison, a simple sum of column densities measured within a certain projected area on the plane of the sky overestimates the mass by including the contribution from the material along the entire line of sight (see Figure 28). Similarly, when estimating the average density within a shell-shaped volume surrounding the targeted structure (as done in Section 3.3.3), summing the column densities measured within a ring-shaped area on the plane of the sky overestimates the mass—and hence, the density as well (different shades of gray in Figure 28). The typical difference between the mass estimated after applying the clipping and the mass estimated without any clipping (a simple sum) is ∼25%. In the virial analysis presented in Section 3.3, this amounts to ∼50% of uncertainty in the estimate of the gravitational potential energy and ∼25% of uncertainty in either of the kinetic energy and the energy term representing the ambient gas pressure confinement. These uncertainties are included in the uncertainties listed in Table 2 and do not qualitatively change the results presented in subsequent discussions.

More sophisticated ways to remove contributions from material in the foreground and background may involve removing contributions from column density structures larger than a certain size scale—for example, using a transform algorithm like the wavelet decomposition. While such algorithms perform well in analyses of compact structures, the uncertainty becomes unclear if we are interested in both the mass within the targeted structure (as we are in Section 3.2) and the density of the surrounding material (as we are in Section 3.3.3). A single background removal can result in an overestimated mass of the structure at the center (the black areas in Figure 29, compared to Figure 27), and when estimating the density of the surrounding material, a single background removal would give an estimate for a hollow cylindrical volume instead of the shell-shaped volume (different shades of gray in Figure 29, compared to Figure 27). While we can, in principle, resolve the issue by optimizing the transform algorithm to perform differently for different purposes, our reasons for adopting the clipping method in this paper are twofold: (1) to fully avoid double counting the contribution from the material in the same volume when estimating the mass in *and* outside a structure, and (2) for its simplicity and ease of error estimation. As demonstrated in Figure 27, if the structure is spherical, the clipping method would give the exact masses for the layers of materials at different radial distances.

The main uncertainty resulting from using the clipping method with circular annuli (as done in Sections 3.3.3, 4.1.1, and 4.1.2) is then the deviation in the shape of the targeted structure from a sphere. As mentioned in Section 3.1, most of the droplets have aspect ratios between 1 and 2, with the exceptions of L1688-d1 (with an aspect ratio of ∼2.50), L1688-d6 (with an aspect ratio of ∼2.52), and B18-d5 (with an aspect ratio of ∼2.03). Thus, we estimate that the uncertainty resulting from using circular annuli is no larger than a factor of 2. See discussions in Appendix D.

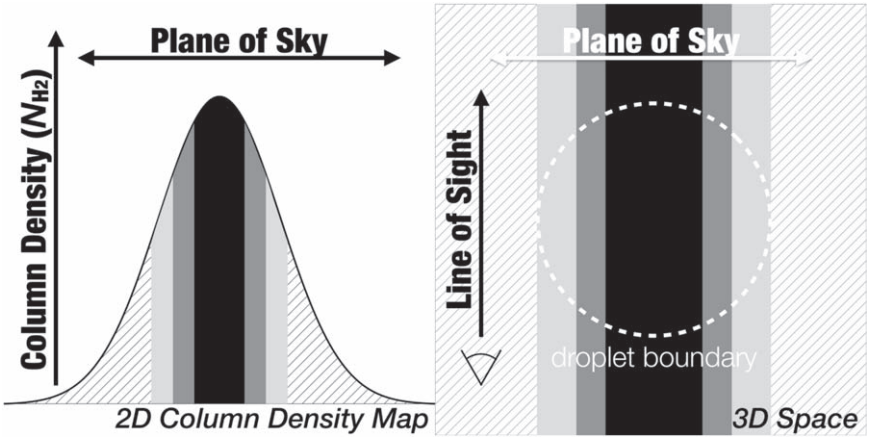

Figure 28. This cartoon shows the mass (integrated column density) on a column density distribution derived from a 2D column density map (left; with the vertical axis corresponding to the column density) and the corresponding volumes in the 3D space (right; with the line of sight along the vertical axis), if no baseline removal is applied. The solid shaded area (in black/dark gray/gray) corresponds to the mass (integrated column density) estimated from the 2D column density map (left) and the material occupying the corresponding volume in the 3D space (right).

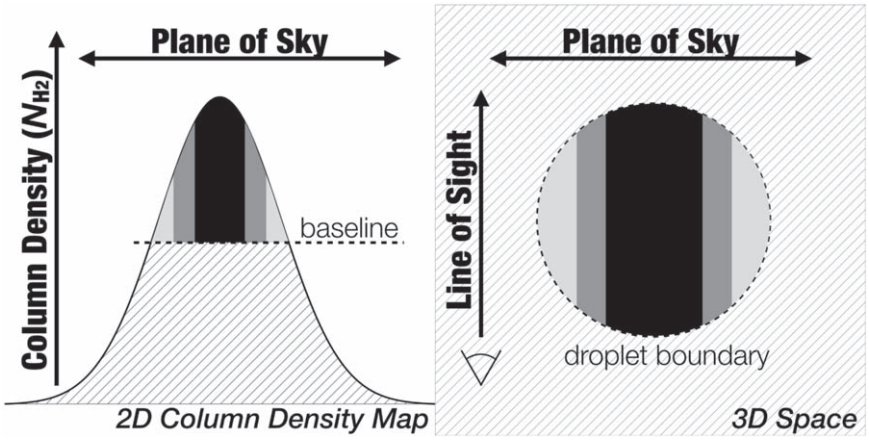

Figure 29. This cartoon shows the mass (integrated column density) on a column density distribution derived from a 2D column density map (left; with the vertical axis corresponding to the column density) and the corresponding volumes in the *3D space* (right; with the line of sight along the vertical axis), if a single baseline removal is applied. The solid shaded area (in black/dark gray/gray) corresponds to the mass (integrated column density) estimated from the 2D column density map (left) and the material occupying the corresponding volume in the 3D space (right). Schematically, a single baseline removal corresponds to the "subtraction" of column density below the dashed line in the panel on the left. For a structure with a spherical shape, such subtraction corresponds to the removal of the contribution from material outside the dashed line in the panel on the right. Depending on the algorithm used for the baseline removal, the "subtraction" might not exactly correspond to the removal of a flat-top function as shown in this cartoon. The cartoon is used only to demonstrate how a single baseline removal does not fit the purpose of simultaneously estimating the masses within different layers at different radial distances.

Appendix F
Uncertainty in Mass Due to the Potential Bias in SED Fitting of *Herschel* Observations

Here, we examine the uncertainty in the potentially biased SED fitting of the *Herschel* observations. As presented above, we use the column density map obtained via SED fitting of *Herschel* observations to estimate the mass of the droplets (Section 2.2). Using the *Herschel* column density to estimate the mass and the fits to the NH_3 line profiles to estimate the velocity dispersion allows mutually independent measurements of the mass–size and the mass–line width relations (Figure 9). However, it is a known issue that SED fitting of emissions in *Herschel* bands might be biased, especially toward cold and dense regions (Shetty et al. 2009a, 2009b; Kelly et al. 2012). In the cold and dense regions, there can be a certain degree of redundancy between a high dust temperature and a high column density. As a result, the SED fitting can overestimate the dust temperature and underestimate the column density, which would result in underestimated masses for the droplets in this case.

Consistently with what Friesen et al. (2017) pointed out, Figure 30(a) shows that the dust temperature, $T_{\rm dust}$, is systematically 2–3 K higher than the kinetic temperature of the dense gas traced by NH_3 emission, $T_{\rm kin}$. Figure 30(a) also shows that, for pixels within the boundaries of the droplets, the difference between $T_{\rm dust}$ and $T_{\rm kin}$ could be even larger, up to 6 K. Figure 30(b) further shows that, for pixels within the boundaries of the droplets, not only is the difference between $T_{\rm dust}$ and $T_{\rm kin}$ larger than the median value of the entire cloud, the pixel-by-pixel NH_3 abundance obtained by dividing the $N_{\rm NH_3}$ (from fitting the NH_3 hyperfine line profiles; see Friesen et al. (2017)) by $N_{\rm H_2}$ (from SED fitting of *Herschel* observations) is higher than the cloud median. The distribution is consistent with overestimated temperature and underestimated column density in the SED fitting of *Herschel* observations.

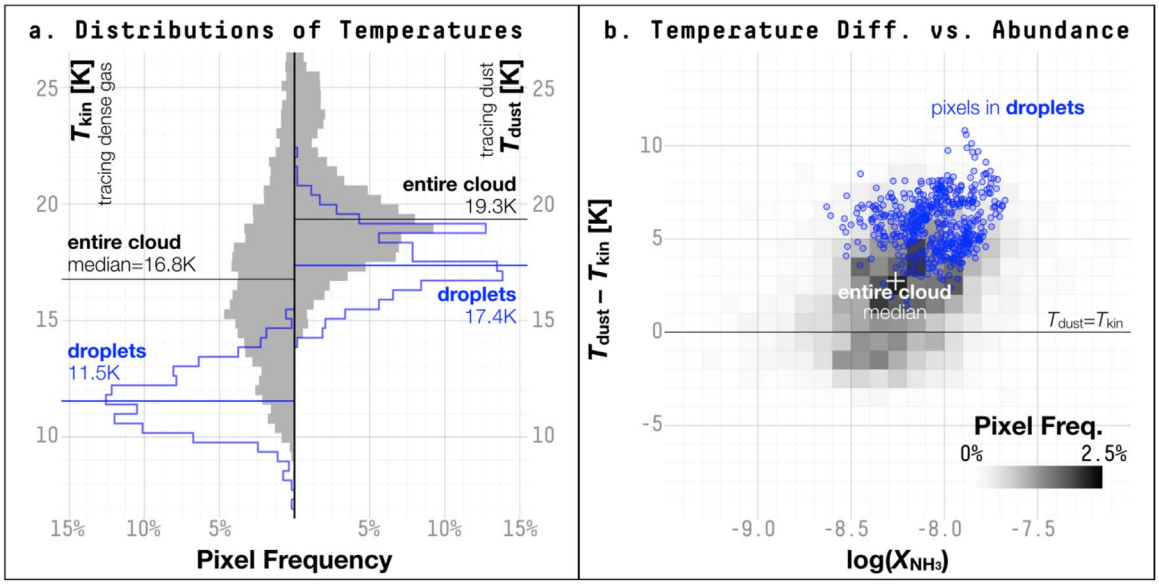

Figure 30. Comparison between properties based on fitting NH_3 hyperfine line profiles and those from the SED fitting of the *Herschel* observations, using the L1688 region as an example. (a) Pixel-by-pixel distributions of temperatures measured from fitting the NH_3 hyperfine line profiles (kinetic temperature, T_{kin}; shown to the left) and from SED fitting of *Herschel* observations (the dust temperature, T_{dust}; shown to the right). Only pixels with significant detection of NH_3 (1, 1) emission are included in this plot (i.e., the total number of pixels included on the left half of the plot is the same as that on the right). The distributions are normalized by the total number of pixels in each group (the cloud or the droplets), so the height of each bin in the histograms corresponds to the frequency of a certain range of values occurring in each group (shown along the horizontal axis as a percentage). The gray histograms show the distributions of all the pixels outside the boundaries of the droplets, and the blue histograms show the distributions of all the pixels inside the droplet boundaries. The median of each distribution is shown as a horizontal line. (b) Two-dimensional histogram showing the distribution of the difference between the dust temperature and the kinetic temperature (T_{dust}–T_{kin}), as a function of the NH_3 abundance ($X_{NH_3} = N_{NH_3}/N_{H_2}$, where N_{H_2} is derived from the SED fitting of the *Herschel* observations). The 2D histogram in each panel shows the distribution of pixels with significant detection of NH_3 (1, 1) emission in the entire map, with the pixel frequency defined as the percentage of pixels on the map falling in each 2D bin in the 2D histogram. The blue dots show the distribution of individual pixels within the droplet boundaries. The horizontal line shows where $T_{dust} = T_{kin}$, and the white cross marks the median values of the abundance and the difference in temperature of the entire cloud.

In this section, we try to estimate the effects of underestimated column density in the SED fitting of *Herschel* observations. In particular, we examine the effects of the underestimated column density on the virial analysis presented in Section 3.3. We compare N_{H_2}, obtained via the SED fitting of *Herschel* observations, to N_{NH_3}, obtained via fitting the NH_3 hyperfine line profiles (for details, see Friesen et al. (2017)). Unfortunately, for the model used in the NH_3 hyperfine line fitting, we need detections of emission from both the NH_3 (1, 1) and (2, 2) lines to determine the population ratios between the two states, in order to estimate N_{NH_3} and T_{kin}. While all pixels within the droplets are detected in NH_3 (1, 1) emission, not all pixels within the droplets are detected in NH_3 (2, 2) emission, so we can only obtain estimates of N_{NH_3} in the densest regions within the droplets. Thus, estimating the mass solely from N_{NH_3} is difficult, especially given that we expect the column density to decrease toward the outer edge of a droplet.

Thus, in order to assess the potential bias in the column density obtained via SED fitting of *Herschel* observations, we used the pixels within the droplet boundaries where we have measurements of both N_{NH_3} and N_{H_2} (i.e., the pixels where we have significant detection of NH_3 (2, 2) emission). We compare the abundance of the droplets (obtained by dividing N_{NH_3} by N_{H_2}) to the median value of the cloud and assume that the difference in abundance between the droplet values and the cloud median is fully due to the underestimated N_{H_2} in the droplets. Assuming the underlying, "real" NH_3 abundance, $X_{real} \equiv N_{NH_3,droplet}/N_{H_2,real}$, is equal to the median NH_3 abundance of the cloud, $X_{cloud} = N_{NH_3,cloud}/N_{H_2,cloud}$, we calculate a correction factor, ϵ:

$$\epsilon = \frac{N_{H_2,real}}{N_{H_2,droplet}} = \frac{N_{NH_3,droplet}}{N_{H_2,droplet}} \frac{N_{H_2,cloud}}{N_{NH_3,cloud}} = \frac{X_{droplet}}{X_{cloud}}, \quad (10)$$

where $N_{H_2,real}$ is the underlying, "real" column density, and $N_{H_2,droplet}$ is the column density measured from the SED fitting for pixels within the droplet boundaries. We can then estimate the "real" mass using this correction factor:

$$M_{real} = \epsilon M_{droplet}, \quad (11)$$

where M_{real} is the underlying, "real" mass, and $M_{droplet}$ is the measured mass of the droplet (from *Herschel* column density; Section 2.2).

After applying the correction factor to the mass, Ω_G and Ω_K in the virial analysis (Section 3.3) are changed by ratios $\propto \epsilon^2$ and $\propto \epsilon$, respectively. The left-hand panels of Figure 31 show the change as arrows, on top of the original mass–size relation (Figure 9(a)) and the original comparisons between various terms in the virial analysis presented in Section 3.3 (see Figures 10 and 11). The right-hand panels of Figure 31 show the resulting plots after applying the correction. Figure 31(a-2) shows that the mass–size relation after the correction is very slightly less steep, and closer to what is found for cloud-scale structures $M \propto R^2$. Figure 31(b-2) shows that, after the

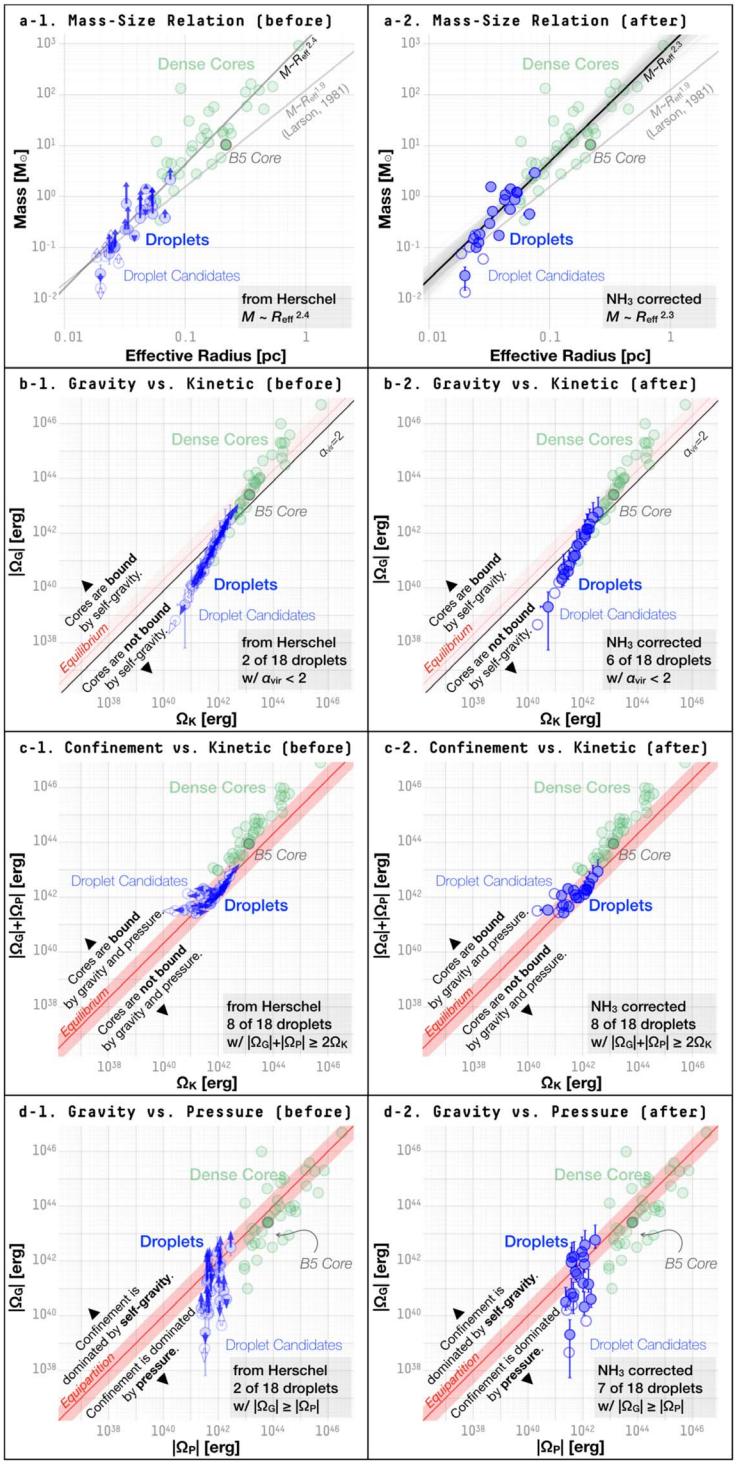

Figure 31. The left four plots show the change in the physical properties corresponding to the correction using N_{NH_3} from the fits to the NH_3 hyperfine line profiles, plotted on top of the original scatter plots. The right four plots show the data points after applying the correction, along the same axes. (a-1) The mass–size distribution of the original data points before the correction, as shown in Figure 9(a), with the change in mass due to the correction shown as arrows. (a-2) The mass–size distribution after applying the correction, plotted along the same axes and with the same data points for dense cores (not affected by the correction). (b-1) The gravitational potential energy plotted against the internal kinetic energy, as shown in Figure 10(a). The changes in both quantities are plotted as arrows. (b-2) The gravitational potential energy plotted against the internal kinetic energy, after applying the correction, plotted along the same axes and with the same data points for dense cores (not affected by the correction). (c-1) The sum of the gravitational potential energy and the energy due to the pressure exerted on the cores by the thermal and nonthermal motions of the ambient gas, plotted against the internal kinetic energy, as shown in Figure 11(a). The changes due to the correction in both quantities are plotted as arrows. (c-2) The sum of gravitational potential energy and the ambient pressure energy term, plotted against the internal kinetic energy, after applying the correction, plotted along the same axes and with the data points for dense cores (not affected by the correction). (d-1) The gravitational potential energy, plotted against the energy due to the pressure exerted on the core surfaces by the thermal and nonthermal motions of the ambient gas, as shown in Figure 11. The changes in the gravitational potential energy due to the correction are plotted as arrows. (d-2) The gravitational potential energy, plotted against the ambient pressure energy, after applying the correction, plotted along the same axes and with the data points for the dense cores (not affected by the correction).

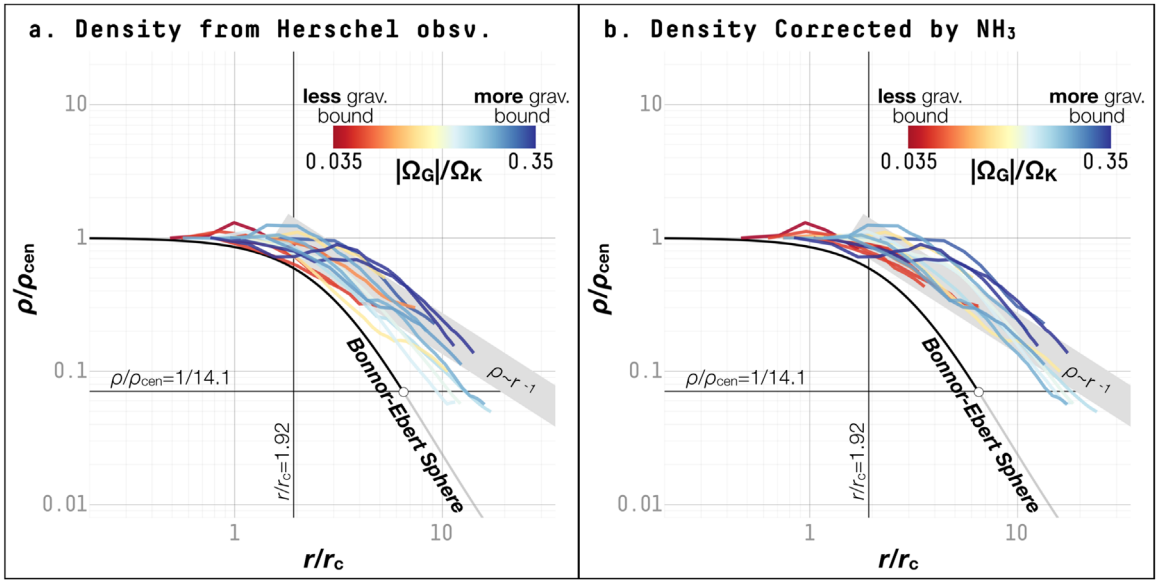

Figure 32. Radial density profiles of the droplets before and after applying the correction using Equation (11). (a-1) The original radial density profiles in dimensionless units (same as Figure 12(a)). (a-2) The radial density profiles in dimensionless units, after applying the correction on the characteristic size scale, r_c, which is dependent on ρ_{cen}. No correction is applied on $y \equiv \rho/\rho_{cen}$, assuming that the same correction factor is applicable on the volume density measured at different distances from the centroid position of a droplet.

correction, a total of six droplets (out of 18 identified in Section 3.1) are now gravitationally "bound" based on the conventional criterion of $\alpha_{vir} = 2$, as opposed to only two droplets that were bound before applying the correction. The correction on the gravitational potential energy also makes the gravitational term, Ω_G, in the virial analysis appear more comparable to the ambient pressure term, Ω_P (Figure 31(d-2)).

The correction also affects the normalized radial profiles of density. The characteristic radius, r_c, which is used to normalize the radial distance from the center, is dependent on the density measured at the center of a droplet and is changed by a ratio of $\propto 1/\sqrt{\epsilon}$, making r_c smaller and consequently x larger. On the other hand, $y \equiv \rho/\rho_{cen}$ is dimensionless and is thus not affected by the correction on the mass (or equivalently, on the density). The resulting change makes the normalized density profiles look even shallower and closer to $\rho \propto r^{-1}$ at larger distances (Figure 32).

Overall, the correction does not qualitatively alter the results of the analyses presented in Sections 3.2 and 3.3. With the corrected mass, the droplets still appear to follow the same power-law mass–size relation found for dense cores (Figure 31(a-2)). Most of the droplets are still gravitationally unbound (Figure 31(b-2)), and the ambient pressure remains important in confining the droplets (Figure 31(c-2)). The density profiles of the droplets appear even shallower and seem to remain continuous from the typical density profile found for cloud-scale structures (Figure 32(a-2)).

Again, because we did not detect NH_3 (2, 2) emission everywhere within the droplet boundaries with the GAS observations, and because we hope to examine the mass–size relation with each term independently measured, we base the analyses presented in this paper on the mass estimated from the *Herschel* column density. The column density obtained from the SED fitting of *Herschel* observations also gives better estimates of the radial density profiles outside regions where we find the dense gas (as traced by NH_3 emission). The "correction" examined in this section serves only as an estimate of the uncertainty in the SED fitting of *Herschel* observations, and we emphasize that a more sophisticated approach is needed to further determine the effects of varying NH_3 abundances due to changes in the astrochemical environments.

Appendix G
Radial Profiles in Physical Units

In Section 4.1.1, we examine the radial profiles and compare them to the Bonnor–Ebert sphere (Ebert 1955; Bonnor 1956; Spitzer 1968). Following the dimensionless analysis in Spitzer (1968), we show that the radial density profiles of the droplets are generally shallower than the Bonnor–Ebert sphere (Figure 12). The analysis in dimensionless units allows comparisons between droplets of different sizes (Section 4.1.1).

Figure 33 shows the radial profiles of the volume density and the pressure in physical units. Again, it demonstrates that drawing comparisons between droplets of different sizes is difficult in physical units. See also Figure 8 for the radial profile of line widths in physical units.

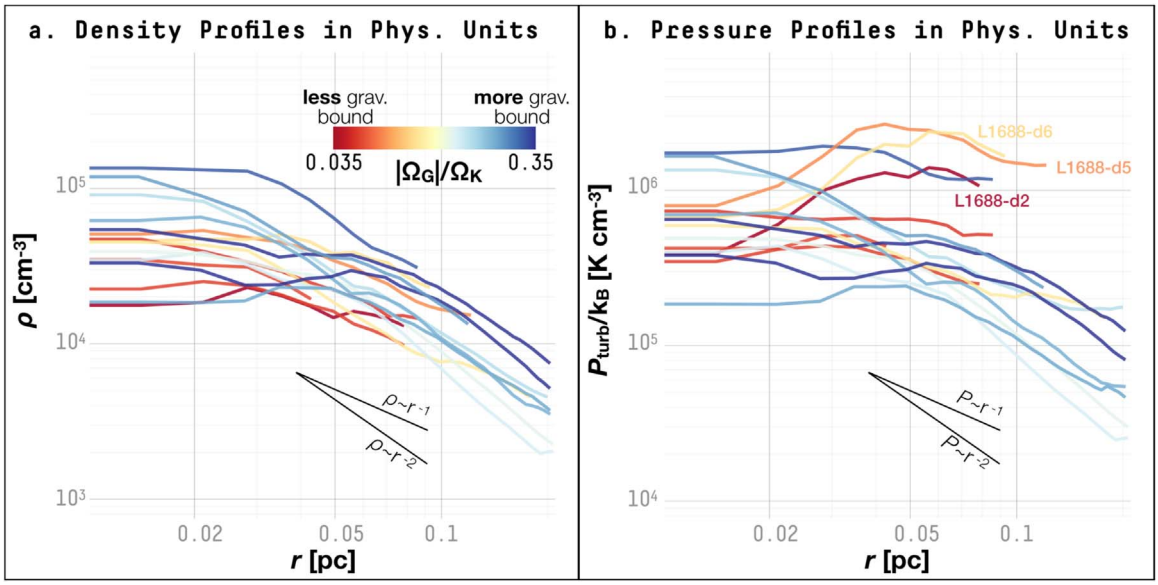

Figure 33. Radial profiles in physical units. (a) The radial density profiles of the droplets, color coded according to the ratio between the gravitational potential energy, Ω_G, and the internal kinetic energy, Ω_K, similar to Figures 12 and 13. The unit of the volume density is the number of molecules per cubic centimeter. (b) The radial pressure profiles of the droplets, similarly color coded by the ratio between the gravitational potential energy, Ω_G, and the internal kinetic energy, Ω_K. Here, the pressure measurement is expressed in the unit of K cm^{-3}, as a ratio between the measured pressure and the Boltzmann constant. L1688-d2, L1688-d5, and L1688-d6 are specifically marked, either because the droplets are elongated or because they sit near the edge of the regions where NH_3 (1, 1) is detected, both of which render the profiles potentially biased. Because the dumbbell shape of L1688-d1 affects this analysis (which assumes spherical geometry), L1688-d1 is not included in this plot.

ORCID iDs

Hope How-Huan Chen https://orcid.org/0000-0001-6222-1712
Jaime E. Pineda https://orcid.org/0000-0002-3972-1978
Alyssa A. Goodman https://orcid.org/0000-0003-1312-0477
Andreas Burkert https://orcid.org/0000-0001-6879-9822
Stella S. R. Offner https://orcid.org/0000-0003-1252-9916
Rachel K. Friesen https://orcid.org/0000-0001-7594-8128
Philip C. Myers https://orcid.org/0000-0002-2885-1806
Felipe Alves https://orcid.org/0000-0002-7945-064X
Héctor G. Arce https://orcid.org/0000-0001-5653-7817
Paola Caselli https://orcid.org/0000-0003-1481-7911
Michael Chun-Yuan Chen https://orcid.org/0000-0003-4242-973X
James Di Francesco https://orcid.org/0000-0002-9289-2450
Adam Ginsburg https://orcid.org/0000-0001-6431-9633
Jared Keown https://orcid.org/0000-0003-2628-0250
Helen Kirk https://orcid.org/0000-0002-5779-8549
Peter G. Martin https://orcid.org/0000-0002-5236-3896
Christopher Matzner https://orcid.org/0000-0001-9732-2281
Anna Punanova https://orcid.org/0000-0001-6004-875X
Elena Redaelli https://orcid.org/0000-0002-0528-8125
Erik Rosolowsky https://orcid.org/0000-0002-5204-2259
Samantha Scibelli https://orcid.org/0000-0002-9485-4394
Ayushi Singh https://orcid.org/0000-0001-6022-3618

References

André, P., Di Francesco, J., Ward-Thompson, D., et al. 2014, in Protostars and Planets VI, ed. H. Beuther et al. (Tucson, AZ: Univ. Arizona Press), 27
André, P., Men'shchikov, A., Bontemps, S., et al. 2010, A&A, 518, L102
Ballesteros-Paredes, J., Vázquez-Semadeni, E., & Scalo, J. 1999, ApJ, 515, 286
Barranco, J. A., & Goodman, A. A. 1998, ApJ, 504, 207
Beaumont, C., Goodman, A., & Greenfield, P. 2015, in ASP Conf. Ser. 495, Astronomical Data Analysis Software an Systems XXIV (ADASS XXIV), ed. A. R. Taylor & E. Rosolowsky (San Francisco, CA: ASP), 101
Beaumont, C. N., Offner, S. S. R., Shetty, R., Glover, S. C. O., & Goodman, A. A. 2013, ApJ, 777, 173
Benson, P. J., Caselli, P., & Myers, P. C. 1998, ApJ, 506, 743
Benson, P. J., & Myers, P. C. 1983, ApJ, 270, 589
Benson, P. J., & Myers, P. C. 1989, ApJS, 71, 89
Bertoldi, F., & McKee, C. F. 1992, ApJ, 395, 140
Bonnor, W. B. 1956, MNRAS, 116, 351
Bourke, T. L., Hyland, A. R., & Robinson, G. 1995, MNRAS, 276, 1052
Caselli, P., Benson, P. J., Myers, P. C., & Tafalla, M. 2002, ApJ, 572, 238
Cox, A. N., & Pilachowski, C. A. 2000, PhT, 53, 77
Crapsi, A., Caselli, P., Walmsley, M. C., & Tafalla, M. 2007, A&A, 470, 221
Dame, T. M., & Thaddeus, P. 1985, ApJ, 297, 751
de Geus, E. J., de Zeeuw, P. T., & Lub, J. 1989, A&A, 216, 44
Dullemond, C. P., Juhasz, A., Pohl, A., et al. 2012, RADMC-3D: A multi-purpose radiative transfer tool, Astrophysics Source Code Library, ascl:1202.015
Dunham, M. M., Allen, L. E., Evans, N. J., II, et al. 2015, ApJS, 220, 11
Ebert, R. 1955, ZA, 37, 217
Elmegreen, B. G. 2000, ApJ, 530, 277
Enoch, M. L., Evans, N. J., II, Sargent, A. I., et al. 2008, ApJ, 684, 1240
Evans, N. J., II 1999, ARA&A, 37, 311
Federrath, C. 2013, MNRAS, 436, 1245
Fischera, J., & Martin, P. G. 2012, A&A, 547, A86
Friesen, R. K., Di Francesco, J., Shimajiri, Y., & Takakuwa, S. 2010, ApJ, 708, 1002
Friesen, R. K., Di Francesco, J., Shirley, Y. L., & Myers, P. C. 2009, ApJ, 697, 1457
Friesen, R. K., Pineda, J. E., co-PIs, et al. 2017, ApJ, 843, 63
Fuller, G. A., & Myers, P. C. 1992, ApJ, 384, 523
Galli, P. A. B., Loinard, L., Ortiz-Léon, G. N., et al. 2018, ApJ, 859, 33
Garay, G., & Lizano, S. 1999, PASP, 111, 1049
Ginsburg, A., & Mirocha, J. 2011, PySpecKit: Python Spectroscopic Toolkit, Astrophysics Source Code Library, ascl:1109.001
Goodman, A. A., Barranco, J. A., Wilner, D. J., & Heyer, M. H. 1998, ApJ, 504, 223
Goodman, A. A., Benson, P. J., Fuller, G. A., & Myers, P. C. 1993, ApJ, 406, 528
Gurney, M., Plume, R., & Johnstone, D. 2008, PASP, 120, 1193
Hacar, A., Tafalla, M., Kauffmann, J., & Kovács, A. 2013, A&A, 554, A55
Hildebrand, R. H. 1983, QJRAS, 24, 267
Hilton, J., & Lahulla, J. F. 1995, A&AS, 113, 325

Jeans, J. H. 1902, RSPTA, 199, 1
Jijina, J., Myers, P. C., & Adams, F. C. 1999, ApJS, 125, 161
Johnstone, D., Fich, M., Mitchell, G. F., & Moriarty-Schieven, G. 2001, ApJ, 559, 307
Johnstone, D., Wilson, C. D., Moriarty-Schieven, G., et al. 2000, ApJ, 545, 327
Jørgensen, J. K., Johnstone, D., Kirk, H., et al. 2008, ApJ, 683, 822
Kauffmann, J., Bertoldi, F., Bourke, T. L., Evans, N. J., II, & Lee, C. W. 2008, A&A, 487, 993
Kauffmann, J., Pillai, T., Shetty, R., Myers, P. C., & Goodman, A. A. 2010a, ApJ, 712, 1137
Kauffmann, J., Pillai, T., Shetty, R., Myers, P. C., & Goodman, A. A. 2010b, ApJ, 716, 433
Kelly, B. C., Shetty, R., Stutz, A. M., et al. 2012, ApJ, 752, 55
Keto, E. R., & Myers, P. C. 1986, ApJ, 304, 466
Kirk, H., Dunham, M. M., Di Francesco, J., et al. 2017a, ApJ, 838, 114
Kirk, H., Friesen, R. K., Pineda, J. E., et al. 2017b, ApJ, 846, 144
Kirk, H., Pineda, J. E., Johnstone, D., & Goodman, A. 2010, ApJ, 723, 457
Kun, M. 1998, ApJS, 115, 59
Lada, C. J., Muench, A. A., Rathborne, J., Alves, J. F., & Lombardi, M. 2008, ApJ, 672, 410
Ladd, E. F., Myers, P. C., & Goodman, A. A. 1994, ApJ, 433, 117
Larson, R. B. 1981, MNRAS, 194, 809
Lee, C. W., Myers, P. C., & Tafalla, M. 1999, ApJ, 526, 788
Li, H.-B., Yuen, K. H., Otto, F., et al. 2015, Natur, 520, 518
Li, P. S., Martin, D. F., Klein, R. I., & McKee, C. F. 2012, ApJ, 745, 139
Loren, R. B. 1989, ApJ, 338, 902
Mangum, J. G., & Shirley, Y. L. 2015, PASP, 127, 266
Maruta, H., Nakamura, F., Nishi, R., Ikeda, N., & Kitamura, Y. 2010, ApJ, 714, 680
McKee, C. F., & Ostriker, E. C. 2007, ARA&A, 45, 565
McLaughlin, D. E., & Pudritz, R. E. 1996, ApJ, 469, 194
McLaughlin, D. E., & Pudritz, R. E. 1997, ApJ, 476, 750
Montillaud, J., Juvela, M., Rivera-Ingraham, A., et al. 2015, A&A, 584, A92
Motte, F., Andre, P., & Neri, R. 1998, A&A, 336, 150
Myers, P. C. 1983, ApJ, 270, 105
Myers, P. C. 1998, ApJL, 496, L109
Myers, P. C., & Benson, P. J. 1983, ApJ, 266, 309
Myers, P. C., Fuller, G. A., Goodman, A. A., & Benson, P. J. 1991, ApJ, 376, 561
Myers, P. C., Linke, R. A., & Benson, P. J. 1983, ApJ, 264, 517
Offner, S. S. R., & Arce, H. G. 2015, ApJ, 811, 146
Onishi, T., Mizuno, A., Kawamura, A., Tachihara, K., & Fukui, Y. 2002, ApJ, 575, 950
Ortiz-León, G. N., Loinard, L., Kounkel, M. A., et al. 2017, ApJ, 834, 141
Padoan, P., Federrath, C., Chabrier, G., et al. 2014, in Protostars and Planets VI, ed. H. Beuther et al. (Tucson, AZ: Univ. Arizona Press), 77
Pattle, K., Ward-Thompson, D., Kirk, J. M., et al. 2015, MNRAS, 450, 1094
Pineda, J. E., Goodman, A. A., Arce, H. G., et al. 2010, ApJL, 712, L116
Pineda, J. E., Goodman, A. A., Arce, H. G., et al. 2011, ApJL, 739, L2
Pineda, J. E., Offner, S. S. R., Parker, R. J., et al. 2015, Natur, 518, 213
Planck Collaboration, Abergel, A., Ade, P. A. R., et al. 2014, A&A, 571, A11
Rebull, L. M., Padgett, D. L., McCabe, C.-E., et al. 2010, ApJS, 186, 259
Ridge, N. A., Di Francesco, J., Kirk, H., et al. 2006, AJ, 131, 2921
Robitaille, T., Beaumont, C., Qian, P., Borkin, M., & Goodman, A. 2017, Glueviz: Multidimensional Data Exploration Glueviz: Multidimensional Data Exploration, v0.13.1, Zenodo, doi:10.5281/zenodo.1237692
Rosolowsky, E., & Leroy, A. 2006, PASP, 118, 590
Rosolowsky, E. W., Pineda, J. E., Foster, J. B., et al. 2008a, ApJS, 175, 509
Rosolowsky, E. W., Pineda, J. E., Kauffmann, J., & Goodman, A. A. 2008b, ApJ, 679, 1338
Schlafly, E. F., Green, G., Finkbeiner, D. P., et al. 2014, ApJ, 786, 29
Schmidt, E. G. 1975, MNRAS, 172, 401
Schneider, S., & Elmegreen, B. G. 1979, ApJS, 41, 87
Schöier, F. L., van der Tak, F. F. S., van Dishoeck, E. F., & Black, J. H. 2005, A&A, 432, 369
Seo, Y. M., Shirley, Y. L., Goldsmith, P., et al. 2015, ApJ, 805, 185
Shetty, R., Glover, S. C., Dullemond, C. P., & Klessen, R. S. 2011, MNRAS, 412, 1686
Shetty, R., Kauffmann, J., Schnee, S., & Goodman, A. A. 2009a, ApJ, 696, 676
Shetty, R., Kauffmann, J., Schnee, S., Goodman, A. A., & Ercolano, B. 2009b, ApJ, 696, 2234
Shu, F. H. 1977, ApJ, 214, 488
Spitzer, L., Jr. 1968, in Dynamics of Interstellar Matter and the Formation of Stars, ed. B. M. Middlehurst & L. H. Aller (Chicage, IL: Univ. Chicago Press), 1
Stanke, T., Smith, M. D., Gredel, R., & Khanzadyan, T. 2006, A&A, 447, 609
Straizys, V., Cernis, K., Kazlauskas, A., & Meistas, E. 1992, BaltA, 1, 149
Tafalla, M., & Hacar, A. 2015, A&A, 574, A104
Tafalla, M., Myers, P. C., Caselli, P., & Walmsley, C. M. 2004, A&A, 416, 191
Tan, J. C., Krumholz, M. R., & McKee, C. F. 2006, ApJL, 641, L121
The Astropy Collaboration, Price-Whelan, A. M., Sipőcz, B. M., et al. 2018, AJ, 156, 123
Ward-Thompson, D., Di Francesco, J., Hatchell, J., et al. 2007, PASP, 119, 855
Ward-Thompson, D., Nutter, D., Bontemps, S., Whitworth, A., & Attwood, R. 2006, MNRAS, 369, 1201
Wood, D. O. S., Myers, P. C., & Daugherty, D. A. 1994, ApJS, 95, 457
Young, K. E., Enoch, M. L., Evans, N. J., I, et al. 2006, ApJ, 644, 326
Zdanavičius, K., Maskoliūnas, M., Zdanavičius, J., Straižys, V., & Kazlauskas, A. 2011, BaltA, 20, 317